

USING THERMOCHRONOLOGY TO TEST THE VALIDITY OF TWO BALANCED
CROSS SECTIONS, KARNALI RIVER, FAR-WESTERN NEPAL

by

CLAIRE ELIZABETH BATTISTELLA

DELORES ROBINSON, COMMITTEE CHAIR
NADINE MCQUARRIE
HAROLD STOWELL
MATTHEW WIELICKI

A THESIS

Submitted in partial fulfillment of the requirements
for the degree of Master of Science
in the Department of Geological Sciences
in the Graduate School of
The University of Alabama

TUSCALOOSA, ALABAMA

2019

Copyright Claire Elizabeth Battistella 2019
ALL RIGHTS RESERVED

ABSTRACT

A balanced cross section provides a viable subsurface geometry; however, multiple subsurface cross section geometries may be possible to match the observed surface geology. Low-temperature thermochronologic data and thermokinematic models can be used to test these multiple subsurface geometries. In this study, I use muscovite $^{40}\text{Ar}/^{39}\text{Ar}$, apatite and zircon fission track, and zircon (U-Th)/He ages in conjunction with two balanced cross sections along the Karnali River in far western Nepal to determine if the cross sections are viable. The balanced cross sections are reconstructed to determine the kinematic sequence and then sequentially deformed in ~10 km increments with flexural loading and erosional isostatic unloading applied to each step. Ages are assigned to each 10 km increment of displacement and then used to create a 2-D thermokinematic model, which predicts the cooling ages along the section. By varying the location of the décollement ramp, shortening rates, and radiogenic heat production, the model is modified to better match the existing observed age data. Comparison of the modeled cooling ages to the thermochronologic data indicates that although the cross sections are valid and balanced, the subsurface fault geometry does not reproduce the existing observed cooling ages over the young uplift imparted by the active ramp in the décollement below the Lesser Himalayan duplex. Thus, a new balanced cross section is needed with a different location and geometry of the ramp to produce the existing cooling ages.

DEDICATION

To my friends and family, for their love and support.

LIST OF ABBREVIATIONS AND SYMBOLS

°C Temperature in degrees Celsius

$\mu\text{W m}^{-3}$ Microwatt per meter cubed

A₀ Radiogenic heat production

AFT Apatite fission track

AHe Apatite (U-Th)/He

DK Dadeldhura klippe

EET Effective elastic thickness

ϵ Epsilon

GH Greater Himalaya

GPa Gigapascal

km Kilometer(s)

LH Lesser Himalaya

LHD Lesser Himalayan duplex

LHZ Lesser Himalayan imbricate zone

m Meter(s)

Ma Million years

Mar $^{40}\text{Ar}/^{39}\text{Ar}$ of muscovite

MBT	Main Boundary thrust
MCT	Main Central thrust
MFT	Main Frontal thrust
MHT	Main Himalayan thrust
Nd	Neodymium
RMT	Ramgarh-Munsiari thrust
SH	Subhimalayan
SHTS	Subhimalayan thrust system
STDS	Southern Tibetan Detachment system
TH	Tibetan Himalaya
yr	Year
ZHe	Zircon (U-Th)/He

ACKNOWLEDGMENTS

I am very grateful to the many people that have helped and supported me in completing this research. I thank Dr. Delores Robinson for her support, guidance, and insights throughout all stages of this research. I am grateful to Dr. Nadine McQuarrie, Dr. Harold Stowell, and Dr. Matthew Wielicki for serving on my thesis committee and providing helpful feedback.

I am grateful for the University of Alabama Graduate School and the Department of Geological Sciences. I thank the Graduate School for providing the Graduate Council Fellowship, the Department of Geological Sciences for providing the Hooks Fund and Johnson Student Travel Fund, and Dr. Robinson for providing funding for fieldwork in Nepal and a research assistantship from her NSF grant. The National Science Foundation provided funding for this research (NSF EAR Tectonics 1524320).

I thank my friends Suryodoy Ghoshal, Joshua Olsen, and Victoria Buford (University of Pittsburgh) for their assistance with 2D Move and Pecube. Thank you to my lab mates Gourab Bhattacharya and Elizabeth Olree for their support and encouragement. Special thanks to my friends Sarah Beth Carson and Travis Sizemore for their love and support throughout this research.

CONTENTS

ABSTRACT	ii
DEDICATION	iii
LIST OF ABBREVIATIONS AND SYMBOLS	iv
ACKNOWLEDGMENTS	vi
LIST OF FIGURES	ix
LIST OF TABLES	xi
1. INTRODUCTION	1
2. GEOLOGIC SETTING	4
2.1 Structural and Other Published Data.....	12
2.2 Balanced Cross Sections	17
2.3 Thermochronologic Data	17
3. METHODS	22
3.1 Sample Collection.....	22
3.2 Flexural and Kinematic Model	23
3.2.1 Kinematic Analysis	23
3.2.2 Initial Model Configuration	23
3.2.3 Flexural Isostasy Model	25
3.2.4 Model Parameters	28
3.3 Thermokinematic Modeling.....	29
4. RESULTS	33

4.1 Robinson et al. (2006) Simikot cross section.....	33
4.1.1 Flexural-kinematic model	33
4.1.2 Thermokinematic model	44
4.1.2.1 Effect of variable radiogenic heat production on predicted cooling ages.....	44
4.1.2.2 Effect of variable shortening rates on predicted cooling ages	45
4.2 Modified version of Simikot cross section from Olsen et al. (2018).....	53
4.2.1 Flexural-kinematic model	53
4.2.2 Thermokinematic model	64
4.2.2.1 Effect of variable radiogenic heat production on predicted cooling ages.....	64
4.2.2.2 Effect of variable shortening rates on predicted cooling ages	65
5. INTERPERTATIONS AND DISCUSSION	72
5.1 Evaluating the sensitivity of predicted cooling ages.....	72
5.2 Evaluating cross section geometry.....	74
5.3 Proposed New Cross Section	76
6. CONCLUSIONS.....	79
REFERENCES	80
APPENDIX A: NEW MAPPING OF FAR-WESTERN NEPAL.....	90
APPENDIX B: NEW THERMOCHRONOLOGY SAMPLES COLLECTED ALONG SIMIKOT CROSS SECTION	91
APPENDIX C: VELOCITY MODELS WITH TIMING OF MOVEMNT ON INDIVIDUAL FAULTS	92

LIST OF FIGURES

1. (A) Shaded relief map of the Himalayan-Tibetan orogen, with the Indus suture zone highlighted and Nepal outlined in white. (B) Generalized geologic map of the Nepal Himalaya, modified from Robinson and Martin (2014). Box indicates extent of far-western Nepal mapped by Robinson et al. (2006). (C) Simplified geologic map of far-western Nepal adapted from Robinson (2008). Simikot cross section trace from A to A' 5
2. Geologic map of far-western Nepal, modified from Robinson et al. (2006). Simikot cross section A to A'..... 11
3. Field photos of major structures along the Simikot cross section. (A) View to the south of the MBT and Siwaliks hills in the distance. (B) MCT or DT fault at the base of the southern end of the DK separating LH rocks from the GH DK rocks. (C) Photo looking to the north at a LHD thrust fault separating Kushma Formation from Ranimata Formation. (D) MCT separating GH rock from LH rock..... 12
4. (A) Balanced Simikot cross section from Robinson et al. (2006) with restored section below. (B) Modified version of the Simikot cross section from Olsen et al. (2018) with restored section below. 16
5. Published MAr, ZHe, AFT, and AHe thermochronometer cooling ages with 2σ error along Simikot cross section from Robinson et al. (2006). Data from McCallister et al. (2014), Sakai et al. (2013), van der Beek et al. (2016), and unpublished data from Harvey (2015) and Mercier (2014). 21
6. (A) Initial configuration of the Robinson et al. (2006) model, shown as an example of the initial model configuration of the Move models. (B-G) Simplified illustration of isostatic response to deformation and erosion. (B) Simplified restored cross section with future fault (red dashed line). (C) Motion on fault. (D) Isostatic loading (black arrows) of material moved by fault. (E) Erosion of material above new topography (black dashed line) generated using critical wedge angle. (F) Isostatic unloading (black arrows) from removal of eroded materials mass. (G) Sediment loading from deposition of sediments in the foreland basin. 25
7. (A-S) Sequential flexural kinematic Robinson et al. (2006) cross section reconstructions. (A-C) has a vertical exaggeration of 1.5 and (D-S) has no vertical exaggeration. Active fault is red, dotted black line is the topographic surface, and solid black lines are inactive future fault ramp locations. Details of deformation are discussed in text and listed in Table 6. Individual stratigraphic units are identified by colored lines the line represents the top of unit and white area below line is the rock unit. GH rocks (dark pink), Kushma Formation (light green), Ranimata Formation (dark green), Sangram Formation (light purple), Galyang Formation

(brown), Syangia Formation (light pink), Lakharpatra Group (blue), Bhainskati Formation (dark purple), Dumri Formation (orange), and Siwaliks Group (yellow).....	42
8. Predicted (A) MAr, (B) ZHe, (C) AFT, and (D) AFT cooling age outputs for Robinson et al. (2006) cross section Pecube models with variable radiogenic heat production values and a constant velocity rate. Predicted cooling ages are lines: black for A_0 of $2.0 \mu\text{W m}^{-3}$, red for A_0 of $2.5 \mu\text{W m}^{-3}$, and blue for A_0 of $3.0 \mu\text{W m}^{-3}$. Observed cooling ages are represented with symbols and 2σ error. MAr (red star), ZHe (orange diamond), AFT (blue circle), and AHE (green star).	43
9. Predicted MAr (red line), ZHe (orange line), AFT (blue line), and AFT (green line) cooling age outputs for Robinson et al. (2006) cross section Pecube models with variable velocity models, summarized in Table 5. (A) Velocity A, (B) Velocity B, (C) Velocity C, (D) Velocity D, and (E) Velocity E all with $A_0 = 2.0 \mu\text{W m}^{-3}$	49
10. (A-T) Sequential flexural kinematic Olsen et al. (2018) cross section reconstructions. (A-C) has a vertical exaggeration of 1.5 and (D-T) has no vertical exaggeration. Active fault is red, dotted black line is the topographic surface, and solid black lines are inactive future fault ramp locations. Details of deformation are discussed in text and listed in Table 8. Individual stratigraphic units are identified by colored lines the line represents the top of unit and white area below line is the rock unit. Rock unit colors are the same as in Figure 7.....	62
11. Predicted (A) MAr, (B) ZHe, (C) AFT, and (D) AFT cooling age outputs for Olsen et al. (2018) cross section Pecube models with variable radiogenic heat production values. Symbols same as in Figure 8.	63
12. Predicted MAr (red line), ZHe (orange line), AFT (blue line), and AFT (green line) cooling age outputs for Olsen et al. (2018) cross section Pecube models with variable velocity models, summarized in Table 5. (A) Velocity F, (B) Velocity G, (C) Velocity H, and (D) Velocity I all with $A_0 = 2.0 \mu\text{W m}^{-3}$	68
13. Thermal structure of crust in final step of Robinson et al. (2006) Pecube models for (A) $A_0 = 2.0$ and (B) $A_0 = 3.0 \mu\text{W m}^{-3}$	73

LIST OF TABLES

1.	Stratigraphy of far-western Nepal.....	6
2.	Published MAr, ZHe, AFT, and AHe cooling ages along Simikot cross section.....	19
3.	Flexural-kinematic model parameters tested in 2D-Move.....	28
4.	Pecube thermokinematic properties.....	30
5.	Deformation ages and rates tested for thermokinematic models	32
6.	Simikot cross section Robinson et al. (2006) flexural-kinematic model displacement	33
7.	Observed cooling ages compared to modeled cooling ages for Robinson et al. (2006) Simikot cross section.....	47
8.	Simikot cross section Olsen et al. (2018) flexural-kinematic model displacement.....	54
9.	Observed cooling ages compared to modeled cooling ages for Olsen et al. (2018) Simikot cross section.....	66

1. INTRODUCTION

Balanced cross sections provide viable cross section geometries based on surface geology and geophysical constraints; however, multiple interpretations can be made for subsurface structures and the location and geometry of the décollement resulting in variable shortening estimates. Kinematic reconstructions of balanced cross sections further test the viability of balanced cross sections and the kinematic sequence of faulting and folding (e.g., Robinson, 2008). However, balanced cross sections and their kinematic reconstructions only provide a spatial constraint in fold-thrust belts. To better understand a fold-thrust belt's evolution, models need to incorporate timing of deformation and exhumation.

In fold-thrust belt systems, the upper crust's temperature distribution is constantly evolving from advection due to the lateral and vertical transport of rock packages along faults, erosional exhumation, and sedimentation (Stüwe et al., 1994; Rahn and Grasemann, 1999; Ehlers and Farley, 2003). Low-temperature thermochronometers record the time that the rock passed through a mineral system's closure temperature and thus, yields information about the evolving thermal structure. The cooling ages of low-temperature thermochronometers are controlled by the timing, magnitude, and rate of exhumation in fold-thrust belts (e.g., Shi and Wang, 1987; Ehlers and Farley, 2003; Huerta and Rodgers, 2006; Lock and Willett, 2008; McQuarrie and Ehlers, 2015). The location, magnitude, and rate of exhumation is a function of fault geometry and deformation rates (Lock and Willett, 2008; McQuarrie and Ehlers, 2015; 2017). In fold-thrust belts, the magnitude of uplift is greatest over fault ramps, which produces topographic highs where erosion is concentrated and exhumation rates increase at that location (Whipp et al.,

2007; Lock and Willett, 2008; Robert et al., 2011; Coutand et al., 2014; McQuarrie and Ehlers, 2015, 2017). Thus, fault geometry and kinematics have a significant impact on exhumation and cooling history of fold-thrust belts.

The coupling of balanced cross sections and thermokinematic models can be used to test the validity of a cross section's geometry and kinematic evolution. In this study, I expand upon previous work by making 2-D thermokinematic models from two sequentially forward modeled balanced cross sections in far western Nepal. This approach addresses the non-uniqueness of balanced cross sections by utilizing all available thermochronological and geologic data to generate a thermokinematic model. The methods used were introduced in McQuarrie and Ehlers (2015) and tested in the Bhutan Himalaya.

Far-western Nepal has a duplex with eight imbricate thrust sheets (Robinson et al., 2006). Each thrust sheet has a unique exhumation history and therefore, a potentially, a distinct age for each low-temperature thermochronometer. By comparing the existing thermochronometric ages to the predicted thermochronometric ages from the models, I can determine if the proposed cross section and the fault geometries could have produced the existing ages. This method has applications for testing cross section geometry, testing the influence of fault geometry, timing and tempo on cooling ages, and can be applied to other convergent orogenic systems to better understand the kinematic evolution.

In this study, I evaluate two balanced cross sections along the Karnali River in far-western Nepal, the Simikot balanced cross section from Robinson et al. (2006) and a modified version of the Simikot cross section from Olsen et al. (2018). The flexural-kinematic models evaluate the flexural, erosional, and isostatic response throughout the formation of the Himalayan fold-thrust belt. The thermokinematic models investigate the evolution of the thermal

history and predict cooling ages along the cross section through time. These models test the viability of a cross section's geometry by matching the predicted thermochronologic data to the observed data, if the observed and modeled thermochronologic data do not match, I can determine how to modify the balanced cross section to better match the existing thermochronologic data.

2. GEOLOGIC SETTING

Convergence between the Indian and Eurasian plates over the past 55 Ma has resulted in approximately 2500 km of crustal shortening (Patriat and Achache, 1984; Besse and Courtillot, 1988; Klootwijk et al., 1992). The Himalayan fold-thrust belt accommodates anywhere from one third to one half of that shortening as it migrates southward (Lyon-Caen and Molnar, 1985; Lillie et al., 1987; Srivastava and Mitra, 1994; Bilham et al., 1997; Powers et al., 1998; Larson et al., 1999; Lavé and Avouac, 2000; DeCelles et al., 2002). The kinematic sequence that accommodates this deformation holds the key to understanding the evolution of the Himalayan thrust belt. Far-western Nepal accommodates the greatest magnitude of horizontal shortening across the entire Himalayan arc with estimates up to ~900 km (Robinson et al., 2006).

The Himalayan rocks are divided into tectonostratigraphic groups that are separated by major fault systems (Fig. 1). From north to south the tectonostratigraphic groups and major fault systems include the Tibetan Himalaya (TH) rocks, Southern Tibetan Detachment system (STDS), Greater Himalaya (GH) rocks, Main Central thrust (MCT), Lesser Himalaya (LH) rocks, Ramgarh-Munsiari thrust (RMT), Lesser Himalayan duplex (LHD), Dadeldhura klippe (DK), Lesser Himalayan imbricate zone (LHZ), Main Boundary thrust (MBT), Subhimalayan (SH) rocks, and the Subhimalayan thrust system (SHTS) with the frontal thrust being the Main Frontal thrust (MFT). Each tectonostratigraphic group is then subdivided into formations based on lithology and age. Table 1 contains lithologic descriptions of the stratigraphy (for more information, see DeCelles et al., 2001; Robinson et al., 2006). All thrusts in the Himalayan thrust belt converge at depth into the basal décollement, the Main Himalayan thrust (MHT).

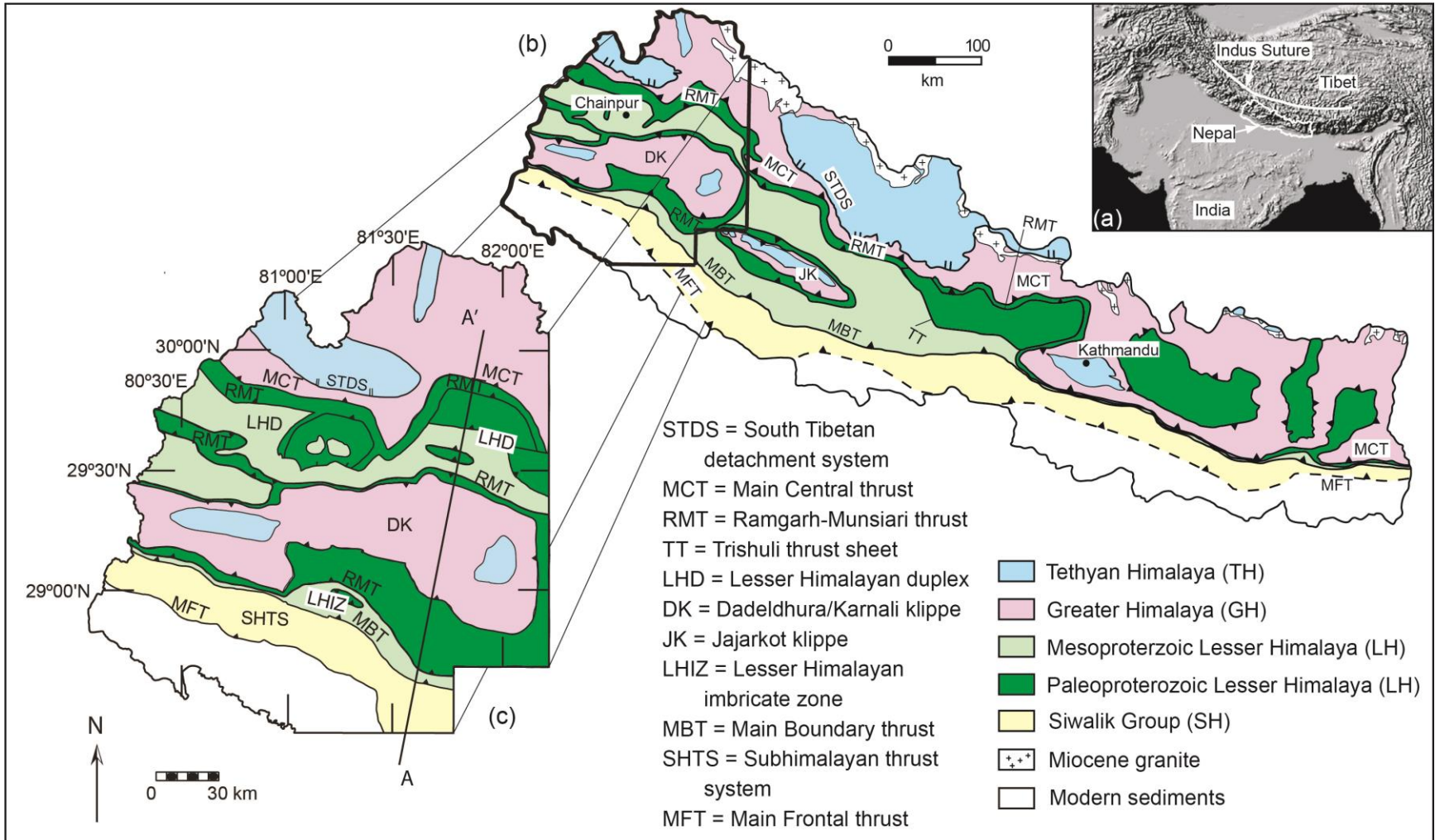


Figure 1: (A) Shaded relief map of the Himalayan-Tibetan orogen, with the Indus suture zone highlighted and Nepal outlined in white. (B) Generalized geological map of the Nepal Himalaya, modified from Robinson and Martin (2014). Box indicates extent of far-western Nepal mapped by Robinson et al. (2006). (C) Simplified geological map of far-western Nepal adapted from Robinson (2008). Simikot cross section trace from A to A'.

Table 1: Stratigraphy of far-western Nepal

Unit Name	Lithological Description	Thickness (m)	Age Constraints (Ma)
<u>Greater Himalaya</u>			
Unit III	Granitic orthogneiss	>2600 ^a	
Unit I	Garnet and kyanite bearing gneiss, migmatite, metaquartzite	6000-15000 ^a	
<u>Lesser Himalaya</u>			
Dumri Fm.	Medium- to fine-grained quartzolithic sandstone, mottled red siltstone	1200 ^a	19.9 to 15.1 ^{bc}
Bhainskati Fm.	Black mudstone, thin beds of dark quartzolithic sandstone	100 ^a	
Gondwanan Unit	Pebbly quartzose conglomerate, sandstone, black shale	300 ^a	
Lakharpatra Group	Blue-grey dolostone and limestone, black slate	3000 ^a	
Syangia Fm.	Pink, green, and white quartzite, green phyllite	500 ^a	
Galyang Fm.	Thinly bedded green, grey, and brown phyllite and black slate	~500-1000 ^a	
Sangram Fm.	White medium-grained orthoquartzite	500 ^a	<1680 ^d
Ranimata Fm.	Green chloritic phyllite, Paleoproterozoic augen orthogneiss	1500-3000 ^a	<1830 ^d
Kushma Fm.	Medium- to coarse-grained white orthoquartzite	800-1500 ^a	1850 ^{de}
<u>Subhimalaya</u>			
upper Siwalik unit	Conglomerate with coarse sandstone ^f	~2000 ^b	>4.6 ^{cef}
middle Siwalik unit	Medium-grained sandstone interbedded with mudstone ^f	~2200 ^b	10.8 to 4.6 ^{cef}
lower Siwalik unit	Fine to medium-grained sandstone interbedded with paleosols ^f	~2000 ^f	16 to 9.7 ^f

^aRobinson et al. (2006); ^bDecelles et al. (2001); ^cOjha et al. (2009); ^dDecelles et al. (2000); ^eQuade et al. (1995);

^fGautam and Fujiwara, (2000).

During Proterozoic time, the Indian passive margin was blanketed with a discontinuous sedimentary package sourced from the Indian craton that compose the LH rocks (Gansser, 1964; Upreti, 1996). Nd isotopic values (e.g., Ahmad et al., 2000; Robinson et al., 2001) and U-Pb detrital zircon ages (e.g., DeCelles et al., 2000) suggest that GH rocks are not derived from the Indian craton and are not Indian cratonic basement. Currently, GH rocks are placed next to LH rocks along the MCT; however, GH rocks were originally formed somewhere north and distal to cratonic India with an age that is bracketed by a maximum depositional age of ~1050 Ma from detrital zircons ages and igneous zircon ages of ~480 Ma (Gehrels et al., 2003; 2006; Martin et al., 2005). From Cambrian to Cretaceous time, the Indian passive margin was once again blanketed by a sedimentary sequence; these units compose the TH rocks that deposited in the Paleotethys Ocean (Brookfield, 1993; Garzanti, 1999; DeCelles et al., 2001) and covered the GH and LH rocks. The combined TH/GH/LH sequences formed the northern extension of the Indian craton known as Greater India (e.g., van Hinsbergen et al., 2011).

Greater India collided with the Eurasian plate along the Indus-Yarlung suture zone between 59-54 Ma (DeCelles et al., 2014; Hu et al., 2016; Najman et al., 2017). The Tethyan thrust belt formed from the initiation of collision as the Indian plate subducted northward under the Eurasian plate (Ratschbacher et al., 1994; Murphy and Yin, 2003; Wang et al., 2011). The Tethyan thrust belt migrated southward burying and metamorphosing GH rocks underneath the thrust belt to peak metamorphic temperatures around 700 °C in far western Nepal (Yakamchuk and Godin, 2012) during Eocene to Oligocene time (Hodges, 2003; Godin et al., 2001; Godin, 2003). TH rocks continued deforming until at least 30 Ma (Ratschbacher et al., 1994; Webb et al., 2011).

Intra-GH thrusts were active from ~28-26 to 17 Ma (Carosi et al., 2013; Montomoli et al., 2013). The High Himalayan discontinuity is a thrust that separates sillimanite-bearing gneiss and schist with peak pressures of 1.0-0.9 GPa in the hanging wall from kyanite-bearing gneiss and schist with peak pressures of 0.7 GPa in the footwall (Larson et al., 2010; Yakamchuk and Godin, 2012; Imayama et al., 2012; Montomoli et al., 2013; Carosi et al., 2013). After movement was accommodated along the High Himalayan discontinuity, GH rocks were transported southward along a shear zone, the MCT. In this study, the MCT is defined as the thrust fault that separates GH from LH rock. GH rocks have $\Sigma_{Nd}(0)$ values between -19 to -12 and LH rocks have $\Sigma_{Nd}(0)$ values between -20 to -26 (Martin et al., 2005). GH rocks have detrital zircon ages between ~1050 and ~480 Ma, and LH rocks have detrital zircon ages between ~1880 and ~1550 Ma (Gehrels et al., 2003, 2006; Martin et al., 2005). The metamorphic discontinuity between the GH and LH rocks is interpreted as a faulted contact (e.g., Robinson et al., 2006; Carosi et al., 2013; Montomoli et al., 2013; Martin, 2017) while other studies define the MCT as a strain discontinuity and place it further south in LH rock (e.g., Searle et al., 2008; Larson et al., 2010; Yakymhuk and Godin, 2012; Braden et al., 2017; 2018). $^{40}\text{Ar}/^{39}\text{Ar}$ cooling ages on muscovite ~49 km the west of the Simikot cross section suggests that movement along the MCT began ~25-21 Ma (DeCelles et al., 2001; Robinson et al., 2006). However, U-Pb ages in monazite ~51 km the east of the Simikot cross section is interpreted to date the initiation of motion on the MCT at ~17 Ma and was active until 13 Ma (Montomoli et al., 2013).

GH rocks were emplaced over and metamorphosed LH rocks in Early to Middle Miocene time (Robinson et al., 2003). The LH units include the Paleoproterozoic Kushma and Ranimata Formations, the Mesoproterozoic Sangram, Galyang, and Syangia Formations and the Lakharpata Group, the Late Paleozoic to Mesozoic Gondwana Group, and the Eocene to

Miocene, Bhainskati, and Dumri Formations (Table 1). The Ramgarh-Munsiari thrust (RMT) is a major intra-LH fault that translates Paleoproterozoic LH rocks (Kushma and Ranimata Formations) and GH rocks at least 100 km southward (DeCelles et al., 2001; Robinson and Pearson, 2013). Movement on the RMT is interpreted to have initiated after motion on the MCT ended around 13 Ma in a section ~51 km to the east of the Simikot cross section (Montomoli et al., 2013). Zircon rim age of 8 Ma (Braden et al., 2018) in an RMT imbricate thrust just ~1.5 km south of the RMT in the Simikot cross section suggests that movement on the RMT imbricate stopped before 8 Ma. Thus, the RMT may have formed and accommodated its total fault displacement somewhere between 13-9 Ma. Evidence of Paleoproterozoic LH rocks is first seen in the Siwalik Group at 10 Ma in the Karnali River section by a switch to more negative $\epsilon_{\text{Nd}}(\text{T})$ values (Huyghe et al., 2001; Szulc et al., 2006). The Lesser Himalayan duplex (LHD) is formed by a series of imbricate thrusts in the Lesser Himalayan imbricate zone forming a hinterland-dipping antiformal duplex (Robinson et al., 2006). Formation of the duplex must be between the end of motion on the RMT and 4-5 Ma, the age of the MBT (DeCelles et al., 1998b).

Synorogenic units deposited in the foreland basin of the Himalayan thrust belt in far-western Nepal include the LH Bhainsakti Formation and Dumri Formation, and the lower, middle, and upper units of the Siwalik Group (SH rocks). The Bhainskati Formation was deposited in Early to Middle Eocene time with the TH as the source (Fuchs and Frank, 1970; Sakai, 1983; DeCelles et al., 2001; Najman et al., 2005). The Dumri Formation was deposited from at least 19.9 to 15.1 Ma; it is unclear whether the TH or GH rocks or both are the source rocks (DeCelles et al., 2001; Najman et al., 2005; Ojha et al., 2009). The lower Siwalik unit was deposited 16 to 9.7 Ma with TH as the dominate source until 12 Ma when lithic fragments sourced from GH rocks first appear (Gautam and Fujiwara, 2000; DeCelles et al., 2001;

Robinson and McQuarrie, 2012). The middle Siwalik unit was deposited 9.7 to 4.6 Ma with a continued source of the TH and GH rocks and the first appearance of LH derived clasts at 10 Ma (Gautam and Fujiwara, 2000; Ojha et al., 2000; Huyghe et al., 2001; Szulc et al., 2006; Robinson and McQuarrie, 2012). The upper Siwalik unit was deposited from 4.6 Ma to present with the same sources as the middle Siwalik unit of TH, GH, and LH rocks (Quade et al., 1995; DeCelles et al., 1998a; DeCelles et al., 1998b; Nakayama and Ulak, 1999; Gautam and Fujiwara, 2000; Ojha et al., 2000, 2009).

GEOLOGICAL MAP OF FAR-WESTERN NEPAL

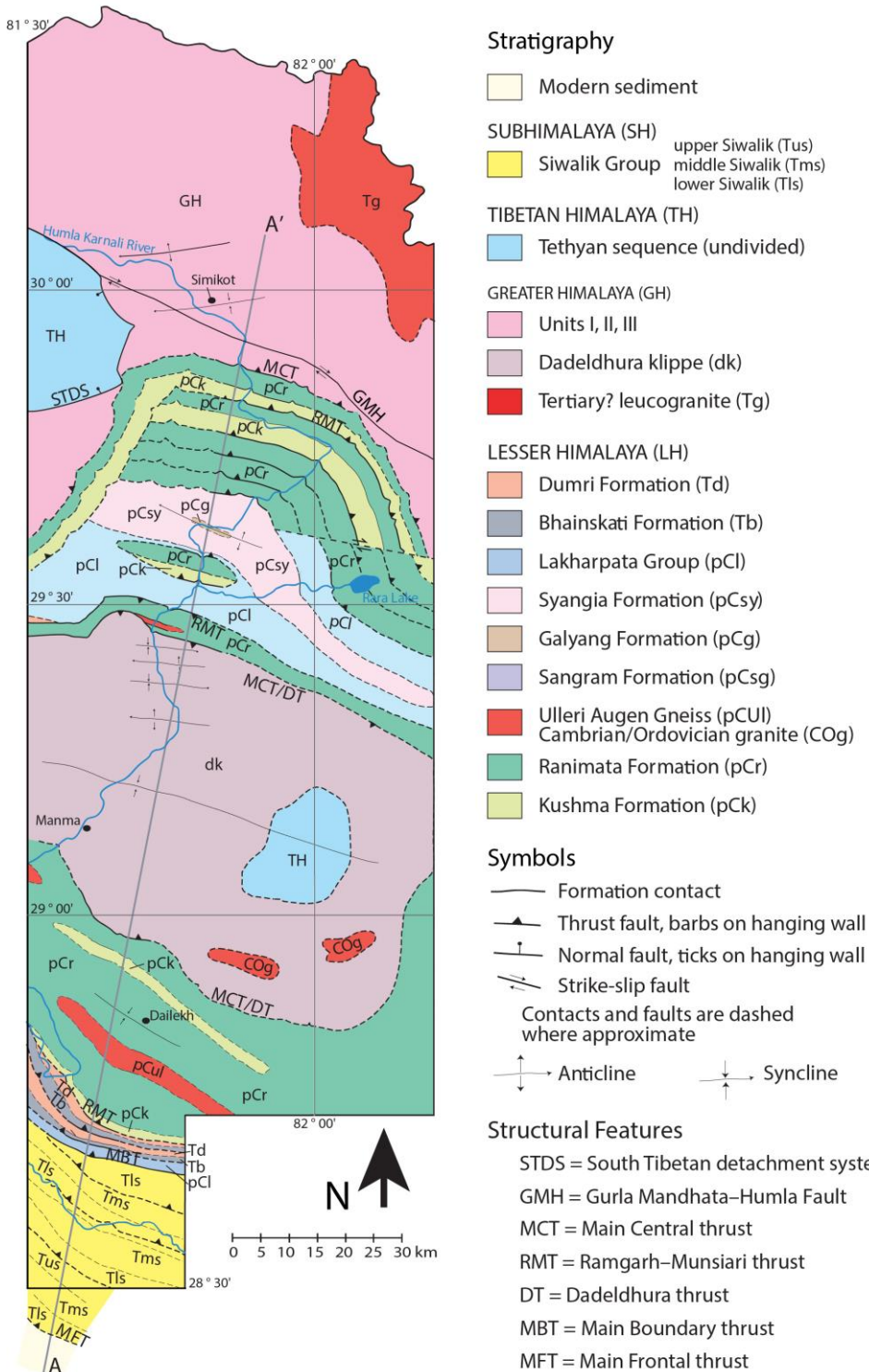


Figure 2: Geologic map of far-western Nepal, modified from Robinson et al. (2006). Simikot cross section A to A'.

2.1 Structural and Other Published Data

The structural data and balanced cross section are from Robinson et al. (2006) (Fig. 2).

Along the Simikot cross section from south to north, A to A' on Figure 2, the MFT marks the southern extent of the fold-thrust belt and separates the Quaternary sediments from the SH Neogene Siwalik Group. Three north-dipping thrust sheets within the Subhimalayan thrust system (SHTS) repeat stratigraphy of the three-part Siwalik Group and dip ~20-60°N (Robinson et al., 2006) and include the Main Dun thrust (Mugnier et al., 1999).

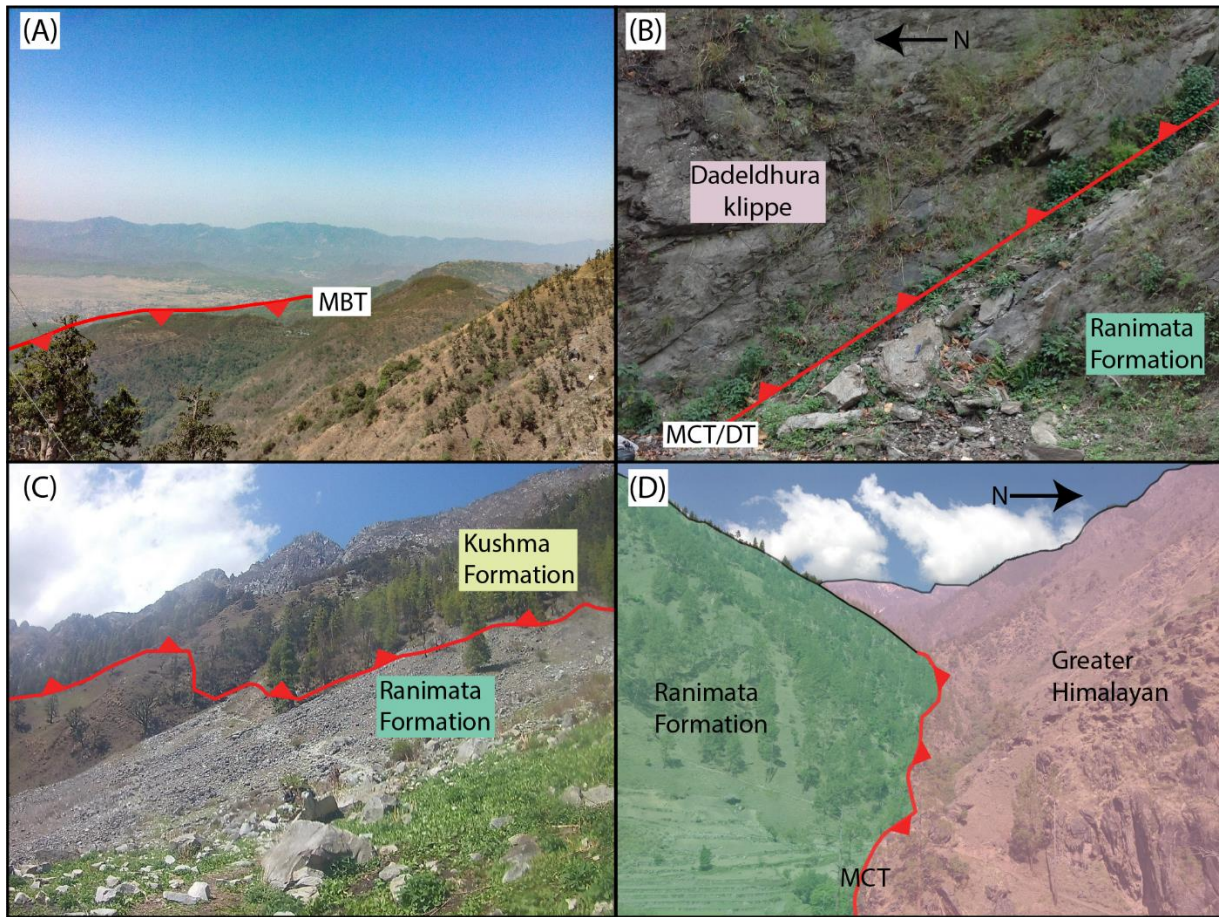


Figure 3: Field photos of major structures along the Simikot cross section. (A) View to the south of the MBT and Siwaliks hills in the distance. (B) MCT or DT fault at the base of the southern end of the DK separating LH rocks from the GH DK rocks. (C) Photo looking to the north at a LHD thrust fault separating Kushma Formation from Ranimata Formation. (D) MCT separating GH rock from LH rock.

The Main Boundary thrust (MBT) is the southern boundary of the Lesser Himalayan imbricate zone (LHZ) (Fig. 3A). The MBT places the LH Lakharpatra Group, Bhainskati Formation and Dumri Formation over the SH Siwalik Group, a north-dipping thrust of the LHZ repeats the LH Bhainskati and Dumri Formations. The LHZ is bounded to the north by the Ramgarh-Munsiari thrust (RMT).

The RMT is a major fault that translates the LH Kushma and Ranimata Formations at least 100 km southward (Robinson and Pearson, 2013). The RMT sheet of LH and GH rocks contains a syncline-anticline pair with a width of ~33 km along the section line due to this folding. The RMT sheet is folded underneath the Dadeldhura klippe with its root zone in the footwall of the MCT. North of the southern exposure of the RMT sheet, the Dadeldhura klippe (DK) is folded into an asymmetric syncline, and is bounded by a thrust that dips 35°N at the southern end of the klippe and 37°S at the northern extent of the klippe (Fig. 3B). The Dadeldhura klippe is comprised of medium-grade metamorphic rocks that are lithologically similar to GH rocks with ϵ_{Nd} values of -7.6 to -11.8 and U-Pb detrital zircon ages of ~900 Ma, indicating the klippe is a southern continuation of GH rocks (Robinson et al., 2001; Gehrels et al., 2003; Mandel et al., 2014). Thus, the DK is an erosional remnant of the MCT or another intra-GH fault. The greenschist to amphibolite facies GH rocks of the DK are overlain by non-metamorphosed calcareous sedimentary TH rocks (Arita et al., 1984; Hyashi et al., 1984). The TH rocks within the klippe, which are 18 km east of the cross section, either unconformably overlie GH rocks (Gehrels et al., 2003; 2006) or are separated by a fault (La Roche et al., 2016). Rocks at the base of this contact display a top-to-the-NE shear fabric interpreted as the STDS, with monzomite U-Pb ages indicating ductile shearing along the base of the STDS in the DK starting at 30 – 29 Ma and continuing until 19 Ma (La Roche et al., 2016). The top-to-the-north

Tila shear zone, north of the TH rocks within the DK, has also been interpreted as the STDS separating GH rocks from TH rocks, but this shear zone lacks a metamorphic discontinuity between hanging wall and footwall metamorphic grade (He et al., 2016; LaRoche et al., 2016). More work needs to be done on these contacts to determine if the STDS is present or not. Immediately north of the klippe along the cross section, the LH Ranimata Formation is present and its base is the RMT dipping 37°S.

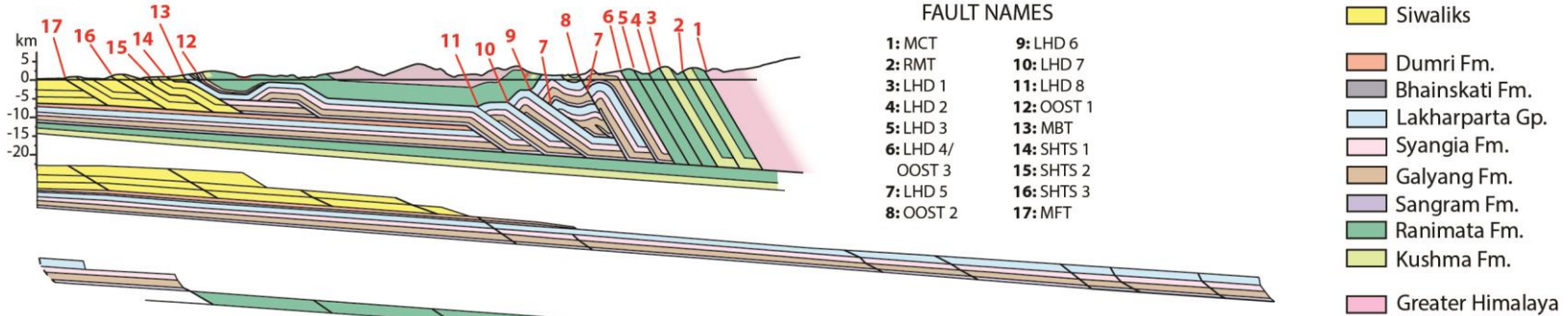
North of the RMT, the hinterland dipping LH duplex is exposed. The southern portion of the duplex consists of four thrust sheets that contain the Sangram, Galyang and Syangia Formations, and the Lakharpatra Group. The northern portion of the LH duplex is composed of four thrust sheets one with the LH Ranimata and Kushma formations and three with only the Ranimata Formation, which dip 50-60°N (Fig. 3C). The northernmost thrust sheet of the LH duplex is the root zone for the RMT sheet, which is the roof thrust for the LH duplex.

The MCT lies north of the RMT sheet; this major north-dipping thrust separates GH from LH rocks (Heim and Gansser, 1939) (Fig. 3D). GH rocks are amphibolite-facies metasedimentary and metaigneous rocks. Intra-GH thrusts were active from ~28-26 to 17 Ma (Montomoli et al., 2013; Carosi et al., 2013). GH rocks have a metamorphic pressure gradient that decreases upsection from 10 to 5 kbar (Yakymchuck and Godin, 2012). Foliations north of the MCT and LH rocks south of the MCT are parallel, indicating that the relationship between the underlying LH rocks as the GH thrust sheet was translated over top is likely a hanging wall flat on top of a footwall flat (Robinson et al., 2003; 2006).

The Southern Tibetan detachment system (STDS) marks the northern most extent of the GH rocks. The STDS is a large detachment fault with TH rocks in the hanging wall and GH rocks in the footwall. Within the TH rocks, the Gurla Mandhata- Humla fault system is a strike-

slip system that acts as an extensional stepover that was active after 15 Ma with a minimum slip of 24.4 to 32.4 km and a slip rate of ~5 to 3 mm yr⁻¹ (Murphy and Copeland, 2005; McCallister et al., 2014). Movement along the STDS near Gurla Mandhata possibly continued until ~9 Ma (Murphy et al., 2002). If the DK contains the STDS, the shear zone has basal ductile shearing starting at 30 – 29 Ma and continuing until 19 Ma (La Roche et al., 2016). In the cross section, the STDS lies north from the mapped extent of Robinson et al. (2006).

(A) Simikot Cross Section and Restoration from Robinson et al. (2006)



(B) Simikot Cross Section and Restoration from Olsen et al. (2018)

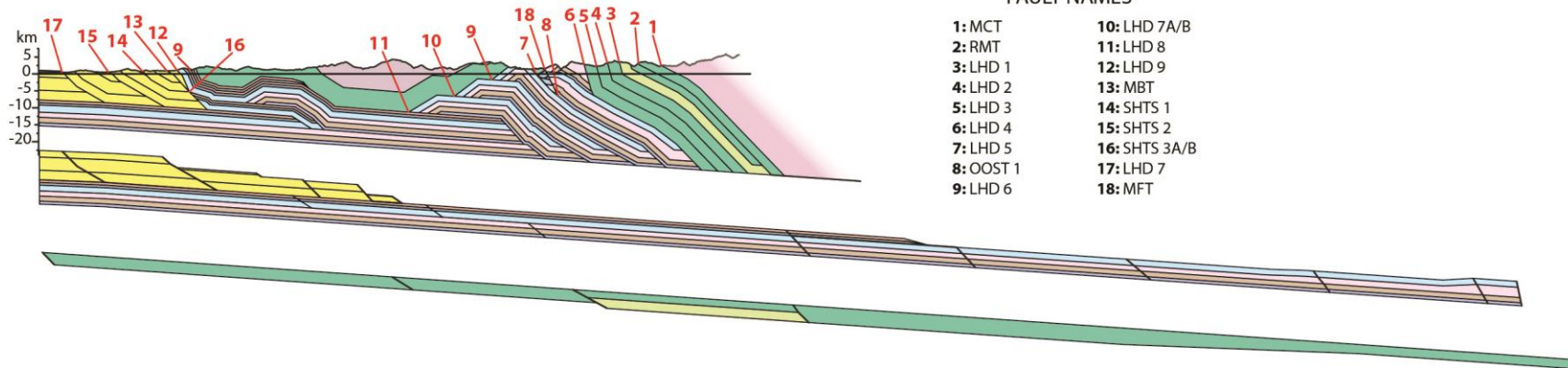


Figure 4: (A) Balanced Simikot cross section from Robinson et al. (2006) with restored section below. (B) Modified version of the Simikot cross section from Olsen et al. (2018) with restored section below.

2.2 Balanced Cross Sections

Balanced cross sections have a geometrically viable subsurface geometry in a fold-thrust belt. This study examines the Simikot cross section from Robinson et al. (2006) along with a modified version of this same section from Olsen et al. (2018). The Robinson et al. (2006) version has a single ramp in the décollement with the top at ~110 km and the bottom ~120 km north of the MFT (Fig. 4A). The modified version of Olsen et al. (2018) has an altered footwall geometry that places ramps in regions of physiographic transition (Fig. 4B) as explained by Harvey et al. (2015). These regions have active uplift through observations of high river steepness indices and seismic patterns suggesting that footwall ramps are likely located under these areas of physiographic transition (Harvey et al., 2015). The Olsen et al. (2018) version has two ramps in the décollement, one between 75 and 80 km north of the MFT and the other between 145 and 150 km north of the MFT (Fig. 4B). The different décollement geometries of Robinson et al. (2006) and Olsen et al. (2018) cross sections imply a different kinematic sequence of faulting, different rocks exhuming at different times and different shortening rate estimates for the two cross sections. Throughout this study, I will refer to the cross sections as the Robinson et al. (2006) and Olsen et al. (2018) cross sections. These studies provide the balanced cross sections; however, all subsequent modeling of these cross sections is new in this study.

2.3 Thermochronologic Data

$^{40}\text{Ar}/^{39}\text{Ar}$ of muscovite (MAr), (U-Th)/He of zircon (ZHe), apatite fission track (AFT), and zircon fission track (ZFT) thermochronology ages from McCallister et al. (2014), Sakai et al. (2013), van der Beek et al. (2016), and unpublished data from Harvey (2015) and Mercier (2014)

are used. Ages are reported as the mean age with a 2σ error (Table 2). All of the ages are from within 20 km east or west of the cross section line and are projected to the line along strike of the rock units.

Table 2: Published MAr, ZHe, AFT, and AHe cooling ages along Simikot cross section

Sample ID	Thermochronometer	Latitude (°N)	Longitude (°E)	Elevation (m)	Cooling Age (Ma)
<u>McCallister et al. (2014)</u>					
zHUM02-10	ZHe	30.03698	81.81368	2900	3.45 ± 0.32
zHUM02-11	ZHe	30.03767	81.81655	2900	3.92 ± 0.97
zHUM02-12	ZHe	30.04433	81.82827	3200	4.22 ± 0.81
zHUM02-13	ZHe	30.04425	81.82833	3190	3.97 ± 0.50
<u>Sakai et al. (2013)</u>					
94112701a	AFT	28.71983	81.69167	870	10.3 ± 0.5
94112409	AFT	28.68017	81.63900	2170	14.4 ± 2.2
<u>van der Beek et al. (2016)</u>					
KAR02	AFT	29.96325	81.82745	2840	8.5 ± 1.7
KAR04	AFT	29.94185	81.85353	2115	1.3 ± 0.3
KAR07	AFT	29.90685	81.88775	2080	3.3 ± 1.0
KAR14	AFT	29.86348	81.87530	1940	2.0 ± 0.4
KAR15	AFT	29.86348	81.87530	1940	1.4 ± 0.3
KAR55	AFT	29.47520	81.71401	1085	7.0 ± 1.0
KAR57	AFT	29.44860	81.70600	1145	7.8 ± 1.5
KAR59	AFT	29.40070	81.71545	1085	6.2 ± 0.5
KAR62	AFT	29.13928	81.58005	780	8.9 ± 1.5
KAR68	AFT	29.08008	81.47740	690	6.2 ± 0.5
<u>Harvey (2015)</u>					
SIM11-RT3-1	AHe	29.9619	81.7977	2225	2.3 ± 0.51
SIM11-RT3-1	ZHe	29.9619	81.7977	2225	2.5 ± 0.47
SIM11-RT3-2	ZHe	29.9584	81.7939	2400	2.1 ± 0.26
SIM11-RT3-4b	AHe	29.9536	81.7968	2729	1.3 ± 0.13
SIM11-RT3-4b	ZHe	29.9536	81.7968	2729	2.3 ± 0.88
SIM11-RT3-4a	AHe	29.9505	81.7981	2943	2.4 ± 0.80
SIM11-RT3-4a	ZHe	29.9505	81.7981	2943	2.3 ± 0.15
SIM11-RT3-3	AHe	29.9534	81.7879	2600	1.1 ± 0.16
SIM11-RT3-3	ZHe	29.9534	81.7879	2600	2.4 ± 0.60
SIM11-RT3-6	ZHe	29.9478	81.7964	3214	2.3 ± 0.42
SIM11-RT3-7	AHe	29.9454	81.7965	3429	2.3 ± 0.58
SIM11-RT3-7	ZHe	29.9454	81.7965	3429	2.2 ± 0.18
JUM13-RT3-0	AHe	29.1406	81.7916	1595	10.2 ± 1.32

Sample ID	Thermochronometer	Latitude (°N)	Longitude (°E)	Elevation (m)	Cooling Age (Ma)
<u>Harvey (2015) (contd.)</u>					
JUM13-RT3-0	ZHe	29.1406	81.7916	1595	10.6 ± 1.20
JUM13-RT3-1	AHe	29.1489	81.7876	1830	9.3 ± 2.17
JUM13-RT3-1	ZHe	29.1489	81.7876	1830	9.9 ± 0.52
JUM13-RT3-2	AHe	29.1552	81.7906	2086	8.8 ± 0.29
JUM13-RT3-2	ZHe	29.1552	81.7906	2086	11.4 ± 1.20
JUM13-RT3-3	AHe	29.1652	81.7887	2477	10.3 ± 3.50
JUM13-RT3-3	ZHe	29.1652	81.7887	2477	13.0 ± 2.68
JUM13-RT3-4	AHe	29.1729	81.7903	2735	8.4 ± 2.17
JUM13-RT3-4	ZHe	29.1729	81.7903	2735	10.5 ± 0.61
JUM13-RT3-5	AHe	29.1807	81.7950	3035	6.4 ± 2.59
JUM13-RT3-5	ZHe	29.1807	81.7950	3035	11.2 ± 0.75
JUM13-RT3-6	AHe	29.1851	81.7866	3339	7.5 ± 1.88
JUM13-RT3-6	ZHe	29.1851	81.7866	3339	10.9 ± 0.45
JUM13-RT3-8	AHe	29.1969	81.7799	3909	11.4 ± 1.28
JUM13-RT3-8	ZHe	29.1969	81.7799	3909	11.6 ± 0.86
JUM13-RT3-9	AHe	29.2050	81.7793	4190	9.6 ± 0.90
JUM13-RT4-2	AHe	29.1692	81.6193	1118	7.4 ± 2.68
JUM13-RT4-3	AHe	29.1663	81.6235	1366	9.9 ± 1.65
JUM13-RT4-4	AHe	29.1613	81.6238	1533	8.4 ± 1.73
JUM13-RT4-4	ZHe	29.1613	81.6238	1533	12.6 ± 3.10
JUM13-RT4-5	AHe	29.1588	81.6194	1760	8.7 ± 2.63
JUM13-RT4-5	ZHe	29.1588	81.6194	1760	12.2 ± 2.05
JUM13-RT4-6	ZHe	29.1518	81.6234	2199	11.7 ± 0.73
JUM13-RT4-7	AHe	29.1469	81.6339	2555	5.2 ± 1.33
JUM13-RT4-7	ZHe	29.1469	81.6339	2555	12.3 ± 0.43
<u>Mercier (2014)</u>					
KAR11-007	Mar	29.93784	81.88522	2620	6.16 ± 0.06
KAR11-028	Mar	29.73382	81.83265	2489	5.85 ± 0.67
KAR11-064	Mar	29.12493	81.56487	728	16.92 ± 0.33
KAR11-069	Mar	29.07970	81.46932	687	18.60 ± 1.80

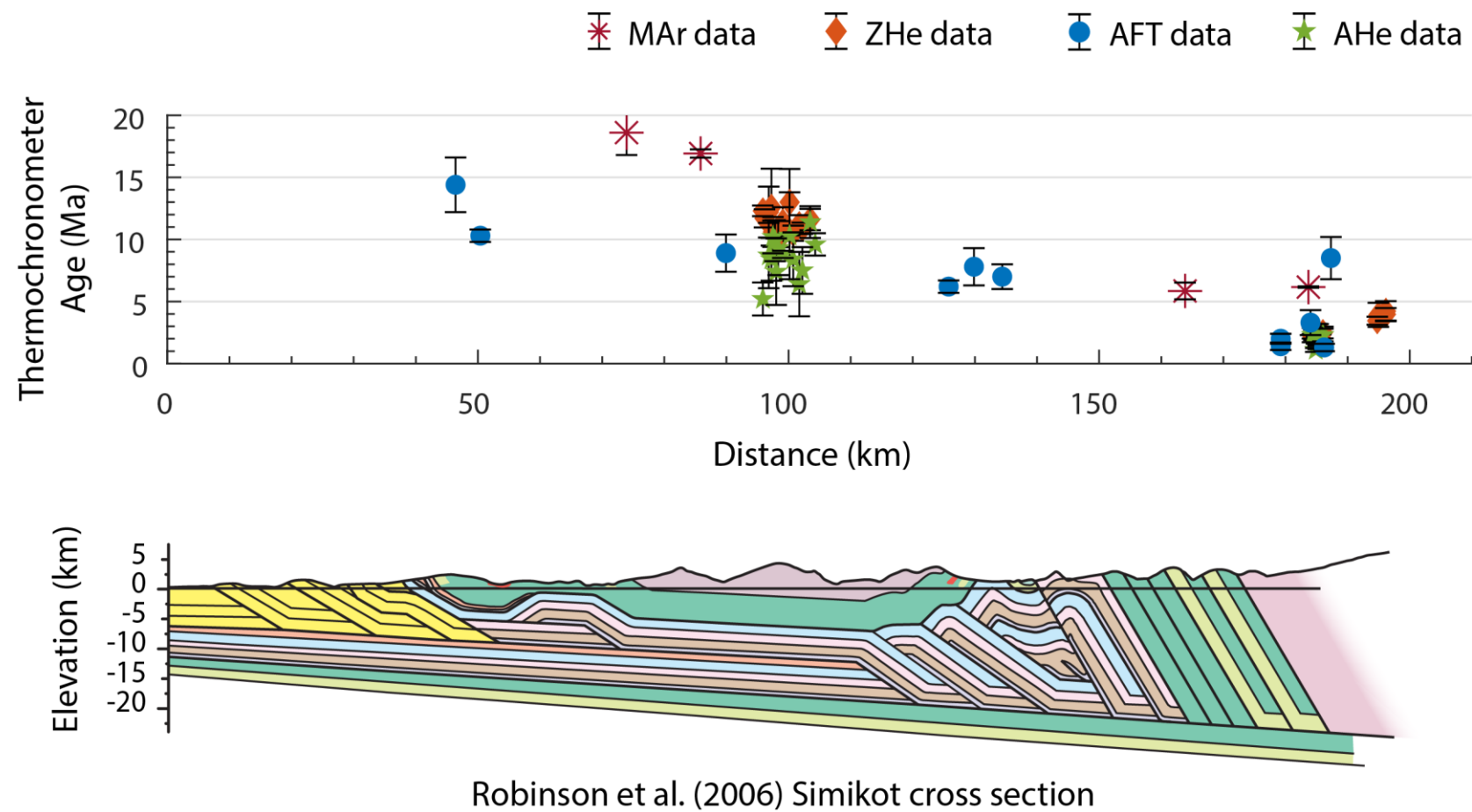


Figure 5: Published MAr, ZHe, AFT, and AHe thermochronometer cooling ages with 2σ error along Simikot cross section from Robinson et al. (2006). Data from McCallister et al. (2014), Sakai et al. (2013), van der Beek et al. (2016), and unpublished data from Harvey (2015) and Mercier (2014).

3. METHODS

3.1 Sample Collection

The GH and LH units along the Simikot section were sampled during 10 days of geologic mapping along the Karnali River (Fig. 2). Appendix A shows the new mapping conducted during this field season. However, in this study, I use the map and cross section from Robinson et al. (2006) and the cross section from Olsen et al. (2018).

The main purpose of the field work was to collect samples to supplement the already existing apatite fission track (AFT), zircon (U-Th)/He (ZHe), and $^{40}\text{Ar}/^{39}\text{Ar}$ of white mica (MAr) samples (Table 2). Rock samples were collected in some of the same locations as those in Table 2 and in areas where there are no samples to fill the gaps in data. Six new samples were analyzed for AFT, and 14 samples were analyzed for ZHe. Appendix B lists each sample, description, and location. Zircon and apatite grains were separated from the samples using the facilities at the University of Alabama. The minerals were separated by crushing, pulverizing, sieving, density separation with heavy liquids LST and MEI, and magnetic separation with a Frantz (e.g., Gehrels et al., 2008). However, due to delays in obtaining the analyses, the results are not included in this study. Instead, we use only the existing thermochronologic data in Table 2 and will incorporate the ZHe and AFT analyses into future work.

3.2 Flexural and Kinematic Model

3.2.1 Kinematic Analysis

Inherently, each balanced cross section has an implied kinematic sequence. The first phase of modeling is to forward model the restored balanced cross section to its present geometry via the kinematic sequence required by the cross section. The restored balanced cross section was scanned, scaled, and digitized in 2D Move with lines representing stratigraphy, faults, and topography. The faults were sequentially deformed with the “fault-parallel flow” algorithm, which translates the stratigraphy in hanging wall parallel to the user defined fault surface, while the stratigraphy in the footwall remains undeformed. In all models, the thrust sheets were treated as a rigid bodies lacking internal strain. The amount of permissible displacement per fault was estimated from the balanced cross section. The displacement used varies from the estimate by up to several kilometers.

3.2.2 Initial Model Configuration

The balanced cross sections from Robinson et al. (2006) and Olsen et al. (2018) are drawn with the décollement at its present day depth and dip and all synorogenic sedimentary rocks deposited below present day surface (0 km) (Fig. 4). Before flexural modeling, the balanced cross sections were restored to the best estimate for the initial configuration of the Indian passive margin (Fig. 6A). The initial model configuration was restored to the Indian margin configuration after the formation of the Tethyan fold-thrust belt but before the initiation of the MCT so the flexural and isostatic response of the upper crust throughout the building of the Himalayan fold-thrust belt can be modeled. The LH units are overlain by wedge-shaped TH rocks with a topographic taper angle of 2° up to an elevation of 5 km above sea level and then

the topography levels out at 5 km (DeCelles et al., 2007; Hetzel et al., 2011; Rohrmann et al., 2012). This wedge shaped geometry of TH rocks represents the Tethyan fold-thrust belt as a coulomb wedge; individual faults within this thrust belt are not represented, and it is treated as a cohesive unit. The LH stratigraphic basin that composes the Indian passive margin gently dips northward (0.6-1.3°). The Bhainskati and Dumri formations and all SH units are above sea level in the original configuration because they are synorogenic units that are deposited later as the foreland basin forms. The top of the Lakharparta Group was lowered to a depth of -0.31 km for the Robinson et al. (2006) cross section and -1.84 km for the Olsen et al. (2018) cross section to prevent the erosion of the Proterozoic LH units as the forebulge migrated southward in the model. The length of all stratigraphic units in the restored section was extended by 65 km at the southern end and 100 km at the northern end to eliminate any edge effect from the flexural and thermokinematic modeling (see section 3.2.3 and 3.3).

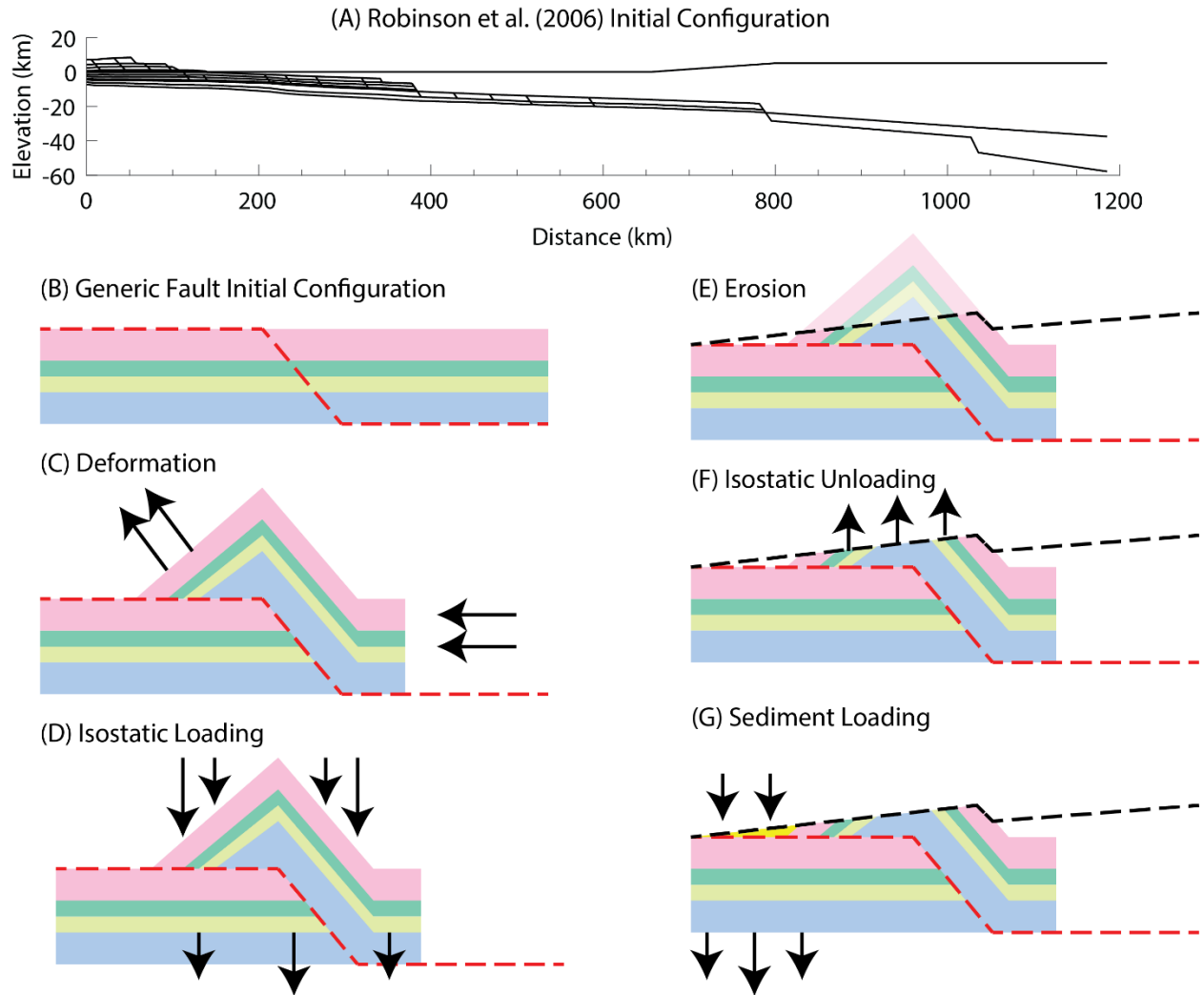


Figure 6: (A) Initial configuration of the Robinson et al. (2006) model, shown as an example of the initial model configuration of the Move models. (B-G) Simplified illustration of isostatic response to deformation and erosion. (B) Simplified restored cross section with future fault (red dashed line). (C) Motion on fault. (D) Isostatic loading (black arrows) of material moved by fault. (E) Erosion of material above new topography (black dashed line) generated using critical wedge angle. (F) Isostatic unloading (black arrows) from removal of eroded materials mass. (G) Sediment loading from deposition of sediments in the foreland basin.

3.2.3 Flexural Isostasy Model

The fault displacements obtained from the kinematic model were divided into approximately 10 km incremental steps and starting with the initial cross section configuration described in the previous section, each incremental step was deformed along the active fault,

flexurally loaded from thrust faulting, and isostatically unloaded after erosion (Fig. 6). Along with this, a 0.5 X 0.5 km grid of unique points was also sequentially deformed to produce vectors of displacement used in later thermokinematic modeling (see section 3.3). Deformation along a fault created a new uplifted topographic surface with the uplift concentrated above ramps in the décollement and at the deformation front (Figs. 6B & 6C). The vertical difference between the initial topographic surface and the newly deformed topographic surface represented the size and distribution of the load imposed by thrust faulting that must be flexurally accommodated. The magnitude of load was calculated from the difference in the area of the deformed topography from the area of the original topography before the deformation (McQuarrie and Ehlers, 2015) (Fig. 6D). The flexural load caused the depth and angle of the décollement to increase along with the depth and width of the foreland basin. As the foreland basin deepened due to the flexural response, the deformation front migrated southward towards the foreland basin.

In 2D Move, the “compaction” feature within the “decompaction module” calculated compaction. This module distributed the isostatic load over a wavelength that was determined by flexural properties of the lithosphere. Equations from Turcotte and Schubert (1982) were used to calculate the deflection caused by a line load on an infinite plate using the load density, effective elastic thickness (EET) of the plate, mantle density, and Young’s modulus. The load density and EET values were systematically varied by the user to best recreate the present day surface geology, foreland basin depth, and décollement angle (section 3.2.4 details parameters used)

The resulting deformed loaded topography was used to calculate the magnitude of erosion and create a new topographic profile. The deformed loaded topographic profile was exported from Move and run through the Python script “makeTopo”. This script created a new topographic profile using a user-specified topographic angle and the location of the deformation

front. The new topographic profile was at 0 km in elevation at the MBT and increased northward to the deformation front at the topographic angle set by the user, which could also be varied. The elevation of this line never exceeded 6.5 km to set a maximum elevation for topography realistic for the Himalaya. The topographic angle was systematically varied to best match the cross section geometry (see section 3.2.4). Material above this new topographic profile was eroded and area created below sea level in the foreland basin filled with sediment eroded from the fold-thrust belt (Fig. 6E).

All area above the new eroded topographic line was removed, which induced a flexural response of the lithosphere. In the model, erosional unloading was determined by the vertical difference in the area of the deformed isostatically loaded topography and the area of the new topographic profile that resulted from erosion (McQuarrie and Ehlers, 2015) (Fig 6F). In 2D Move, decompression was calculated using the same “decompression module” used to calculate the compaction. Erosional unloading resulted in an upward rebound of the décollement and foreland basin.

Flexural loading and erosional unloading were applied to ~10 km incremental step for the Robinson et al. (2006) cross section, which had 87 steps. In addition, a sediment loading step was applied to the 90 incremental steps of the modified version from Olsen et al. (2018) section to determine the effect it had on foreland basin development (see section 4.2.1). The sediment load step was applied after the deformed section was loaded, eroded, and unloaded. This load was applied to the foreland basin and any piggyback basins that may form. The magnitude of sediment loading was determined with the difference vertical area between the deformed unloaded topography and the new eroded topography line (Fig. 5G).

3.2.4 Model Parameters

Table 3: Flexural-kinematic model parameters tested in 2D-Move

Model name	EET (km)	Crustal density (g m ⁻³)	Sediment density (g m ⁻³)	Topography erosion angle (°)	Decollement dip (°)	Foreland basin thickness (km)
Robinson et al. (2006) Simikot cross section						
SimiFlex1	100	2850	N/A	1.6	6.9	6.8
SimiFlex2	90	2850	N/A	1.6	6.8	6.7
SimiFlex3	90	2700	N/A	1.6	6.7	6.5
SimiFlex4	95	2600	N/A	1.6	6.1	5.1
SimiFlex5	100	2600	N/A	1.6	6.1	5.3
SimiFlex6	100	2600	N/A	1.4	6.1	5.2
SimiFlex7	100	2650	N/A	1.3	6.1	5.5
SimiFlex8	100	2700	N/A	1.2	6.0	5.4
SimiFlex9	100	2700	N/A	1.4	6.1	6.2
SimiFlex10	105	2650	N/A	1.3	5.4	5.8
SimiFlex11	105	2700	N/A	1.3	5.3	6.3
SimiFlex12	110	2700	N/A	1.3	5.3	6.1
Olsen et al. (2018) Simikot cross section						
SimiFlex39	95	2500	2300	1.75	3.9	7.4
SimiFlex40	95	2550	2300	1.75	4.6	7.2
SimiFlex41	95	2600	2300	1.75	4.1	7.6
SimiFlex42	95	2600	2350	1.75	4.5	7.9

Effective elastic thickness (EET), crustal bulk density, and the topographic angle were varied and tested throughout the flexural modeling process to improve the fit of the modeled cross section to the: (1) observed surface geology, (2) thickness of the foreland basin deposits, and (3) dip of the MHT décollement. If any of these three features did not match when comparing the final step of the modeled cross section was compared to the balanced cross section, the model was run again with different parameters. The range of parameters tested in the flexural model was within the range of acceptable values for the Himalaya (Karner and Watts 1983; Bai et al., 2013; Chen et al., 2015). Table 3 shows the values tested for both the Robinson et al. (2006) and the Olsen et al. (2018) cross sections along with the resulting décollement dip

and foreland basin thickness. Twelve different flexural models were created for the Robinson et al. (2006) section with one matching all the criteria and four were created the Olsen et al. (2018) section with one best-fit model. The best fit models are highlighted in grey on Table 3.

3.3 Thermokinematic Modeling

The 0.5 X 0.5 km grid of unique points and topographic profile for each incremental step of the flexural isostasy model were exported from 2D Move and used to create the thermokinematic model. The grid of points tracks movement of material through the subsurface to the surface defined by the topographic profile. These data were the input for creating the thermal structure model in a University of Tübingen modified version of Pecube (Braun, 2003; Whipp et al., 2009; McQuarrie and Ehlers, 2015). Pecube solves a transient 3D heat transfer equation that derives the time-temperature history of exhumed rocks based on their transport path throughout an imposed tectonic history. The time-temperature path was used to calculate predicted thermochronometric ages for a suite of low temperature thermochronometers using approaches described in Ehlers et al. (2005) and Braun (2003).

The 2D model extended 1250 km horizontally to represent the Indian passive margin (1085 km) and extended to a depth of 110 km to include all of the lithosphere. Constant temperature boundaries were applied at the surface and the base. Temperatures at sea level were 24.7° C (yearly average temperature in Nepalganj, Nepal) and decreased with elevation at a rate of 6° C km⁻¹, the mean lapse rate measured in the western Himalaya (Jain et al., 2008). The lithospheric basal temperature was held at 1300° C at 110 km, similar to previous studies (Jiménez-Munt and Platt, 2006; McQuarrie and Ehlers, 2015). Radiogenic heat production (A_0) was varied from 2 to 3 $\mu\text{W m}^{-3}$ (Herman et al., 2010). In the model, thermal conductivity was set

to 2.5 W mK^{-1} , specific heat capacity at 800 J kgK^{-1} , and e-fold depth of crustal heat production was set at 20 km (Table 4); these values are global averages for crustal rocks (Ehlers et al., 2005). In the model, vertical movement on faults advects heat upward, rapid erosion of material results in isotherms near the surface (e.g., Lock and Willett, 2008), and rapid sedimentation in the foreland results in isotherms far from the surface (e.g., Husson and Moretti, 2002).

Table 4: Pecube thermokinematic properties

	Model Input Value
Material Properties	
Crustal volumetric heat production	$2.0 \text{ to } 3.0 \mu\text{W m}^{-3}$
e-fold depth	20 km
Thermal conductivity	2.5 W mK^{-1}
Specific heat	800 J kgK^{-1}
Numerical Properties	
Temperature at base	1300° C
Model base	110 km
Surface temperature at 0 km	24.7° C
Atmospheric lapse rate	6° C/km
Kinematic grid spacing	0.5 km
Displacement increment	10 km
Model domain	$1250 \times 110 \times 5 \text{ km}$
Horizontal node spacing (numerical model)	0.5 km
Vertical node spacing (numerical model)	1.0 km
Model start time	50 Ma

In Pecube, a range of radiogenic heat productions and velocities for fault movements were tested to compare the effects of radiogenic heat production, fault timing, and deformation rates on the modeled cooling ages. Table 5 summarizes the different velocity rates and deformation ages tested (See Appendix C for timing of deformation on each individual fault). All models began at 50 Ma with the MCT deformation starting at 25 Ma (DeCelles et al., 2001; Robinson et al., 2006). For both cross section models, a constant velocity model was ran

assuming a constant rate of shortening along all faults from 25 Ma to 0 Ma. Variable velocity models A through E were run for the Robinson et al. (2006) cross section and velocity models F through I were run for the Olsen et al. (2018) cross section (Table 5). For Velocity A and F, fault deformation timing was constrained by data from previous studies introduced in Section 2. Velocity B and G were based on the deformation ages and velocity rates introduced in Robinson and McQuarrie (2012) for far-western Nepal. For Velocity C, D, E, H, and I the velocity rates were systematically changed to speed up or slow down displacements on faults to better match the modeled ages to the observed ages. Table 5 summarizes time displacement occurred and the velocity rate that it occurred in the various velocity models.

Table 5: Deformation ages and rates tested for thermokinematic models

Robinson et al. (2006) model																			
Fault System	Displacement (km)	Constant velocity			Velocity A			Velocity B			Velocity C			Velocity D			Velocity E		
		Start age (Ma)	End age (Ma)	Velocity ty (mm yr ⁻¹)	Start age (Ma)	End age (Ma)	Velocity ty (mm yr ⁻¹)	Start age (Ma)	End age (Ma)	Velocity ty (mm yr ⁻¹)	Start age (Ma)	End age (Ma)	Velocity ty (mm yr ⁻¹)	Start age (Ma)	End age (Ma)	Velocity ty (mm yr ⁻¹)	Start age (Ma)	End age (Ma)	Velocity ty (mm yr ⁻¹)
MCT	252	25.0	17.4	33.2	25.0	13.0	21.0	25.0	20.0	50.4	25.0	20.0	50.4	25.0	22.0	84.0	28.0	24.0	63.0
RMT	185.9	17.4	11.8	33.2	13.0	9.0	46.5	20.0	16.0	46.5	20.0	16.1	47.6	22.0	17.3	39.7	24.0	19.7	43.3
LHD	302.49	11.8	2.7	33.2	9.0	5.0	72.6	16.0	5.0	48.5 - 15.6	16.1	10.0	47.6	17.3	10.0	39.7	19.7	13.0	43.3
SHTS & OOST	88.4	2.7	0.0	33.2	5.0	0.0	20.1	5.0	0.0	17.7	10.0	0.0	10.1	10.0	0.0	10.1	13.0	0.0	7.7

Olsen et al. (2018) model																
Fault System	Displacement (km)	Constant velocity			Velocity F			Velocity G			Velocity H			Velocity I		
		Start age (Ma)	End age (Ma)	Velocity ty (mm yr ⁻¹)	Start age (Ma)	End age (Ma)	Velocity ty (mm yr ⁻¹)	Start age (Ma)	End age (Ma)	Velocity ty (mm yr ⁻¹)	Start age (Ma)	End age (Ma)	Velocity ty (mm yr ⁻¹)	Start age (Ma)	End age (Ma)	Velocity ty (mm yr ⁻¹)
MCT	220.5	25.0	18.7	35.0	25.0	13.0	18.4	25.0	20.0	44.1	25.0	20.0	44.1	25.0	18.0	31.5
RMT	205.65	18.7	12.8	35.0	13.0	9.0	51.4	20.0	16.0	51.4	20.0	16.4	57.1	18.0	15.1	71.4
LHD	379	12.8	2.0	35.0	9.0	5.0	91.4	16.0	5.0	52.2 - 28.9	16.4	10.0	57.1	15.1	10.0	71.4
SHTS & OOST	69.4	2.0	0.0	35.0	5.0	0.0	16.7	5.0	0.0	16.7	10.0	0.0	8.3	10.0	0.0	8.3

4. RESULTS

4.1 Robinson et al. (2006) Simikot cross section

4.1.1 Flexural-kinematic model

Table 6: Simikot cross section Robinson et al. (2006)
flexural-kinematic model displacement.

Fault	Step	Displacement (km)	Cumulative Displacement (km)
	A	0	0
MCT	B	252	252
RMT	C	185.9	437.9
LHD 1	D	66.9	504.8
LHD 2	E	36.65	541.45
LHD 3	F	36.35	577.8
LHD 4	G	36.35	614.15
LHD 5	H	48.5	662.65
LHD 6	I	31.7	694.35
LHD 7	J	19.7	714.05
LHD 8	K	14.2	728.25
MBT	L	12.14	740.39
SHTS 1	M	21.7	762.09
SHTS 2	N	15.8	777.89
SHTS 3	O	17.6	795.49
MFT	P	13.9	809.39
OOST 1	Q	2.9	812.29
OOST 2	R	11	823.29
OOST 3	S	5.5	828.79

Table 6 lists the minimum shortening estimates of the Robinson et al. (2006) Simikot cross section based on the regional cross section and shortening amounts determined from the flexural-kinematic modeling. The minimum initial length of the undeformed Indian passive

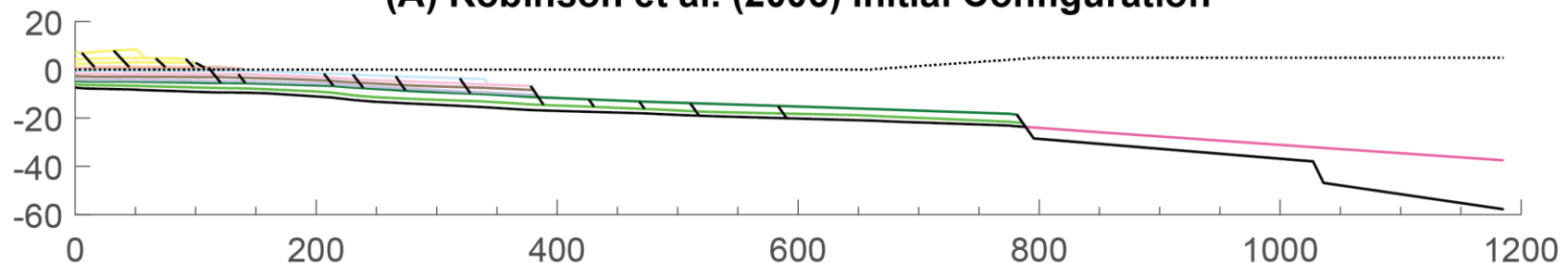
margin from the future location of the MFT to the northernmost extent of the GH rocks is 1180.40 km (Robinson et al., 2006). The cross section predicts 817-919 km of total shortening (Robinson et al., 2006). The total shortening determined by the flexural-kinematic model is 828.79 km. The final length of the cross section from the MFT to the northernmost extent of the GH is 351.61 km. Therefore, the total shortening is ~70% of the original length of the undeformed cross section. The displacement along this section can be divided into five major fault systems consisting of multiple individual thrust sheets, these include: the MCT, the RMT, the LHD thrust sheets, the SHTS, and out-of-sequence thrust (OOST) faulting. Table 6 lists the shortening amount on each of these individual thrust sheets.

Figure 7A shows the initial configuration of the model. This model begins at 25 Ma at the onset of the MCT or another intra-GH fault. Shortening that occurred in the Tethyan thrust belt is not included. The MCT accounts for 30% of the total minimum shortening (Fig. 7B). The RMT accommodates 22% of the total shortening (Fig. 7C) The nine faults of the LHD, including the MBT accommodate 37% of the total shortening (Fig. 7D-L) Four thrust sheets of the SHTS including the MFT account for 9% of the total shortening (Fig. 7M-P). Finally, there are three late OOST faults that accommodate 2% of the total shortening (Fig. 7Q-S). GH rocks are exposed after 682.65 km of shortening during movement on thrust sheet LHD 6 and was deposited in the foreland basin lower and middle Siwalik units. LH rocks are exposed after 740.39 km of shortening during movement on the MBT and was deposited in the foreland basin middle and upper Siwalik units.

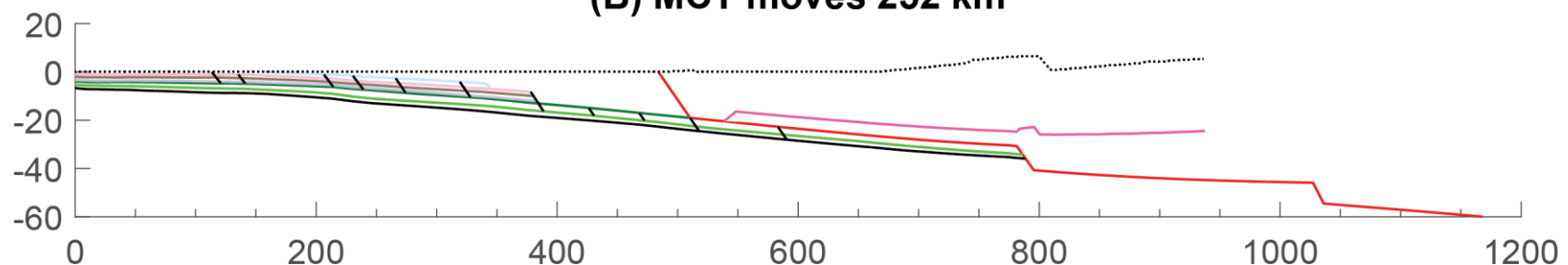
The EET, bulk density, and topographic angle were changed methodically to find a flexural-kinematic model that best matched the surface geology, dip of décollement, and depth of foreland basin. Table 3 summarizes the 12 flexural-kinematic models with the various

parameters tested with the final best fit model highlighted. The parameters for the best fit model are a bulk density of 2700 kg m^{-3} , an EET of 110 km, and a topographic erosion angle of 1.3° . This resulted in a foreland basin depth measured from the top of the MFT ramp of 6.1 km compared to 6.4 km in the original section, and a décollement dip of 5.3° compared to the 4.6° in the original section.

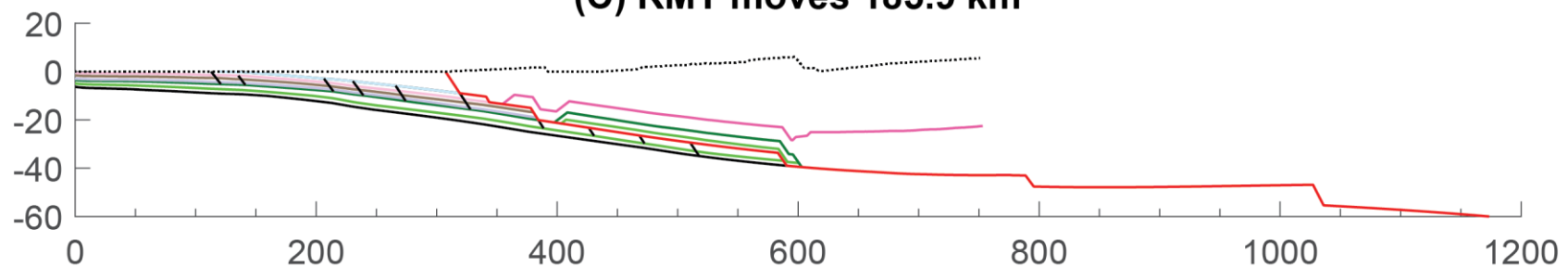
(A) Robinson et al. (2006) Initial Configuration



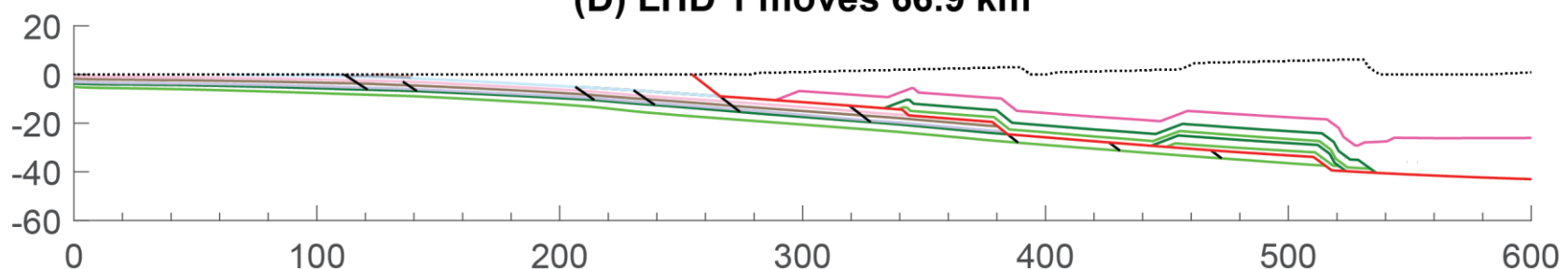
(B) MCT moves 252 km



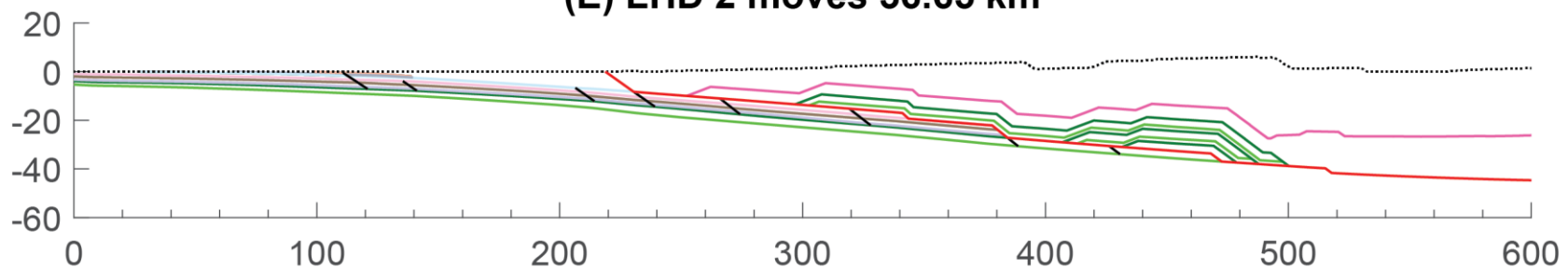
(C) RMT moves 185.9 km



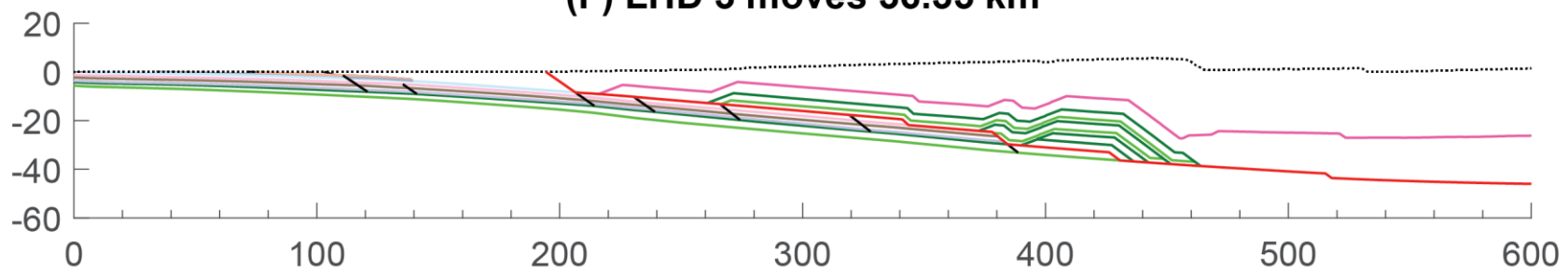
(D) LHD 1 moves 66.9 km



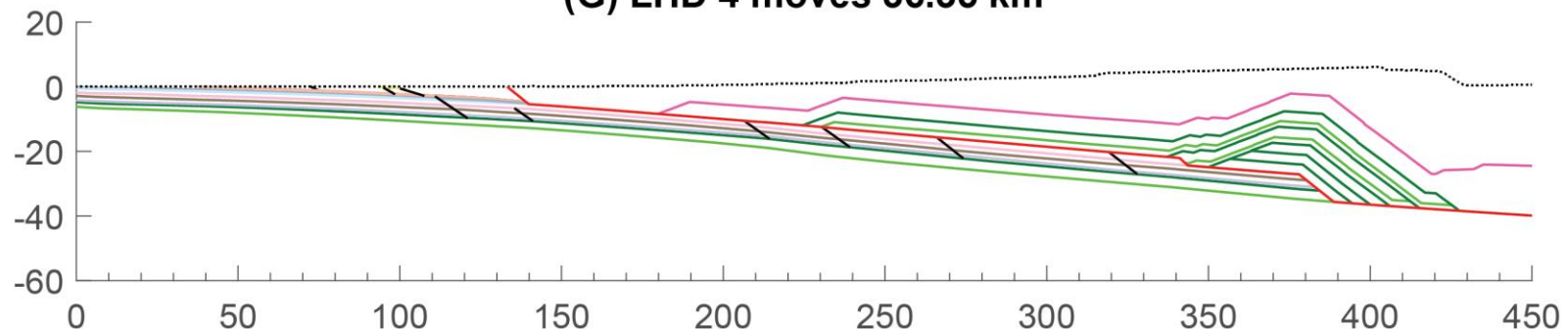
(E) LHD 2 moves 36.65 km



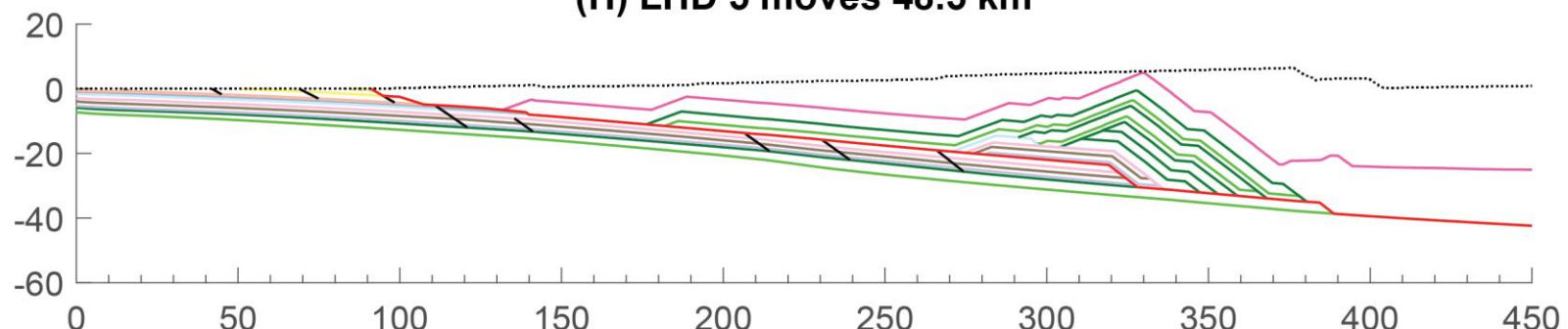
(F) LHD 3 moves 36.35 km



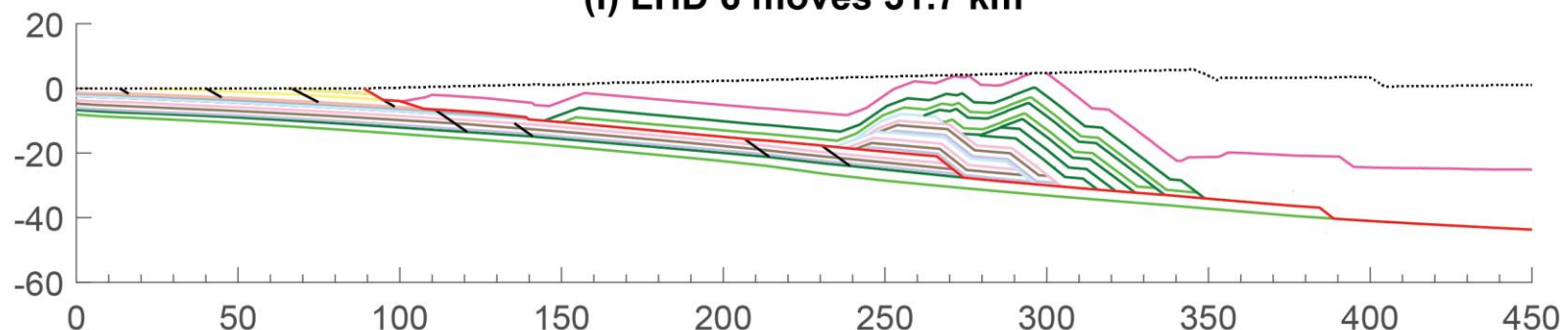
(G) LHD 4 moves 36.35 km



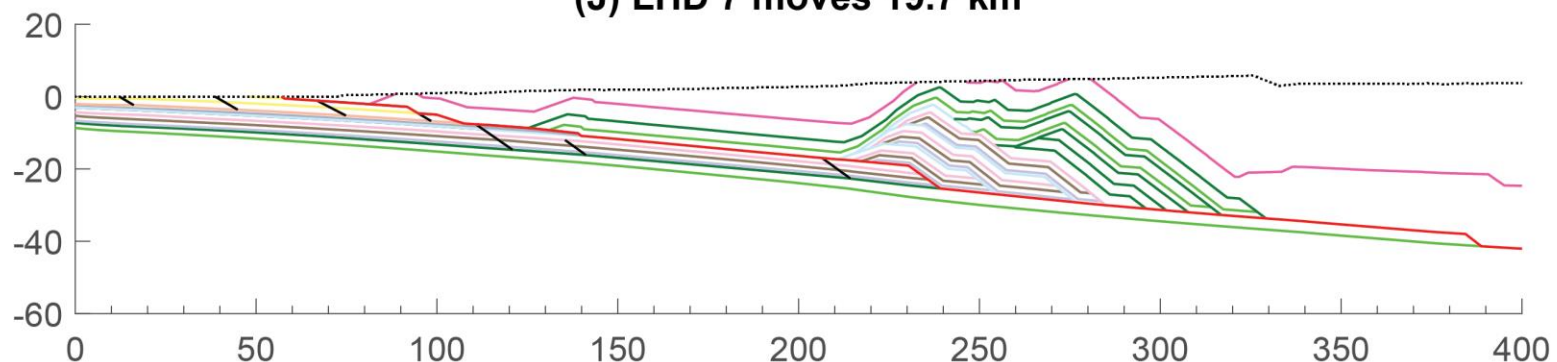
(H) LHD 5 moves 48.5 km



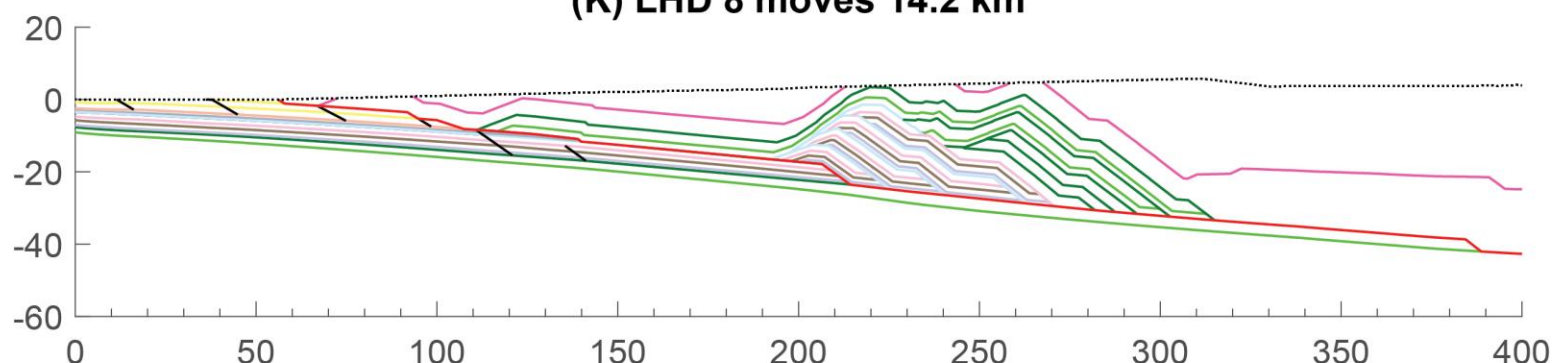
(I) LHD 6 moves 31.7 km



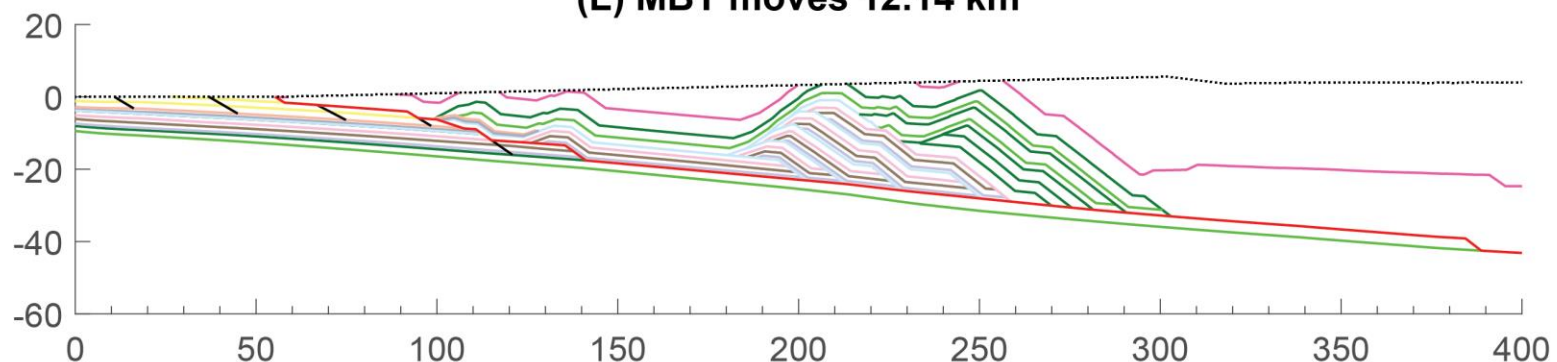
(J) LHD 7 moves 19.7 km



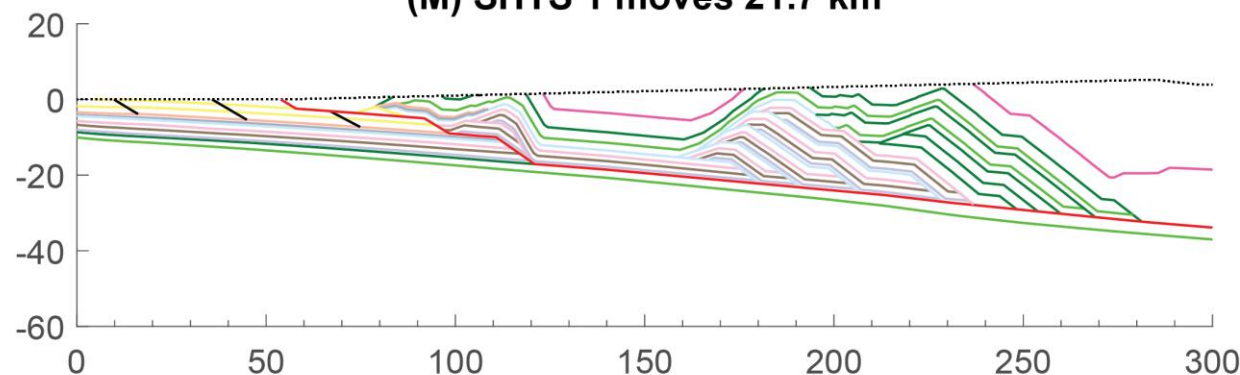
(K) LHD 8 moves 14.2 km



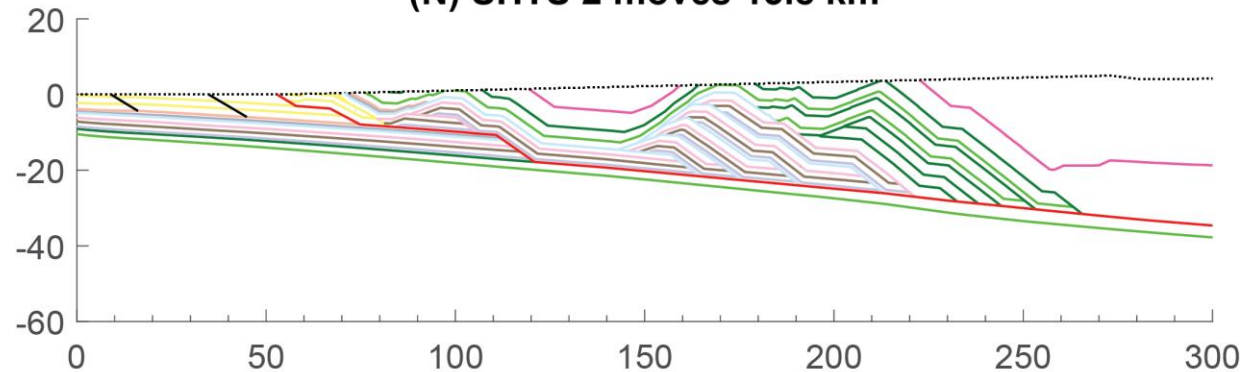
(L) MBT moves 12.14 km



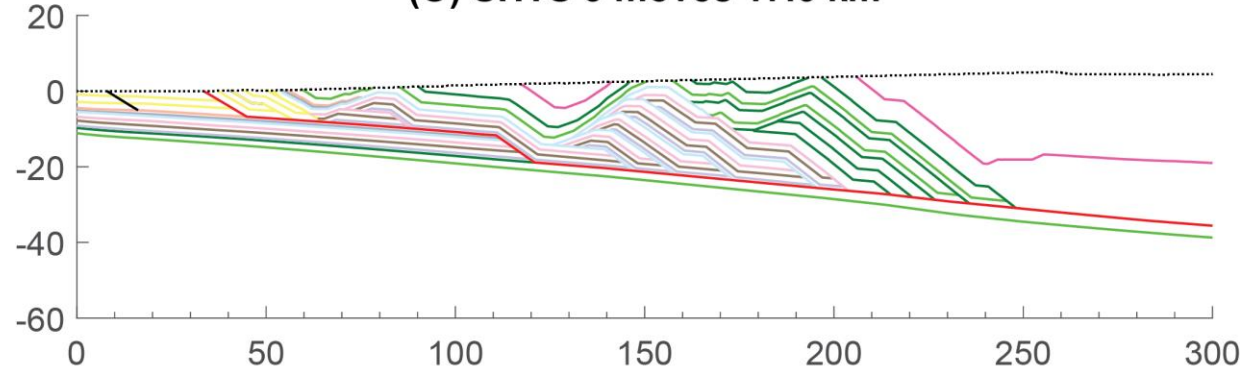
(M) SHTS 1 moves 21.7 km



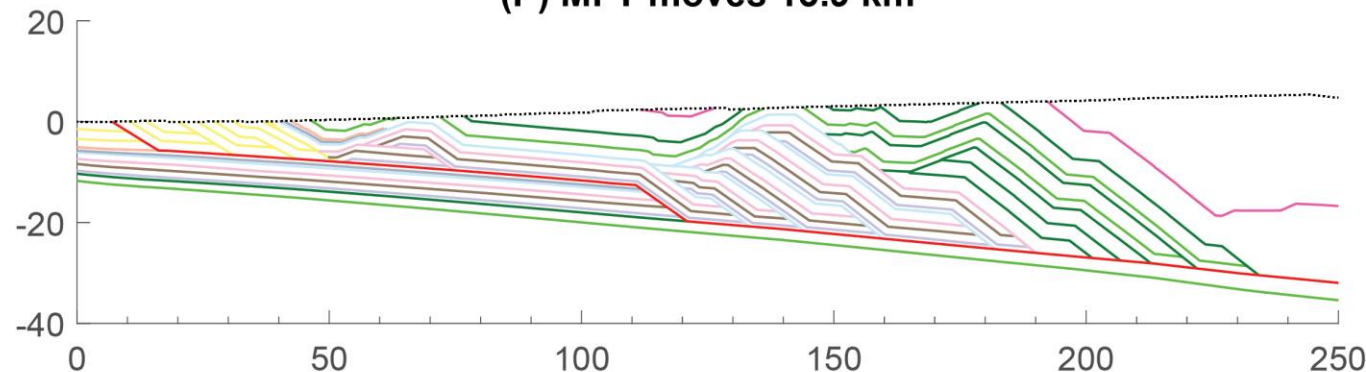
(N) SHTS 2 moves 15.8 km



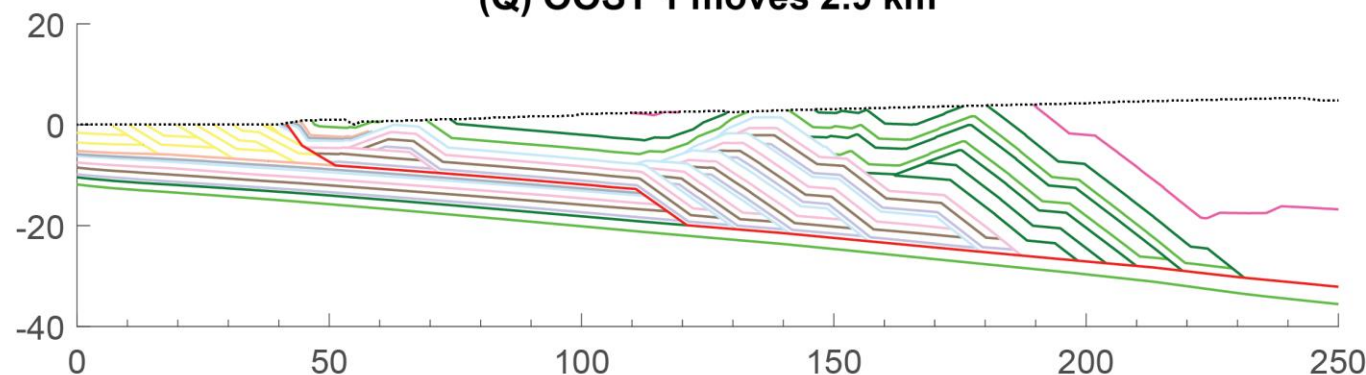
(O) SHTS 3 moves 17.6 km



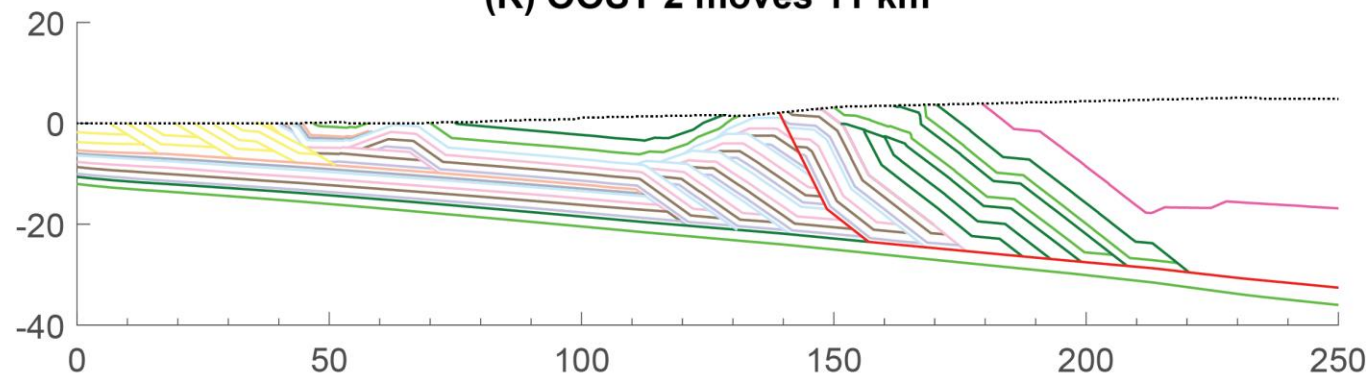
(P) MFT moves 13.9 km



(Q) OOST 1 moves 2.9 km



(R) OOST 2 moves 11 km



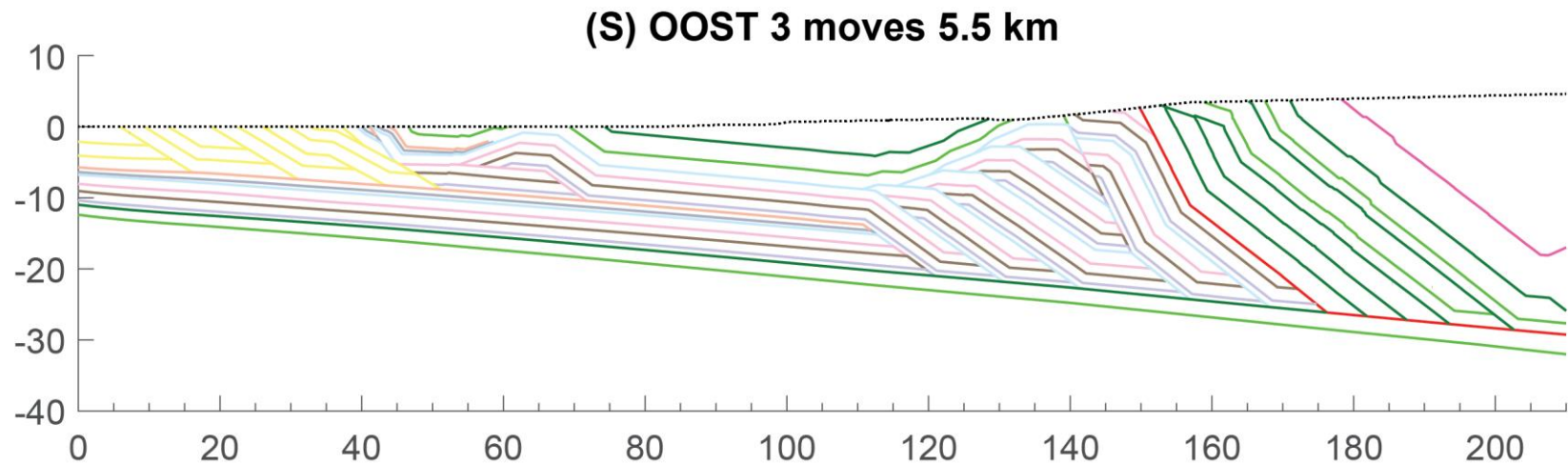


Figure 7: (A-S) Sequential flexural kinematic Robinson et al. (2006) cross section reconstructions. (A-C) has a vertical exaggeration of 1.5 and (D-S) has no vertical exaggeration. Active fault is red, dotted black line is the topographic surface, and solid black lines are inactive future fault ramp locations. Details of deformation are discussed in text and listed in Table 6. Individual stratigraphic units are identified by colored lines the line represents the top of unit and white area below line is the rock unit. GH rocks (dark pink), Kushma Formation (light green), Ranimata Formation (dark green), Sangram Formation (light purple), Galyang Formation (brown), Syangia Formation (light pink), Lakharpata Group (blue), Bhainskati Formation (dark purple), Dumri Formation (orange), and Siwaliks Group (yellow).

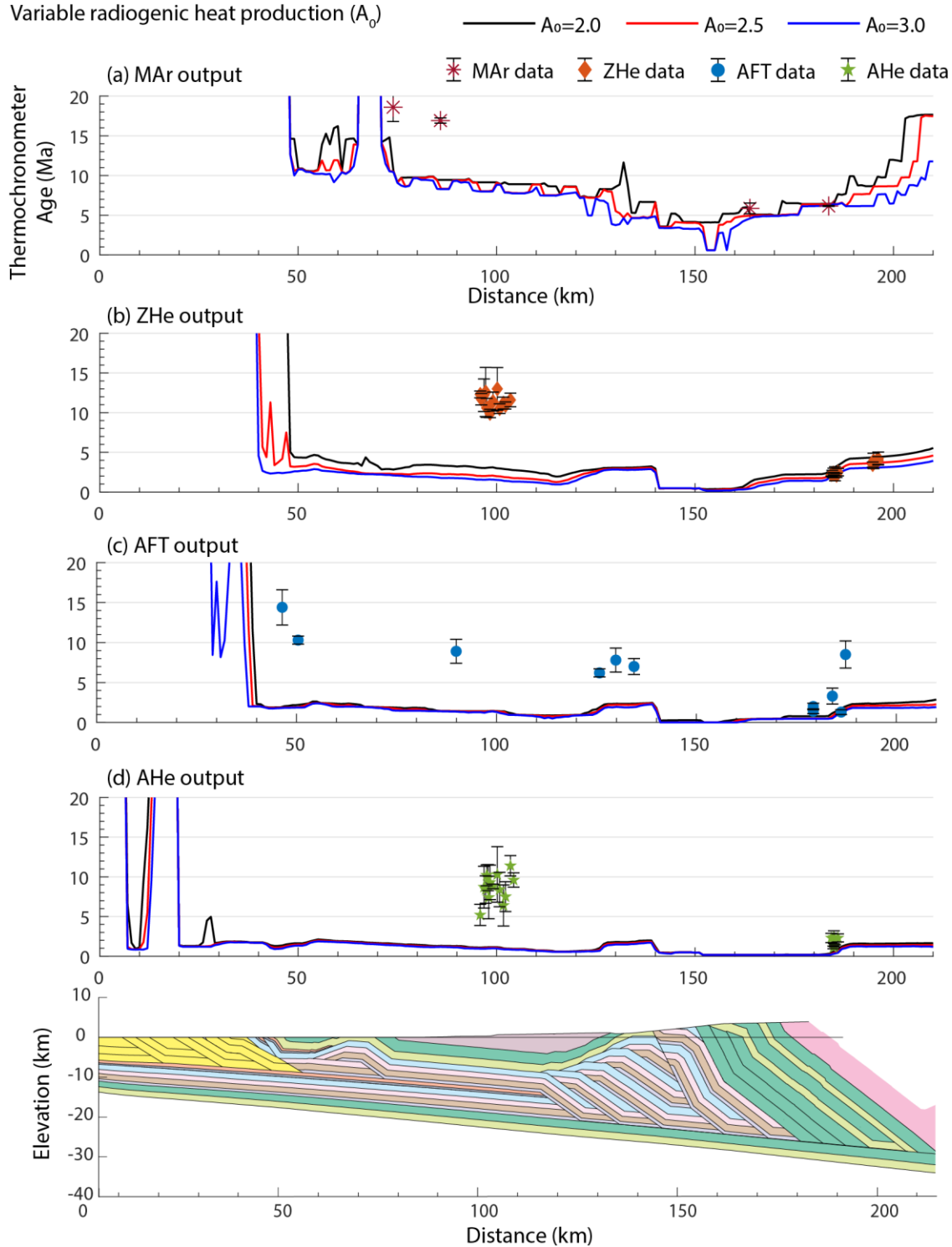


Figure 8: Predicted (A) MAr, (B) ZHe, (C) AFT, and (D) AFT cooling age outputs for Robinson et al. (2006) cross section Pecube models with variable radiogenic heat production values and a constant velocity rate. Predicted cooling ages are lines: black for A_0 of $2.0 \mu\text{W m}^{-3}$, red for A_0 of $2.5 \mu\text{W m}^{-3}$, and blue for A_0 of $3.0 \mu\text{W m}^{-3}$. Observed cooling ages are represented with symbols and 2σ error. MAr (red star), ZHe (orange diamond), AFT (blue circle), and AHe (green star).

4.1.2 Thermokinematic model

4.1.2.1 Effect of variable radiogenic heat production on predicted cooling ages

Figure 8 compares the published/observed cooling ages to the predicted cooling ages of MAr, ZHe, AFT, and AHe modeled with a constant velocity of 33.15 mm yr^{-1} for displacements on all faults and radiogenic heat production (A_0) values of 2.0, 2.5, and $3.0 \mu\text{W m}^{-3}$. The predicted cooling ages for all four thermochronometers are younger with higher A_0 (2.0 to $3.0 \mu\text{W m}^{-3}$) because the temperature throughout the crust is increased resulting in younger cooling ages. Changes in the A_0 value have the most influence on the MAr system with the average difference in predicted ages for A_0 of 2.0 and $3.0 \mu\text{W m}^{-3}$ being approximately 3 Ma (Fig. 8A). The active ramp is located between 110 and 120 km in this cross section. GH rocks north of the MCT that did not travel over the active ramp have predicted MAr ages that vary by approximately 8 Ma between A_0 values of 2.0 and $3.0 \mu\text{W m}^{-3}$. The MAr ages between $\sim 125 - 135 \text{ km}$ varies from $\sim 12 \text{ Ma}$ for an A_0 of $2.0 \mu\text{W m}^{-3}$ and $\sim 4 \text{ Ma}$ for an A_0 of $3.0 \mu\text{W m}^{-3}$. The predicted ZHe ages show the greatest variation in age south of the top of the active ramp at 110 km. South of the ramp, the predicted ZHe ages ranges from ~ 1 to 2 Ma for an A_0 value of $3.0 \mu\text{W m}^{-3}$ to ~ 2.5 to 4.5 Ma for an A_0 of $2.0 \mu\text{W m}^{-3}$ (Fig. 8B). Varying the radiogenic heat production had the least effect on the lowest-temperature thermochronometers of AFT and AHe. For both AFT and AHe, the resulting predicting cooling ages for each value of A_0 are practically identical, with the largest variations in the predicted cooling ages for the different radiogenic heat occurring between $\sim 110 - 140 \text{ km}$, which is the location of the active décollement ramp of the MHT and from north of the MCT where the rocks were not transported over the ramp (Figs. 8C & 8D). Predicted AFT and AHe ages are controlled by the movement over the active ramp of

the MHT between ~110 - 120 km. The predicted cooling age from ~40 – 110 km for AFT and AHe are young ages (~2 - >1 Ma) with the youngest ages at the active ramp.

The model cooling ages for all three radiogenic heat production values reproduce only 4 to 10 of the 57 observed cooling ages. In evaluating the fit between the observed and modeled cooling ages for all three different heat production values, an A_0 value of $2.0 \mu\text{W m}^{-3}$ is the best match; although, the predicted ages are still much younger than the observed ages for MAr, ZHe, AFT, and AHe thermochronometer ages. These underestimations of the predicted cooling ages with a constant rate of deformation indicate that a more complex and variable history of deformation and exhumation is required to better match the observed cooling age data or the cross section geometry itself is incorrect.

4.1.2.2 Effect of variable shortening rates on predicted cooling ages

Models with a constant deformation rate, predict cooling ages that underestimate the observed ages; thus, I vary the velocity rates to try and better match the observed cooling ages. I present five thermokinematic models, each with different and variable velocity rates and a radiogenic heat production value of $2.0 \mu\text{W m}^{-3}$. Table 5 lists all five variable velocity rates tested with the start and stop time and rate of deformation of each major fault system, Appendix C lists the start and stop time for each individual fault and the velocity rate of deformation. Velocity A, B, C, and D begins movement on the MCT at 25 Ma and ran to present day. Velocity E begins at 28 Ma. Figure 9 shows all five Pecube output for the variable velocity rates with the modeled cooling curves and observed cooling data plotted along the cross section. Table 7 lists the observed cooling ages and the modeled cooling ages for different velocity profiles tested,

highlighted cells are modeled cooling age values that match the observed cooling age within 2σ error.

Table 7: Observed cooling ages compared to modeled cooling ages for Robinson et al. (2006) Simikot cross section.

Thermo-chronometer system	Distance (km)	Cooling age (Ma)	Velocity A ages (Ma)	Velocity B ages (Ma)	Velocity C ages (Ma)	Velocity D ages (Ma)	Velocity E ages (Ma)
MAr	184	6.16 ± 0.06	6.53	10.97	12.35	12.83	15.59
	164	5.85 ± 0.67	5.85	10.62	11.37	11.67	14.53
	86	16.92 ± 0.33	7.44	13.74	14.45	15.35	17.90
	74	18.60 ± 1.80	8.44	14.82	15.24	16.29	18.76
ZHe	196	4.22 ± 0.81	4.97	8.72	10.37	10.77	13.50
	196	3.97 ± 0.50	4.97	8.72	10.37	10.77	13.50
	195	3.92 ± 0.97	4.96	8.67	10.35	10.74	13.47
	195	3.45 ± 0.32	4.96	8.67	10.35	10.74	13.47
	186	2.5 ± 0.47	4.31	7.21	9.47	9.76	12.51
	186	2.1 ± 0.26	4.31	7.21	9.47	9.76	12.51
	185	2.3 ± 0.88	4.07	6.68	9.15	9.44	12.17
	185	2.3 ± 0.15	4.07	6.68	9.15	9.44	12.17
	185	2.4 ± 0.6	4.07	6.68	9.15	9.44	12.17
	185	2.3 ± 0.42	4.07	6.68	9.15	9.44	12.17
	184	2.2 ± 0.18	3.81	6.02	8.75	8.98	11.69
	103	11.6 ± 0.86	4.06	5.17	8.27	8.29	10.44
	102	10.9 ± 0.45	4.11	5.24	8.33	8.35	10.51
	102	11.2 ± 0.75	4.11	5.24	8.33	8.35	10.51
	101	10.5 ± 0.61	4.18	5.38	8.50	8.53	10.75
	100	13 ± 2.68	4.21	5.43	8.55	8.58	10.81
	99	11.4 ± 1.2	4.29	5.65	8.70	8.76	11.01
	98	9.9 ± 0.52	4.28	5.55	8.64	8.68	10.90
	97	10.6 ± 1.2	4.26	5.39	8.53	8.55	10.73
	97	12.6 ± 3.1	4.26	5.39	8.53	8.55	10.73
	97	12.2 ± 2.05	4.26	5.39	8.53	8.55	10.73
	96	11.7 ± 0.73	4.28	5.41	8.54	8.56	10.72
	96	12.3 ± 0.43	4.28	5.41	8.54	8.56	10.72
AFT	187	8.5 ± 1.7	3.13	4.37	7.42	7.56	10.09
	186	1.3 ± 0.3	2.78	3.82	6.78	6.88	9.18
	184	3.3 ± 1	2.05	2.88	5.40	5.49	7.42
	179	2 ± 0.4	1.54	2.24	4.37	4.44	6.06
	179	1.4 ± 0.3	1.54	2.24	4.37	4.44	6.06
	134	7 ± 1	4.09	5.30	9.03	9.04	11.93

Thermo-chronometer system	Distance (km)	Cooling age (Ma)	Velocity A ages (Ma)	Velocity B ages (Ma)	Velocity C ages (Ma)	Velocity D ages (Ma)	Velocity E ages (Ma)
AFT (contd.)	130	7.8 ± 1.5	4.11	5.21	8.99	9.01	11.88
	126	6.2 ± 0.5	3.45	4.31	7.80	7.82	10.42
	90	8.9 ± 1.5	2.45	2.91	5.20	5.19	6.72
	50	10.3 ± 0.5	3.76	4.19	7.72	7.67	10.06
	46	14.4 ± 2.2	3.55	3.83	7.00	6.93	9.13
AHe	186	2.3 ± 0.51	1.52	2.04	3.77	3.80	5.02
	185	1.3 ± 0.13	1.20	1.61	3.04	3.06	4.04
	185	2.4 ± 0.8	1.20	1.61	3.04	3.06	4.04
	185	1.1 ± 0.16	1.20	1.61	3.04	3.06	4.04
	184	2.3 ± 0.58	0.69	0.96	1.91	1.92	2.54
	104	9.6 ± 0.9	1.64	1.85	3.38	3.37	4.41
	103	11.4 ± 1.28	1.70	1.92	3.50	3.49	4.57
	102	7.5 ± 1.88	1.77	2.00	3.61	3.61	4.70
	102	6.4 ± 2.59	1.77	2.00	3.61	3.61	4.70
	101	8.4 ± 2.17	1.82	2.05	3.74	3.74	4.86
	100	10.3 ± 3.5	1.86	2.09	3.80	3.79	4.93
	99	8.8 ± 0.29	1.89	2.12	3.82	3.82	4.96
	98	9.3 ± 2.17	1.89	2.13	3.83	3.83	4.98
	98	7.4 ± 2.68	1.89	2.13	3.83	3.83	4.98
	98	9.9 ± 1.65	1.89	2.13	3.83	3.83	4.98
	97	10.2 ± 1.32	1.88	2.11	3.82	3.81	4.95
	97	8.4 ± 1.73	1.88	2.11	3.82	3.81	4.95
	97	8.7 ± 2.63	1.88	2.11	3.82	3.81	4.95
	96	5.2 ± 1.33	1.89	2.13	3.86	3.85	5.02

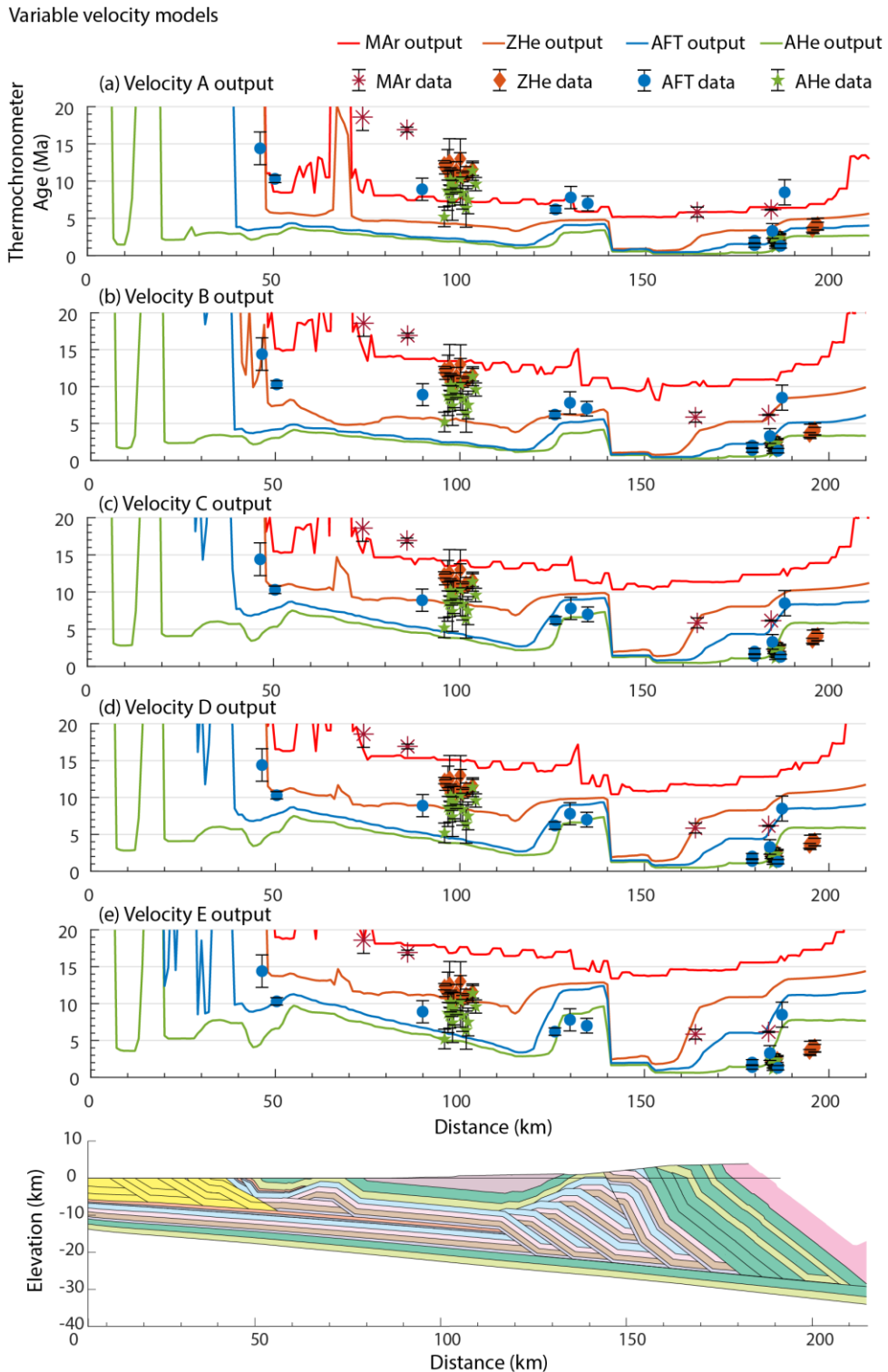


Figure 9: Predicted MAr (red line), ZHe (orange line), AFT (blue line), and AHe (green line) cooling age outputs for Robinson et al. (2006) cross section Pecube models with variable velocity models, summarized in Table 5. (A) Velocity A, (B) Velocity B, (C) Velocity C, (D) Velocity D, and (E) Velocity E all with $A_0 = 2.0 \mu\text{W m}^{-3}$.

In Velocity A, the MCT moved from 25 to 13 Ma, the RMT moved from 13 to 9 Ma, the LHD formed from 9 to 5 Ma, and the SHTS and OOST faults moved from 5 to 0 Ma (Table 5). Predicted cooling ages match 5 out of 57 existing observed cooling ages (Fig. 9A & Table 7). All five predicted ages that match are in the north between 160 and 200 km. These predicted ages are not reset by traveling over the active MHT ramp between 110 and 120 km. The predicted MAr ages in the DK are ~10 Ma younger than the observed ages. Modeled ZHe cooling ages are too young in the DK (~75 – 130 km) with modeled ages ~4 Ma and observed ages between ~9 – 13 Ma. ZHe modeled ages are too old north of the MCT in the GH with modeled cooling ages of ~4 – 5 Ma compared to the observed ~2 – 4 Ma ages. Velocity A reproduces 1 of the 11 AFT and 2 of the 19 AHe ages north of the MCT that did not travel over the active ramp. All AFT and AHe predicted ages south of the active ramp are reset by moving over the ramp, and the predicted cooling ages are much younger than the observed ages south of the ramp.

Velocity B was based on foreland basin data compiled in Robinson and McQuarrie (2012). In the flexural kinematic model, the cross section is sequentially deformed in the hinterland where units are exposed, eroded, and deposited into the foreland basin. Deposition ages of synorogenic units and the appearance of hinterland derived clasts in the Siwalik Group brackets the deformation timing of faults (Robinson and McQuarrie, 2012). In this model, the MCT moves from 25 – 20 Ma, the RMT moves from 20 – 16 Ma, the LHD forms from 16 – 5 Ma, and the SHTS and OOST faults move from 5 – 0 Ma (Table 5). Predicted cooling ages match 4 out of 57 existing observed cooling ages (Fig. 9B & Table 7). The model overestimates the ages of MAr in the LHD and GH rocks just north of the MCT with predicted ages ~11 Ma, which is >5 Ma older than the observed ages. Modeled MAr ages are too young in the DK and just south of it between ~75 – 130 km with modeled ages between 13 – 14 Ma, which is <4 Ma

younger than the observed ages. Modeled MAr ages pass through the closure temperature window during formation and movement on the RMT. Modeled ZHe cooling ages are too young in the DK with modeled ages \sim 5 – 6 Ma and observed ages between \sim 9 – 13 Ma. ZHe modeled ages are too old north of the MCT in the GH with modeled cooling ages of \sim 6 – 8 Ma compared to the observed \sim 2 – 4 Ma ages. Velocity B reproduces 2 of the 11 AFT and 2 of the 19 AHe ages. The modeled AFT and AHe ages that match are north of the MCT and did not travel over the active ramp; therefore, the model only reproduces AFT and AHe ages that are not reset by moving over the ramp. All AFT and AHe predicted ages south of the active ramp are too young.

Velocity C attempts to increase the age of the predicted cooling ages in the DK. To produce old MAr ages in the DK, movement on the MCT and RMT needs to start early and end early because these are the faults that carry the rock in the DK and the cooling ages in the DK are set during movement on the MCT and RMT. In this model, the MCT moves from 25 – 20 Ma, the RMT and LHD thrust sheets move from 20 – 10 Ma, and the SHTS and OOST faults move from 10 – 0 Ma. Predicted cooling ages match 4 out of 57 published cooling ages, with 2 AFT and 2 AHe predicted ages matching the observed ages north of the MCT in GH that did not travel over the active ramp (Fig. 9C & Table 7). This velocity model shifted the pattern of predicted ages upward producing older ages across the entire section, particularly for the ZHe, AFT, and AHe thermochronometers systems (Fig. 9C).

With Velocity D, the shortening rate of the MCT is increased to produce older predicted cooling ages in the DK. The MCT moves from 25 – 22 Ma, the RMT and LHD thrust sheets move from 22 – 10 Ma, and the SHTS and OOST faults moves from 10 – 0 Ma. The shortening rate on the MCT is 84 mm yr^{-1} , which is an unrealistically high rate; however, it is tested to determine the result it would have on the predicted cooling ages. Predicted cooling ages matched

4 out of 57 published cooling ages, with 2 AFT and 2 AHe predicted ages matching the observed ages north of the MCT in GH that did not travel over the active ramp (Fig. 9D & Table 7).

Despite the higher shortening rate for the MCT, the resulting modeled ages fit the observed ages in the same way that Velocity C did. This is because the ZHe, AFT, and AHe ages all become reset as they travel over the active ramp from 17 to 10 Ma. Velocity D produces slightly older predicted cooling ages for ZHe, AFT, and AHe than previous models (Fig. 9).

Velocity E begins movement on the MCT at 28 Ma, which is 3 Ma earlier than $^{40}\text{Ar}/^{39}\text{Ar}$ data suggests that movement began on the MCT (DeCelles et al., 2001; Robinson et al., 2006) to allow the MCT and RMT to deform early to produce the older cooling ages in the DK, without having unrealistically high shortening rates. The MCT moves from 28 – 24 Ma, the RMT and LHD thrust sheets move from 24 – 13 Ma, and the SHTS and OOST faults moves from 13 – 0 Ma. Velocity model E reproduces the most cooling ages of all the variable velocities tested for the Robinson et al. (2006) cross section with the predicted cooling ages matching 15 of the 57 published cooling ages (Fig. 9E & Table 7). This model reproduces 1 of 4 MAr ages south of the DK, and has a close age prediction for the MAr age in the DK; however, the ages are too old north of the DK by >8 Ma. Modeled ZHe ages reproduces 8 of the 23 observed ages, all in the DK. To the north of the DK, modeled ZHe ages are 12-13 Ma, and the observed ages are only between 2 – 4 Ma. This model reproduces 2 of the 11 AFT ages, and the modeled ages in the DK are older than the observed ages. This model reproduces 4 of the 19 AHe ages with 3 of them in the DK and one north of the MCT. Although the timing of deformation in Velocity E results in a better fit of the modeled ages to the observed data compared to Velocity A through D, there is still a large discrepancy between the modeled and observed ages (Fig. 9). This discrepancy between modeled and observed cooling ages for all velocity models tested indicates the cross

section geometry is unable to reproduce the cooling ages along the cross section and therefore must be incorrect.

4.2 Modified version of Simikot cross section from Olsen et al. (2018)

4.2.1 Flexural-kinematic model

Table 8 lists the minimum shortening estimates of the modified Olsen et al. (2018) version of the Simikot cross section based on the regional cross section and the shortening amounts determined from the flexural-kinematic modeling of this section (Fig. 10). The minimum initial length of the undeformed Indian passive margin from the future location of the MFT to the northernmost extent of the GH rocks is 1180.40 km. The total shortening determined by the flexural-kinematic model is 874.89 km. The final length of the cross section from the MFT to the northernmost extent of the GH is 305.51 km. Therefore, total shortening is ~74% of the original length of the undeformed cross section.

Table 8: Simikot cross section Olsen et al. (2018) flexural-kinematic model displacement.

Fault	Step	Displacement		Cumulative Displacement (km)
		(km)		
	A	0		0
MCT	B	220.5		220.5
RMT	C	205.65		426.15
LHD 1	D	56.95		483.1
LHD 2	E	51.6		534.7
LHD 3	F	48.48		583.18
LHD 4	G	9.24		592.42
LHD 5	H	52.2		644.62
LHD 6	I	39.82		684.44
LHD 7A	J	10		694.44
LHD 7B	K	27.7		722.14
LHD 8	L	37.65		759.79
LHD 9	M	31.8		791.59
MBT	N	13.95		805.54
SHTS 1	O	5		810.54
SHTS 2	P	19.55		830.09
SHTS 3A	Q	8		838.09
OOST 1	R	12.1		850.19
OOST 2	R	2.8		852.99
SHTS 3B	S	7.7		860.69
MFT	T	14.2		874.89

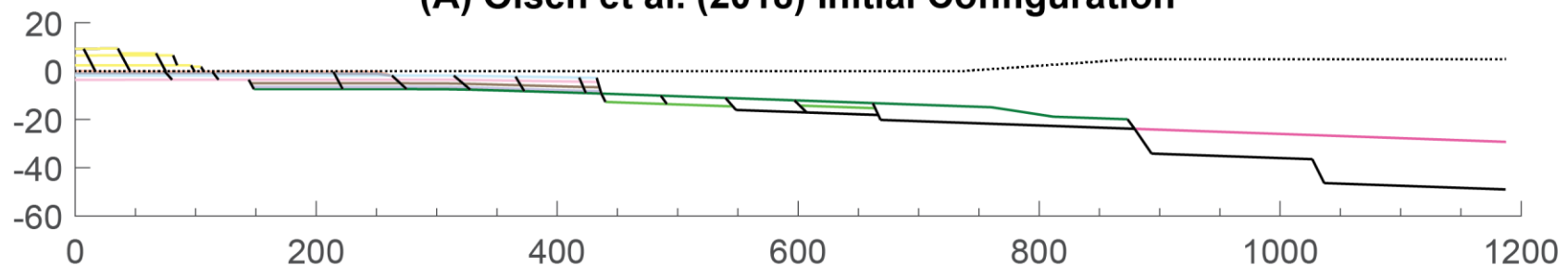
Just as with the Robinson et al. (2006) cross section, the modified section displacements along each fault were adjusted to best match the geometry of the final modeled cross section to the original balanced cross section. The displacement along this section are divided into five major fault systems consisting of multiple individual thrust sheets: MCT, RMT, LHD, SHTS, and OOST faulting. The sequence of faulting for this cross section is different than the sequence for the Robinson et al. (2006) Simikot cross section. The Olsen et al. (2018) cross section has one more LHD thrust fault and one less OOST with the two OOST faulting occurring in between

movement of SHTS 3A and SHTS 3B rather than at the end like it does in Robinson et al. (2006).

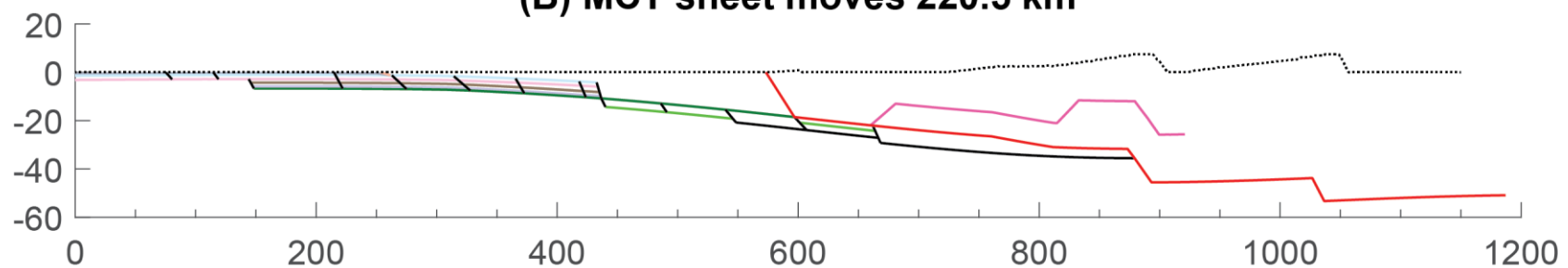
Figure 10A shows the initial configuration of the model. The MCT accounts for 25% of the total minimum shortening (Fig. 10B). The RMT accommodates 24% of the total shortening (Fig. 10C). The ten faults of the LHD, including the MBT accommodate 43% of the total shortening (Fig. 10D-N). Four thrust sheets of the SHTS including the MFT account for 6% of the total shortening (Fig. 10O-Q and Fig. 10S-T). The two OOST faults accommodate 2% of the total shortening (Fig. 10R). GH rocks are exposed after 513.1 km of shortening during movement on the LHD 1. LH rocks are exposed after 722.14 km of shortening during movement of LHD 7B.

The bulk density, sediment density, EET, and topographic angle varies systematically to find a flexural-kinematic model to best match the surface geology, dip of the décollement, and depth of foreland basin. Table 3 summarizes the 4 flexural-kinematic models with the various parameters tested with the final best fit model highlighted. The parameters for the best fit model are a bulk density of 2600 kg m^{-3} , a sediment density of 2350 kg m^{-3} , an EET of 95 km, and a topographic erosion angle of 1.75° . This resulted in a foreland basin depth measured from the MFT of 7.9 km compared to 9.4 km on the original section, and a décollement dip of 4.5° compared to 4.0° on the original section.

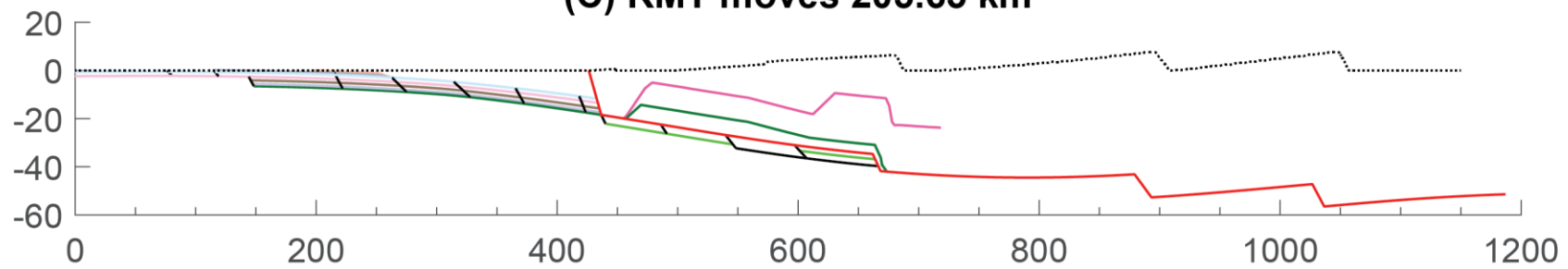
(A) Olsen et al. (2018) Initial Configuration



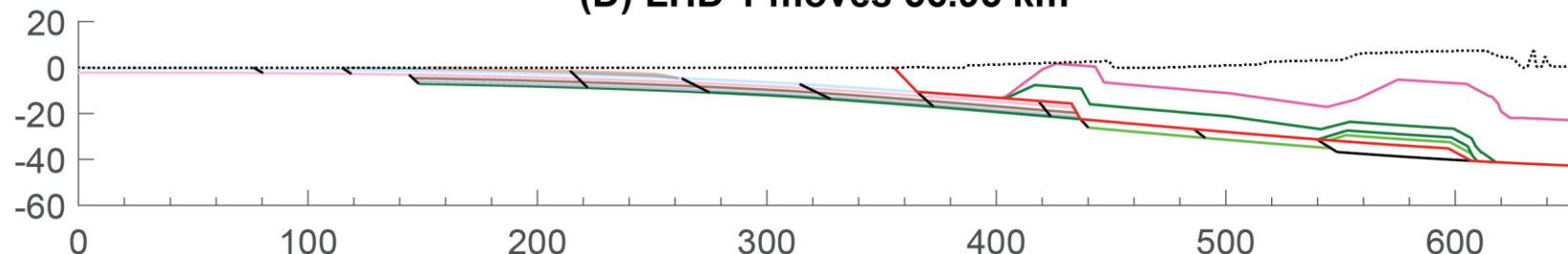
(B) MCT sheet moves 220.5 km



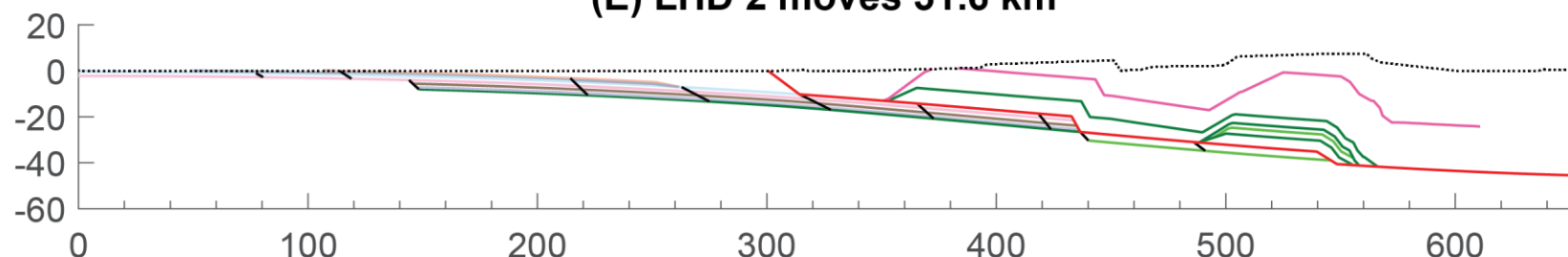
(C) RMT moves 205.65 km



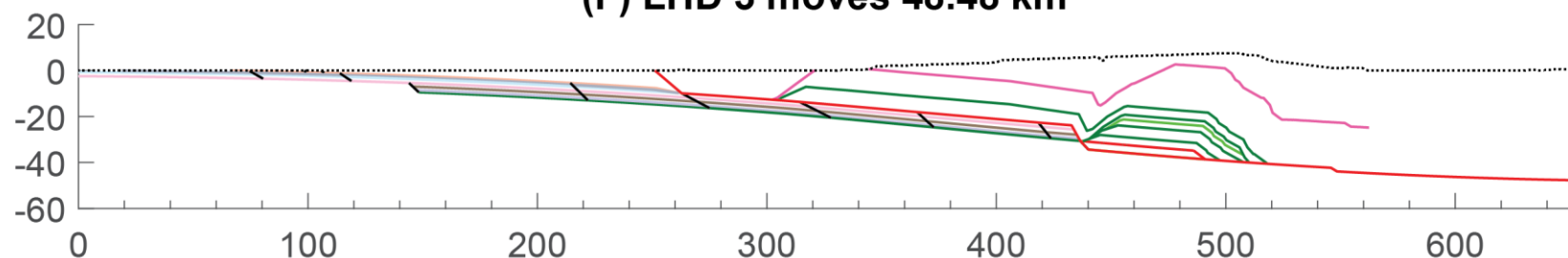
(D) LHD 1 moves 56.95 km



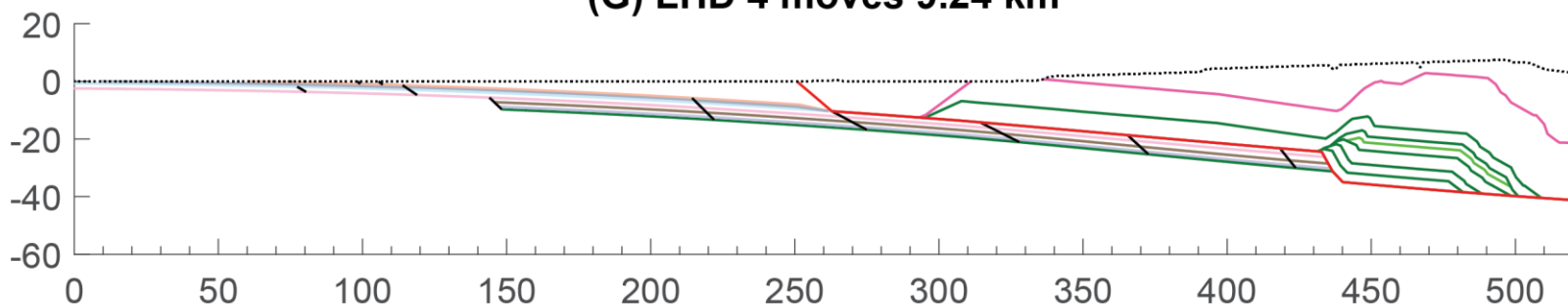
(E) LHD 2 moves 51.6 km



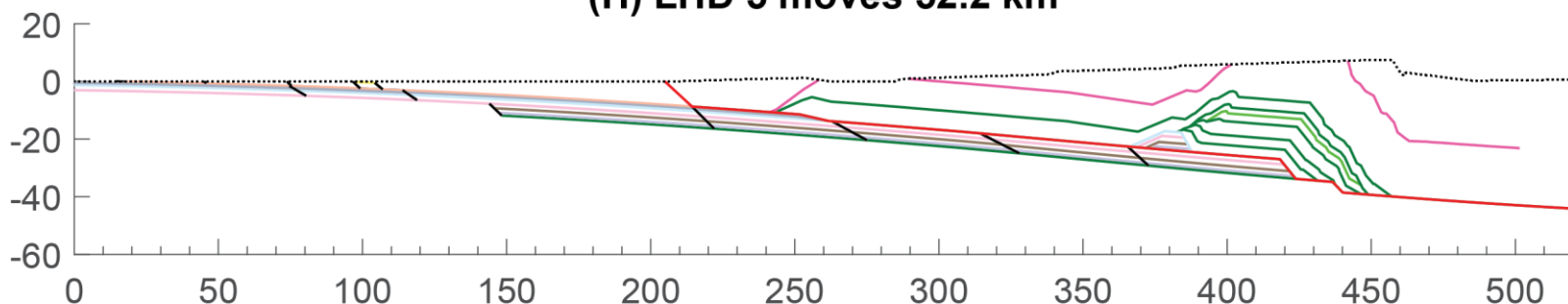
(F) LHD 3 moves 48.48 km



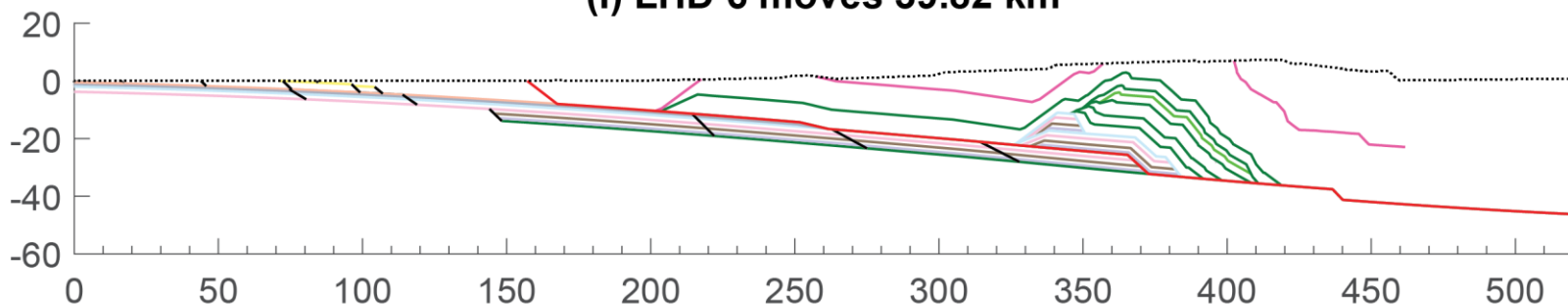
(G) LHD 4 moves 9.24 km



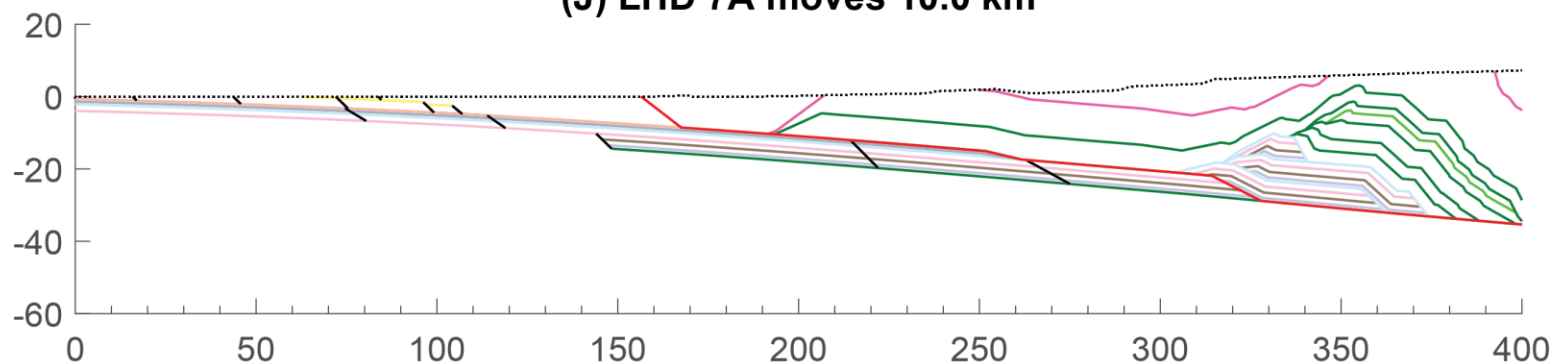
(H) LHD 5 moves 52.2 km



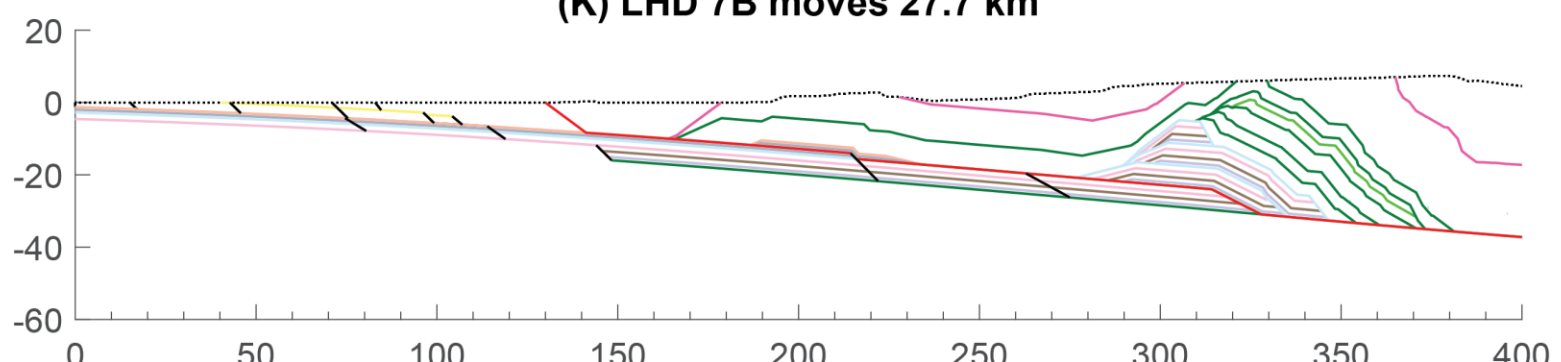
(I) LHD 6 moves 39.82 km



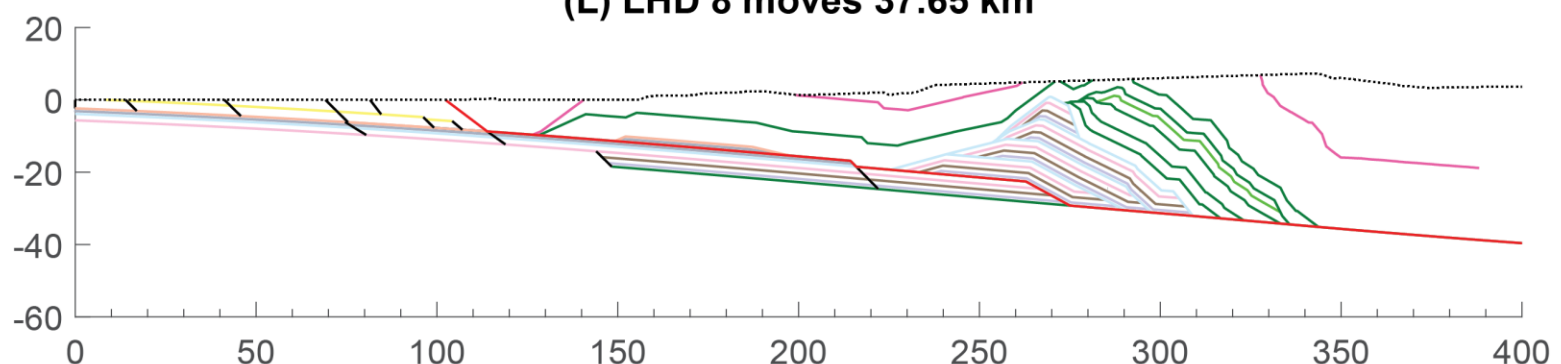
(J) LHD 7A moves 10.0 km



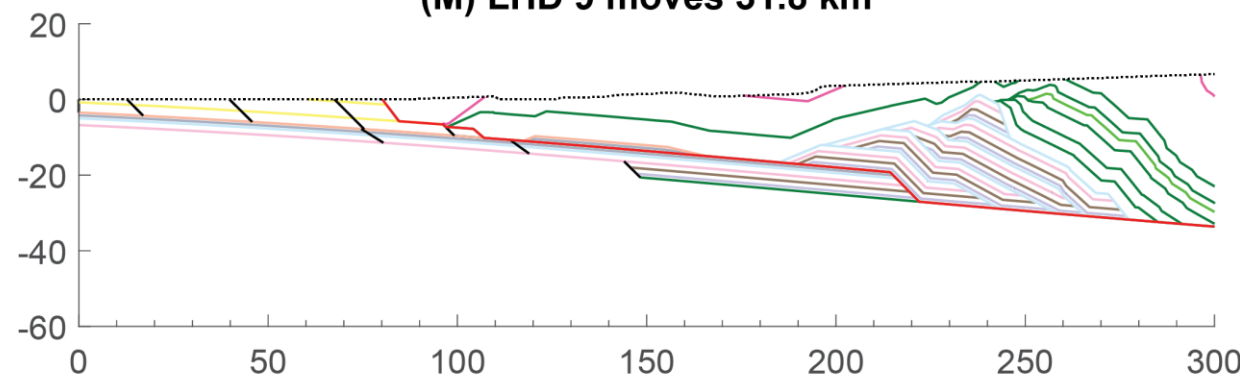
(K) LHD 7B moves 27.7 km



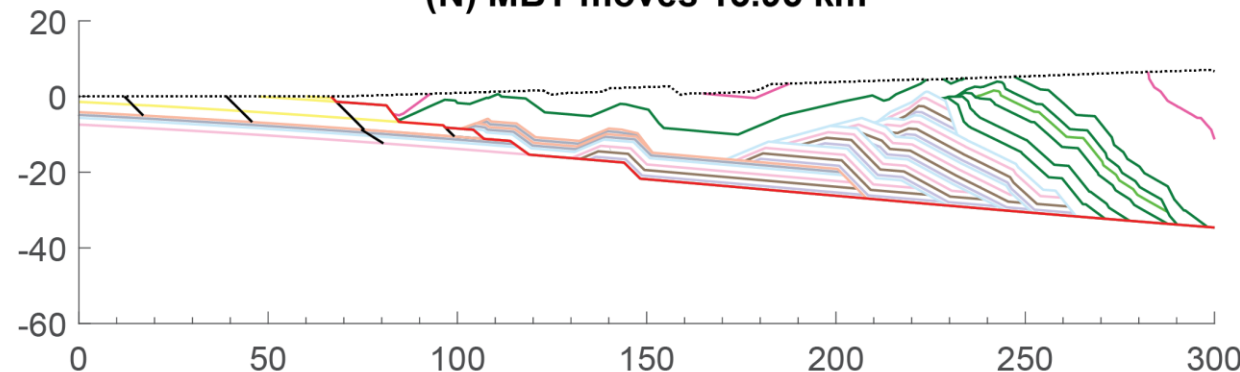
(L) LHD 8 moves 37.65 km



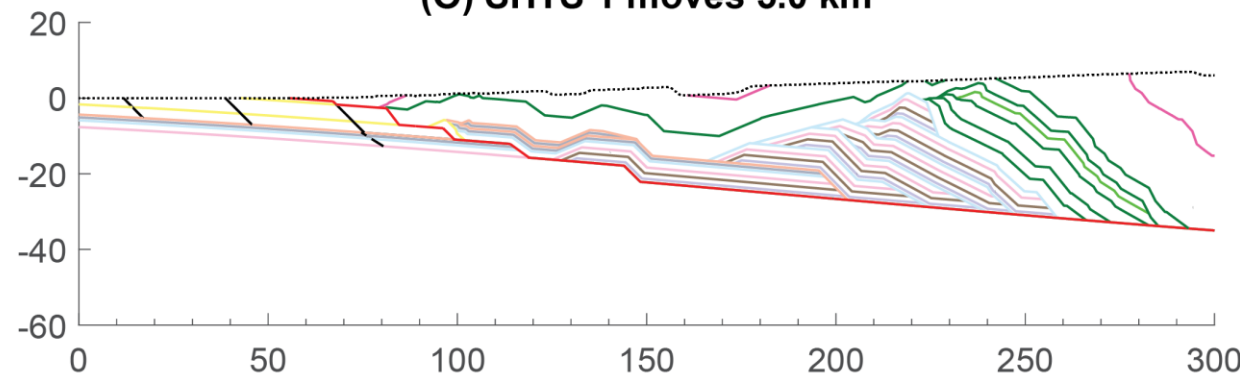
(M) LHD 9 moves 31.8 km

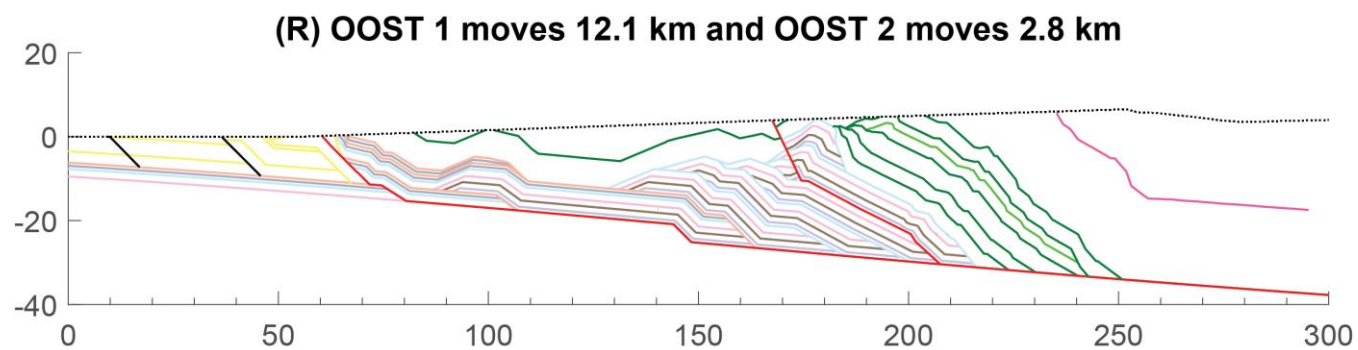
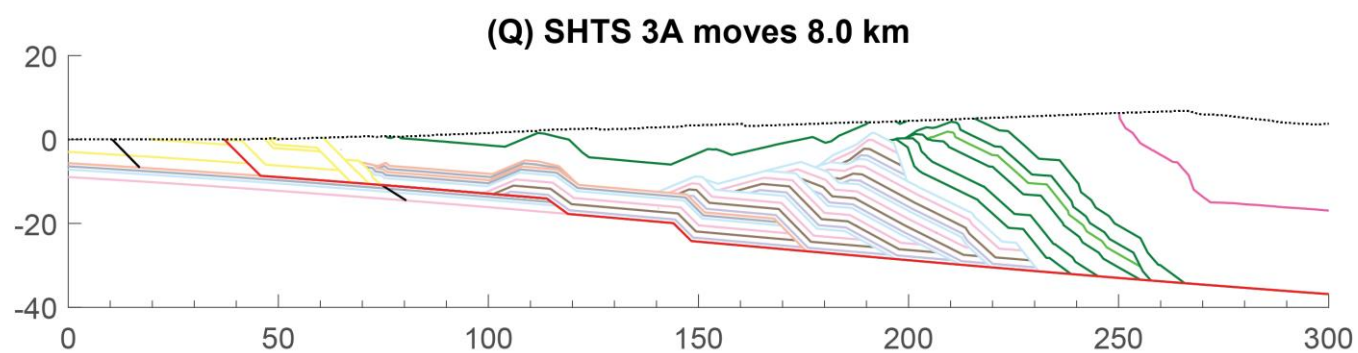
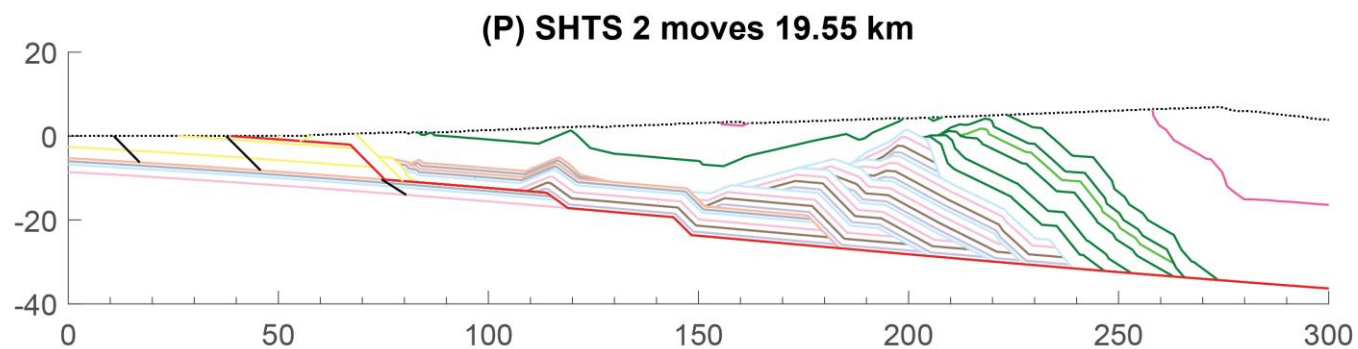


(N) MBT moves 13.95 km



(O) SHTS 1 moves 5.0 km





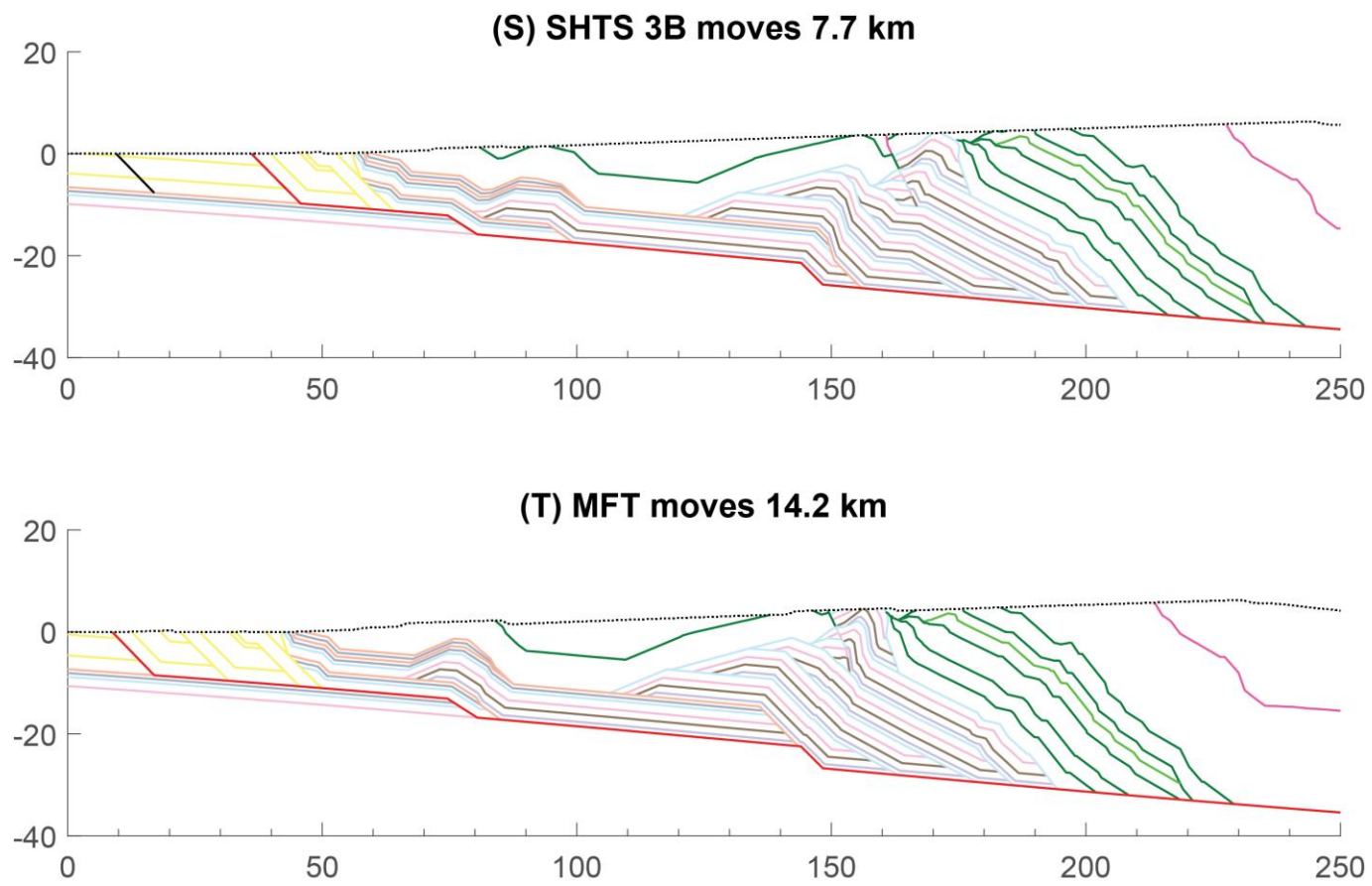


Figure 10: (A-T) Sequential flexural kinematic Olsen et al. (2018) cross section reconstructions. (A-C) has a vertical exaggeration of 1.5 and (D-T) has no vertical exaggeration. Active fault is red, dotted black line is the topographic surface, and solid black lines are inactive future fault ramp locations. Details of deformation are discussed in text and listed in Table 8. Individual stratigraphic units are identified by colored lines the line represents the top of unit and white area below line is the rock unit. Rock unit colors are the same as in Figure 7.

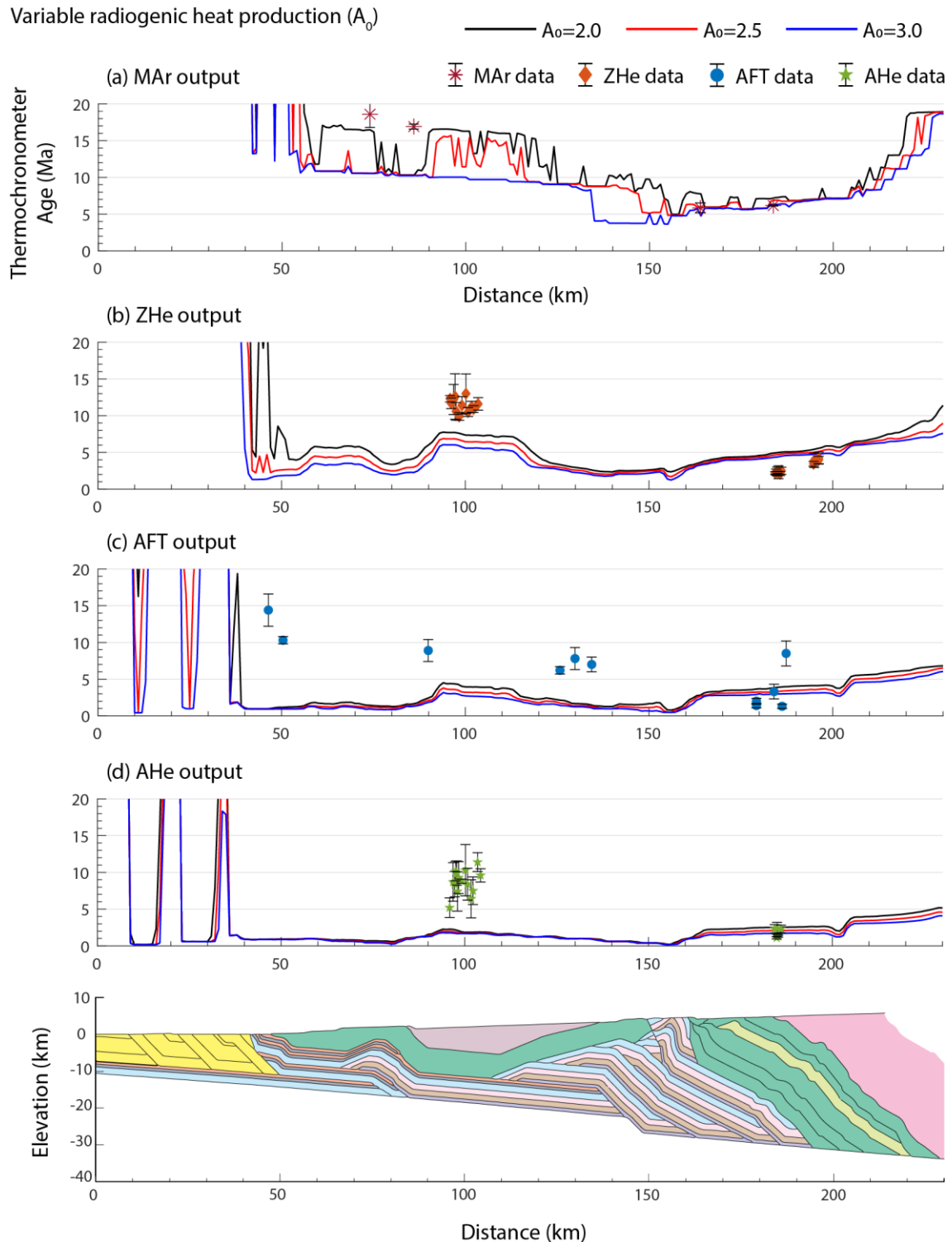


Figure 11: Predicted (A) MAr, (B) ZHe, (C) AFT, and (D) AFT cooling age outputs for Olsen et al. (2018) cross section Pecube models with variable radiogenic heat production values. Symbols same as in Figure 8.

4.2.2 Thermokinematic model

4.2.2.1 Effect of variable radiogenic heat production on predicted cooling ages

Three radiogenic heat production values are tested in the Pecube models for the Olsen et al. (2018) section using a constant shortening rate of 35.00 mm yr⁻¹ from 25 Ma to present. Radiogenic heat production (A_0) values tested are 2.0, 2.5, and 3.0 $\mu\text{W m}^{-3}$. Figure 11 compares the predicted cooling ages of MAr, ZHe, AFT, and AHe to the published data.

Similar to the Robinson et al. (2006) models, the predicted cooling ages for all four thermochronometers systems become younger as A_0 increases from 2.0 to 3.0 $\mu\text{W m}^{-3}$ in the Olsen et al. (2018) models. Variable A_0 values have the largest effect on the predicted MAr ages with the difference in predicted ages ranging as much as ~7 Ma in the DK. Observed MAr ages north of the northern ramp are ~6 Ma with the predicted cooling ages matching for A_0 values of 2.5 and 3.0 $\mu\text{W m}^{-3}$ and predicted ages for 2.0 $\mu\text{W m}^{-3}$ within 1 Ma of the observed ages (Fig. 11A). ZHe predicted ages vary from different A_0 values with the largest south of the northern ramp with a difference of ~3 Ma between an A_0 of 2.0 and 3.0 $\mu\text{W m}^{-3}$. North of the northern ramp, the predicted ZHe ages are fairly similar with the difference in predicted ages ~0.5 Ma between A_0 of 2.0 and 3.0 $\mu\text{W m}^{-3}$ (Fig. 11B). AFT predicted ages within the DK range ~1.5 Ma between A_0 of 2.0 and 3.0 $\mu\text{W m}^{-3}$. North of the northern ramp, the AFT predicted ages range ~1 Ma between A_0 of 2.0 and 3.0 $\mu\text{W m}^{-3}$. AFT is the only thermochronometer system with observed data south of the southern ramp of the décollement with ages of ~10 Ma and ~14.5 Ma (Fig. 11C). All three heat production values underpredicted the cooling ages south of this ramp with predicted cooling ages of ~1 Ma. The predicted cooling ages for AHe varied very little with different A_0 values with the greatest difference in predicted ages for different A_0 values being north of the northern ramp; however, the predicted ages only varied by >1 Ma (Fig. 11D).

All three values of radiogenic heat productions predict cooling ages significantly younger than the observed thermochronology data in the DK between 75 – 128 km, where all the predicted ages for the different thermochronometers systems are significantly younger than the observed data. The predicted cooling ages north of the northern ramp are close to the observed cooling ages for MAr and AHe; however, all A_0 values overpredict cooling ages for ZHe and AFT in the same location. The cooling age models for A_0 values of 2.0 and 3.0 $\mu\text{W m}^{-3}$ reproduces 4 of the 57 cooling ages and the A_0 value of 2.5 $\mu\text{W m}^{-3}$ reproduces 5 of the 57 cooling ages. All three values for radiogenic heat production produced poorly fitting modeled ages; therefore, best-fit for A_0 value is 2.0 $\mu\text{W m}^{-3}$ because it produces a cool crust and the oldest predicted cooling ages in the DK of all the A_0 values. The poor fit of modeled cooling ages to observed cooling ages indicates that a constant rate of shortening cannot reproduce the cooling ages along this cross section.

4.2.2.2 Effect of variable shortening rates on predicted cooling ages

To better match the predicted cooling ages to the observed ages, four different fault velocity rates were used to create thermokinematic models (Table 5). All variable velocity models use a radiogenic heat production value of 2.0 $\mu\text{W m}^{-3}$ with the MCT initiating at 25 Ma. Figure 12 shows the four Pecube outputs for the variable velocity rates with the modeled cooling curves and the observed thermochronometers ages. Table 9 lists the observed cooling ages and the modeled cooling ages for different velocity profiles with the highlighted cells where the modeled cooling age values that match the observed cooling age within 2σ error.

Table 9: Observed cooling ages compared to modeled cooling ages for Olsen et al. (2018) Simikot cross section.

Thermo-chronometer system	Distance (km)	Cooling age (Ma)	Velocity F ages (Ma)	Velocity G ages (Ma)	Velocity H ages (Ma)	Velocity I ages (Ma)
MAr	184	6.16 ± 0.06	6.55	10.34	12.75	12.05
	164	5.85 ± 0.67	5.88	10.76	11.44	11.14
	86	16.92 ± 0.33	8.04	13.59	14.87	13.89
	74	18.60 ± 1.80	8.15	18.22	15.04	14.03
ZHe	196	4.22 ± 0.81	5.65	8.76	11.36	10.92
	196	3.97 ± 0.50	5.65	8.76	11.36	10.92
	195	3.92 ± 0.97	5.64	8.64	11.34	10.91
	195	3.45 ± 0.32	5.64	8.64	11.34	10.91
	186	2.5 ± 0.47	5.50	8.20	11.18	10.74
	186	2.1 ± 0.26	5.50	8.20	11.18	10.74
	185	2.3 ± 0.88	5.48	8.13	11.11	10.70
	185	2.3 ± 0.15	5.48	8.13	11.11	10.70
	185	2.4 ± 0.6	5.48	8.13	11.11	10.70
	185	2.3 ± 0.42	5.48	8.13	11.11	10.70
	184	2.2 ± 0.18	5.47	8.05	11.07	10.66
	103	11.6 ± 0.86	6.24	10.43	12.47	11.73
	102	10.9 ± 0.45	6.24	10.42	12.46	11.73
	102	11.2 ± 0.75	6.24	10.42	12.46	11.73
	101	10.5 ± 0.61	6.24	10.43	12.47	11.73
	100	13 ± 2.68	6.25	10.45	12.48	11.74
	99	11.4 ± 1.2	6.31	10.59	12.57	11.82
	98	9.9 ± 0.52	6.37	10.72	12.65	11.89
	97	10.6 ± 1.2	6.40	10.79	12.71	11.93
	97	12.6 ± 3.1	6.40	10.79	12.71	11.93
	97	12.2 ± 2.05	6.40	10.79	12.71	11.93
AFT	187	8.5 ± 1.7	4.94	7.12	10.74	10.42
	186	1.3 ± 0.3	4.94	7.07	10.72	10.41
	184	3.3 ± 1	4.94	7.02	10.68	10.41
	179	2 ± 0.4	4.93	6.72	10.59	10.39
	179	1.4 ± 0.3	4.93	6.72	10.59	10.39

Thermo-chronometer system	Distance (km)	Cooling age (Ma)	Velocity F ages (Ma)	Velocity G ages (Ma)	Velocity H ages (Ma)	Velocity I ages (Ma)
AFT (contd.)	134	7 ± 1	3.59	3.83	8.01	8.00
	130	7.8 ± 1.5	3.85	4.11	8.40	8.37
	126	6.2 ± 0.5	4.16	4.56	9.08	8.96
	90	8.9 ± 1.5	4.61	4.87	9.36	9.34
	50	10.3 ± 0.5	2.56	2.38	4.41	4.42
	46	14.4 ± 2.2	2.30	2.19	4.21	4.22
AHe	186	2.3 ± 0.51	3.93	5.11	8.78	8.52
	185	1.3 ± 0.13	3.92	5.10	8.77	8.52
	185	2.4 ± 0.8	3.92	5.10	8.77	8.52
	185	1.1 ± 0.16	3.92	5.10	8.77	8.52
	184	2.3 ± 0.58	3.92	5.09	8.76	8.52
	104	9.6 ± 0.9	3.85	3.90	7.71	7.72
	103	11.4 ± 1.28	3.85	3.89	7.69	7.70
	102	7.5 ± 1.88	3.81	3.84	7.60	7.61
	102	6.4 ± 2.59	3.81	3.84	7.60	7.61
	101	8.4 ± 2.17	3.81	3.83	7.56	7.58
	100	10.3 ± 3.5	3.78	3.79	7.50	7.52
	99	8.8 ± 0.29	3.85	3.89	7.61	7.63
	98	9.3 ± 2.17	4.04	4.16	8.01	8.01
	98	7.4 ± 2.68	4.04	4.16	8.01	8.01
	98	9.9 ± 1.65	4.04	4.16	8.01	8.01
	97	10.2 ± 1.32	4.18	4.38	8.34	8.33
	97	8.4 ± 1.73	4.18	4.38	8.34	8.33
	97	8.7 ± 2.63	4.18	4.38	8.34	8.33
	96	5.2 ± 1.33	4.28	4.50	8.57	8.55

Variable velocity models

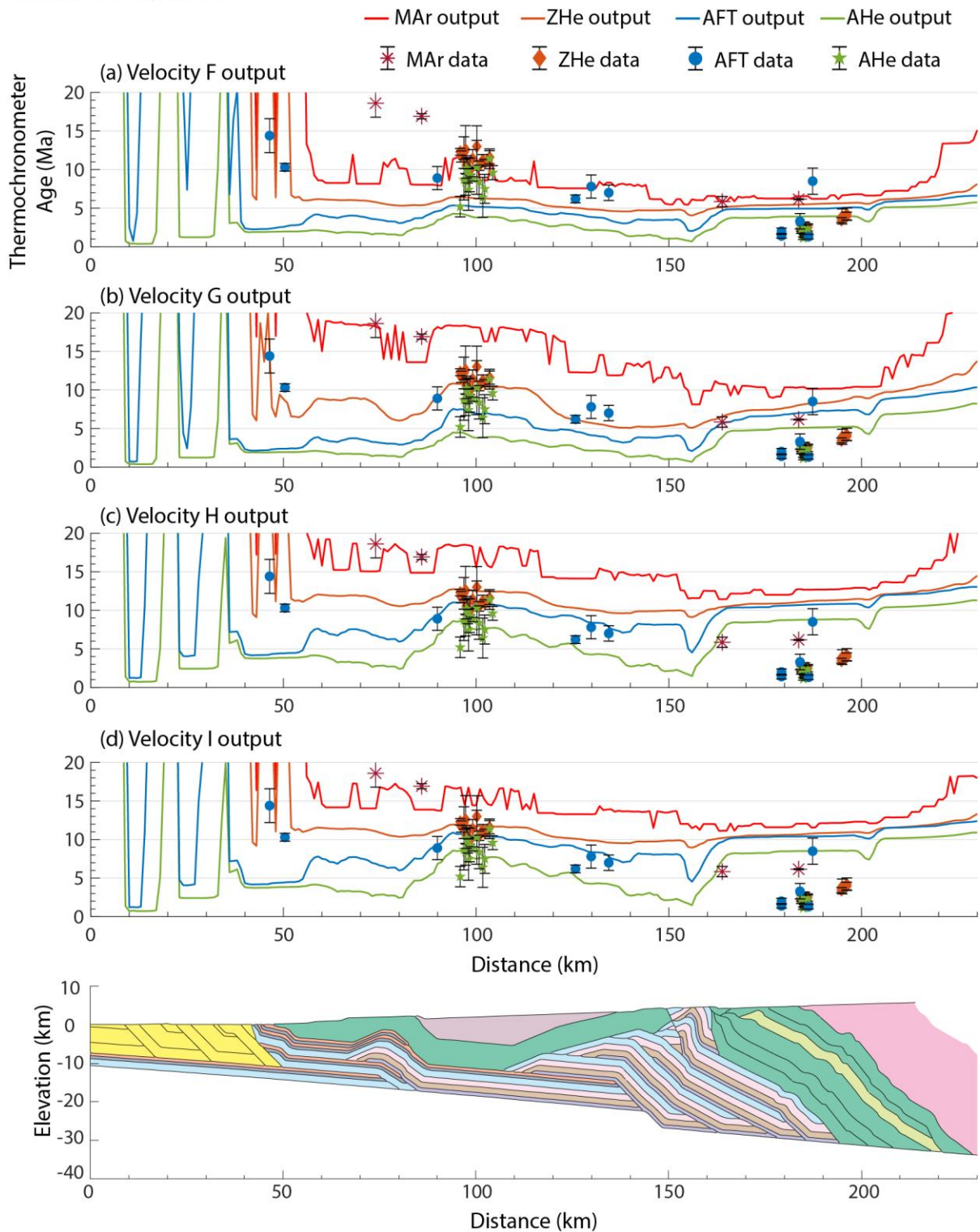


Figure 12: Predicted MAr (red line), ZHe (orange line), AFT (blue line), and AFT (green line) cooling age outputs for Olsen et al. (2018) cross section Pecube models with variable velocity models, summarized in Table 5. (A) Velocity F, (B) Velocity G, (C) Velocity H, and (D) Velocity I all with $A_0 = 2.0 \mu\text{W m}^{-3}$.

Velocity F is comparable to velocity A for the Robinson et al. (2006) models. The MCT moved from 25 to 13 Ma, the RMT moved from 13 to 9 Ma, the LHD formed from 9 to 5 Ma, and the SHTS and OOST faults moved from 5 to 0 Ma (Table 5). Predicted cooling ages match 3 out of 57 existing observed cooling ages (Fig. 12A & Table 9). The predicted MAr ages in the LHD and north of the MCT either match or are very close to matching the observed cooling ages. The predicted MAr ages in the DK are ~10 to 9 Ma younger than the observed ages. Modeled ZHe cooling ages are too young in the DK (~85 – 135 km) with modeled ages ~6.5 Ma and observed ages between ~9 – 13 Ma. ZHe modeled ages are too old north of the MCT in GH rocks with modeled cooling ages of ~5 – 6 Ma compared to the observed ~2 – 4 Ma ages. The predicted AFT ages north of the MCT are ~5 Ma, which is ~1.5 to 3.5 Ma older than the observed ages. Predicted AFT ages south of the MCT are much younger than the observed cooling ages. Predicted AHe ages have a similar pattern to predicted AFT ages, with predicted ages north of the MCT ~3 – 2 Ma older than observed ages and predicted ages in the DK ~2 – 8 Ma younger than observed ages.

Velocity G is based off of constraints for fault movement from Robinson and McQuarrie (2012). In this model, the MCT moves from 25 – 20 Ma, the RMT moves from 20 – 16 Ma, the LHD forms from 16 – 5 Ma, and the SHTS and OOST faults moves from 5 – 0 Ma (Table 5). Predicted cooling ages match 10 out of 57 observed cooling ages (Fig. 12B & Table 9). The model overestimates MAr ages in the LHD and GH just north of the MCT with predicted ages ~10.5 Ma, which is >4 Ma older than the observed ages. The modeled MAr age in the DK is ~3 Ma younger than the observed age. South of the DK between 75 – 85 km, the modeled MAr age falls within 2σ of the observed age. Modeled ZHe cooling ages are too old north of the northern ramp with modeled cooling ages are ~5 – 6 Ma older than the actual observed ages. This velocity

model predicts 6 of the 12 ZHe ages in the DK with modeled ages \sim 10 – 11 Ma and observed ages between \sim 9 – 13 Ma. Velocity G reproduces 1 of the 11 AFT ages. The modeled AFT age that matched is north of the MCT and the observed age is 8.5 ± 1.7 Ma, which is much older than the other observed ages in this area which are \sim 1 – 3 Ma. All other modeled AFT ages north of the MCT are \sim 4 – 5 Ma older than the observed ages. The predicted AFT ages in the LHD are \sim 3 Ma younger than the observed cooling ages and in the DK is \sim 4 Ma younger than the observed ages. Most notably, there are two AFT ages south of the southern ramp with predicted ages of \sim 2 Ma and observed ages \sim 10 and 14 Ma. The AHe predicted ages north of the MCT are \sim 5 Ma with the observed ages between \sim 1 – 2 Ma. Within the DK, the predicted AHe ages are between 3 – 4.5 Ma, and the observed ages range from \sim 5 – 11 Ma.

The shortening rate for the RMT is faster in Velocity H to make the predicted ages older in the DK. To produce old MAr ages in the DK, movement on the MCT and RMT needs to start and end early because the cooling ages in the DK are set during movement on the MCT and RMT. In this model, the MCT moves from 25 – 20 Ma, the RMT and LHD sheets move from 20 – 10 Ma, and the SHTS and OOST faults moves from 10 – 0 Ma (Table 5). Modeled cooling ages match 15 out of 57 published cooling ages (Fig. 12B & Table 9). While the fit for the predicted ZHe, AFT, and AHe ages in the DK improves when compared to Velocity G, the fit for the predicted cooling ages north of the MCT is worse than Velocity G (Fig. 12C & Table 9). For all four thermochronometer systems, the predicted cooling ages north of the MCT are much younger than the observed ages. Predicted ages north of the MCT are older than the observed cooling ages by \sim 6 Ma for MAr, \sim 9 – 7 Ma for ZHe, \sim 8 – 9 Ma for AFT, and $>$ 6 Ma for AHe. Predicted AFT ages for the 2 observed AFT ages south of the southern ramp are younger than the observed ages by \sim 6 and 10 Ma, which is less than the \sim 8 and 12 Ma of Velocityl A. In

summary, Velocity H better predicts the cooling ages in the DK than Velocity G but produces a worse fit for cooling ages north of the MCT.

Velocity I keeps the older cooling ages in the DK while attempting to lower the cooling ages north of the MCT. The MCT moves from 25 – 18 Ma, the RMT and LHD thrust sheets move from 18 – 10 Ma, and the SHTS and OOST faults moves from 10 – 0 Ma. The velocity of the MCT is slowed to 31.50 mm yr⁻¹ and the velocity of the RMT and LHD thrust sheets is increased to 71.39 mm yr⁻¹ (Table 5). Predicted cooling ages matches 19 out of 57 published cooling ages (Fig. 12D & Table 9). This model predicts the ages for ZHe, AFT, and AHe ages in the DK well; however, fails to reproduce ages north of the MCT, although the predicted ages north of the MCT are closer to the observed ages than Velocity H. In the DK, the predicted cooling ages reproduces 8 of 12 ZHe ages, 1 of 2 AFT ages, and 8 of 14 AHe ages. Predicted MAr ages north of the north ramp are too old with predicted ages of ~11 and 12 Ma compared to the observed ages of ~6 Ma. In the DK and south of the southern ramp, the predicted MAr ages are too young with predicted ages of ~14 Ma and observed ages ~17 and 19 Ma. Predicted ages north of the MCT for ZHe are ~6 – 8 Ma, AFT are ~7 – 9 Ma, and AHe >6 Ma older than the observed cooling ages.

While Velocity I makes the predicted ages north of the MCT younger compared to Velocity H, the predicted ages are not young enough to match the observed cooling ages. Although Velocity I for the Olsen et al. (2018) cross section successfully reproduces the most observed cooling ages of all the models for both this cross section and the Robinson et al. (2006) cross section, there is still a large discrepancy between the modeled and observed cooling ages that cannot be resolved by adjusting the radiogenic heat production value or the fault velocity rates. This cross section geometry cannot reproduce the cooling ages along the cross section.

5. INTERPERTATIONS AND DISCUSSION

5.1 Evaluating the sensitivity of predicted cooling ages

The geothermal field determines the spatial and temporal changes in the predicted cooling ages. The horizontal and vertical temperature distribution evolves at each time step in the model, based on thermal parameters, location and magnitude of fault displacement and erosion, and rates of deformation and exhumation. In the thermokinematic modeling process, changing the radiogenic heat production value and the timing of fault movements changes the evolution of the geothermal gradient throughout the model resulting in predicted cooling ages.

The radiogenic heat production value controls the thermal state in the crust, lower A_0 values will produce a cooler crust and higher A_0 values produce a hotter crust. Multiple models with the same exhumation rate but different radiogenic heat production values produce different predicted cooling ages for rocks at the present-day surface (Figs. 8 and 11). In cooler models ($A_0 = 2.0 \mu\text{W m}^{-3}$), the rocks pass through the thermal closure temperatures earlier in the model due to the lower thermal gradient. In the hotter models, rocks pass through the higher thermal gradient of hotter models ($A_0 = 3.0 \mu\text{W m}^{-3}$) later. The result is different predicted cooling ages at the present-day surface depending on the thermal state of the crust, with higher A_0 values producing younger cooling ages and lower A_0 values predicting older cooling ages. Notably, radiogenic heat production values do not affect the shape of the predicted cooling curve; however, it shifts the cooling curves ages younger with increasing A_0 values (Figs. 8 and 11). Therefore, radiogenic heat production does not control the across-strike shape of cooling curves,

rather it affects the thermal gradient in the crust and varying A_0 values shifts cooling curves older or younger (Figs. 8 and 11).

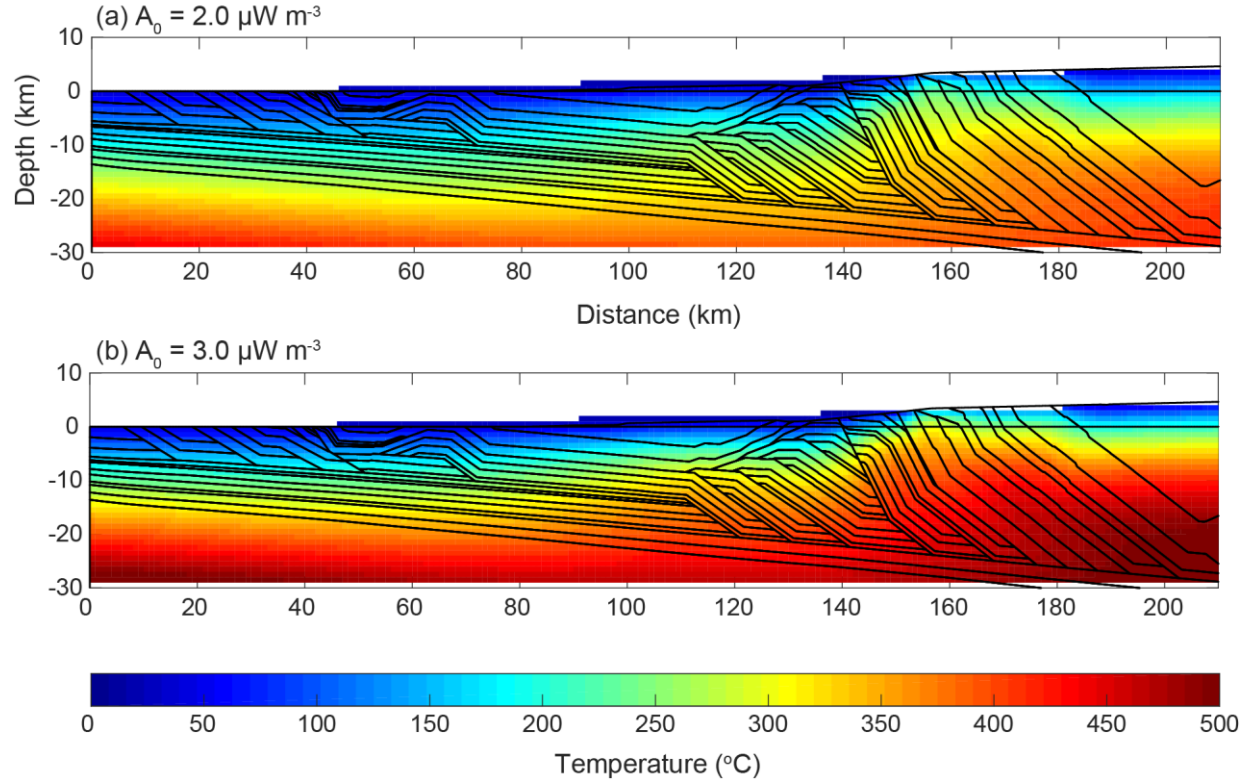


Figure 13: Thermal structure of crust in final step of Robinson et al. (2006) Pecube models for (A) $A_0 = 2.0 \mu\text{W m}^{-3}$ and (B) $A_0 = 3.0 \mu\text{W m}^{-3}$.

Figure 13 compares the thermal structure of the crust at the final step of the Robinson et al. (2006) cross section for an A_0 of $2.0 \mu\text{W m}^{-3}$ and $3.0 \mu\text{W m}^{-3}$. The thermal structure for the model with an A_0 of $3.0 \mu\text{W m}^{-3}$ is a relatively hot model similar to the thermal structure presented in Herman et al. (2010) in central Nepal. This hot model does not predict the older cooling ages found in the DK along the Simikot cross section. The predicted ages are too young because this part of the crust is too hot and rocks move through the isotherm for closure temperatures later in the model. The thermal structure for the model with an A_0 of $2.0 \mu\text{W m}^{-3}$ is a cold model similar

to the thermal structure presented in Bollinger et al. (2006) in central Nepal. A cold crustal model predicts older cooling ages in the DK compared to the hot model. The cold model is used in this study because it produces predicted cooling ages that more closely match the observed cooling ages.

Deformation and exhumation rates at each time step affects the evolution of the thermal field and the resulting predicted cooling ages. Timing of deformation and exhumation is limited by existing data on the initiation of movement on specific faults, timing of deposition of synorogenic units, and tectonic rates. A variety of velocity models are tested to best match the predicted cooling ages to observed cooling ages while staying within the limiting parameters of fault movements from previous studies (Table 5). Timing of fault movement changes the thermal field of the crust as heat is advected upward along thrust faults. The thermokinematic models show that as the velocity of movement on the MCT and RMT is increased, the predicted cooling ages in the DK become older matching more of the observed data. However, the predicted ages north of the MCT are much older than the observed ages for both the Robinson et al. (2006) and Olsen et al. (2018) cross sections. Realistic velocity rates poorly reproduce the cooling ages. More extreme velocity models (i.e., Velocity D) reproduce a few more of the cooling ages in specific locations; however, these still fail to overall produce the cooling pattern across the entire section, indicating an invalid cross section geometry.

5.2 Evaluating cross section geometry

Décollement geometry has a first order control on thermochronometers cooling ages (Lock and Willett, 2008; McQuarrie and Ehlers, 2015, 2017; Gilmore et al., 2018). The Robinson et al. (2006) and Olsen et al. (2018) versions of the Simikot cross section have

different décollement geometries and kinematic sequence of faulting, resulting in different predicted cooling curves across the cross section. The timing and location of exhumation affects the overall shape of the predicted cooling ages.

Changing the décollement fault geometry changes the location of “U-shape” cooling pattern associated with the location of the active ramp, which produces young cooling ages (Lock and Willet; McQuarrie and Ehlers, 2015; 2017). In the Robinson et al. (2006) section, the active ramp in the MHT is located between ~110 and 120 km north of the MFT. The predicted cooling ages above this ramp, particularly ZHe, AFT, and ZHe predicted ages, are younger than the predicted ages just to the north or south of the ramp because of the deep rock moving up and over the ramp results in predicted cooling ages at the present day surface younger than the surrounding rocks. The Olsen et al. (2018) version has two ramps in the décollement, the southern ramp between ~75 and 80 km and the northern ramp between ~145 and 150 km. The southern ramp produces young ages on the southern end of the DK. The northern ramp of the Olsen et al. (2018) model is 35 km further north than the ramp in the Robinson et al. (2006) cross section. All velocity models for the Robinson et al. (2006) cross section have a worse fit in the predicted vs. observed ages in the DK than the Olsen et al. (2018) models (Fig. 9 and 12) because the thermochronometer ages are reset later in the model as rock moves over the active ramp, which is located 35 km further south. By shifting this ramp to the north, rocks that are exposed in the modern day DK move over the ramp and are reset earlier, producing older predicted cooling ages in the DK that match the trend of the observed ages (Tables 7 and 9). However, the Olsen et al. (2018) cross section still has predicted cooling ages that are too old for all thermochronometer systems north of the MCT (Table 9). The predicted AFT and AHe cooling ages north of the MCT in the Robinson et al. (2006) models more closely match the

observed data than the Olsen et al. (2018) models because of the magnitude and location of the OOST that move at the very end of the model diving uplift and exhumation north of 140 km from the MFT. The maximum uplift and exhumation is focused where the OOST faults are located (140 and 155 km from the MFT) while the youngest observed chronometers are 180-190 km from the MFT.

The most notable difference in the sequence of faulting for these cross sections is the sequence of the SHTS and OOST as well as the number of OOST. In the Robinson et al. (2006) models, the three OOST faults occur as the last steps after deformation in the SHTS ends (Table 6 & Fig. 7P-S). In the Olsen et al. (2018) model, the two OOST faults move in the time between deformation on the SHTS 3A and SHTS 3B sheets (Table 8 & Fig. 10Q-T). Both cross sections have an OOST at ~40 km and ~ 150 km and the Robinson et al. (2006) cross section has an additional OOST at ~140 km (Fig. 4). The Robinson et al. (2006) models produce much younger ages at these OOST faults at ~150 and 140 km because they move in the final steps. This pattern is not produced in the Olsen et al. (2018) models because the OOST move earlier in the model, so the ages are reset earlier and become older as the last of the SHTS faults move after the OOST. Young thermochronometer ages exist at the locations of the OOST and the OOST faulting occurring at the end of the model best reproduces the young cooling ages. The sequence of faulting changes the thermal field and the resulting predicted cooling ages along section and can cause changes in the pattern of cooling.

5.3 Proposed New Cross Section

The results from the thermokinematic modeling of the Simikot cross section and the modified version of the cross section provide insight into the viability of the two cross section

geometries and why they do not work. These cross section geometries failed to predict most of the cooling ages, with the best model only predicting 33% of cooling ages. The location of the ramp in the Robinson et al. (2006) cross section is too far south to reproduce the older ages in the DK. The northern ramp in the Olsen et al. (2018) cross section is 35 km further north, and it more accurately reproduces the cooling ages in the DK but the cooling ages are to old north of the MCT. While the location of the Olsen et al. (2018) ramp is a better location than the Robinson et al. (2006) cross section for the modeled ages, it still does not reproduce all the cooling ages. To keep the old predicted cooling ages in the DK and reproduce the younger ages north of the MCT, a better location for that ramp would be between ~180 – 185 km. This would produce cool ages north of the MCT because the rock would be directly above the active ramp, and the predicted cooling ages in the DK would be older because they move over the active ramp early in the model.

The Olsen et al. (2018) cross section incorporates a southern ramp between ~75 – 80 km based on the physiographic transition zones of Harvey et al. (2015). Seismic interpretations in Hoste-Colomer et al. (2018) also indicate a ramp at the same location as Harvey et al. (2015) just south of the DK. Two observed AFT ages south of this ramp along the cross section have ages of 14 and 10 Ma. These ages are much older than any of the predicted cooling ages for Velocity F through I, which predicts these two ages between ~2 to 4 Ma. These predicted AFT ages are young because they are reset late in the model as they pass over the ramp at 75-80 km producing very young predicted AFT ages. In the Robinson et al. (2006) Pecube models, there is no southern ramp and the predicted ages for the two AFT ages are ~9 – 10 Ma, which is closer to the observed 14 and 10 Ma ages. More thermochronology data south of the DK is necessary to

argue for the presence of the southern ramp suggested by Harvey et al. (2015) and Hoste-Colomer et al. (2018).

Along with changes to the MHT fault geometry, the proposed cross section needs an intra-GH fault to account for the movement on the High Himalayan discontinuity. Movement along the MCT starts at 25 Ma in this study, although recent studies suggest that movement along the MCT did not initiate until around 17 Ma (Carosi et al., 2013; Montomoli et al., 2013). If the MCT *sensu stricto* did not move until 17 Ma, an intra-GH thrust must have transported the rocks that compose the DK because the MAr observed ages show cooling between ~19 to 17 Ma. Thus, there must be an earlier fault within the GH that moves before the MCT and places GH rock overtop of LH rock. This would produce the older MAr ages found in the DK and fit the thermochronometer data, which suggests that this intra-GH thrust was active from ~25 – 17 Ma. The DK was likely emplaced along an intra-GH thrust, possibly the Higher Himalayan discontinuity (Larson et al., 2010; Yakamchuk and Godin, 2012; Imayama et al., 2012; Carosi et al., 2013; Montomoli et al., 2013). Then, the MCT became active around 17 Ma (Carosi et al., 2013; Montomoli et al., 2013).

6. CONCLUSIONS

This study presents thermokinematic models that test the viability of two proposed cross section geometries for the Simikot cross section in far-western Nepal. Both cross section geometries fail to accurately reproduce the existing observed cooling ages along the cross section, with the most successful model only matching 33% of the observed cooling ages. Evaluation of the sensitivity of the modeled cooling ages to changes in the timing and magnitude of deformation and exhumation, and décollement geometry illustrates how these models can be improved. I propose a new cross section geometry with the MHT décollement ramp located between ~180 – 185 km and an intra-GH thrust that moves the DK rather than the MCT. This study highlights the importance of pairing cross section reconstructions with thermokinematic models to test the validity of cross section geometry by comparing the modeled thermochronometer ages with the observed cooling ages.

REFERENCES

- Ahmad, T., Harris, N., Bickle, M., Chapman, H., Bunbury, J., and Prince, C., 2000, Isotopic constraints on the structural relationships between the Lesser Himalayan Series and the High Himalayan Crystalline Series, Garwhal Himalaya: Geological Society of America Bulletin, v. 112, p. 467–477, doi: 10.1130/0016-7606(2000)112<0467:ICOTSR>2.3.CO;2.
- Arita, K., Shiraishi, K., and Hayashai, D., 1984, Geology of western Nepal and a comparison with Kumaon, India: Hokkaido, Japan, Faculty of Science Journal, Hokkaido University, Ser. 4, v. 2, p. 1–20.
- Bai, Z., Zhang, S., and Braatenberg, C., 2013, Crustal density structure from 3D gravity modeling beneath Himalaya and Lhasa blocks, Tibet: Journal of Asian Earth Sciences, v. 78, p. 301–317, doi: 10.1016/j.jseaes.2012.12.035.
- Besse, J., and Courtillot, V., 1988, Paleogeographic maps of the continents bordering the Indian Ocean since the Early Jurassic: Journal of Geophysical Research, v. 93, p. 11,791–11,808.
- Bilham, R., Larson, K., and Freymueller, J., 1997, GPS measurements of present-day convergence across the Nepal Himalaya: Naure, p. 61–64.
- Bollinger, L., Henry, P., and Avouac, J.P., 2006, Mountain building in the Nepal Himalaya: Thermal and kinematic model: Earth and Planetary Science Letters, v. 244, p. 58–71, doi: 10.1016/j.epsl.2006.01.045.
- Braden, Z., Godin, L., and Cottle, J.M., 2017, Segmentation and rejuvenation of the Greater Himalayan sequence in western Nepal revealed by in situ U–Th/Pb monazite petrochronology: Lithos, v. 284–285, p. 751–765, doi: 10.1016/j.lithos.2017.04.023.
- Braden, Z., Godin, L., Cottle, J., and Yakymchuk, C., 2018, Renewed late Miocene (< 8 Ma) hinterland ductile thrusting, western Nepal Himalaya: Geology, v. 46, p. 503–506, doi: 10.1130/G40097.1.
- Braun, J., 2003, Pecube: a new finite-element code to solve the 3D heat transport equation including the effects of a time-varying, finite amplitude surface topography, Computer Geoscience, v. 29, p. 787–794, doi:10.1016/S0098-3004(03)00052-9.

Brookfield, M. E., 1993, The Himalayan passive margin from Precambrian to Cretaceous times, *Sediment. Geology*, v. 84, p. 1–35, doi:10.1016/0037-0738(93)90042-4. Carosi, R., Montomoli, C., Rubatto, D., and Visonà, D., 2013, Leucogranite intruding the South Tibetan Detachment in western Nepal: Implications for exhumation models in the Himalayas: *Terra Nova*, v. 25, p. 478–489, doi: 10.1111/ter.12062.

Chen, B., Liu, J., Chen, C., Du, J., and Sun, Y., 2015, Elastic thickness of the Himalayan-Tibetan orogen estimated from the fan wavelet coherence method, and its implications for lithospheric structure: *Earth and Planetary Science Letters*, v. 409, p. 1–14, doi: 10.1016/j.epsl.2014.10.039.

Coutand, I., Whipp, D.M., Grujic, D., Bernet, M., Fellin, M.G., Bookhagen, B., Landry, K.R., Ghalley, S.K., and Duncan, C., 2014, Journal of Geophysical Research: Solid Earth of multithermochronologic data: *Journal of Geophysical Research: Solid Earth*, p. 1–36, doi: 10.1002/2013JB010891.

DeCelles, P.G., Gehrels, G.E., Quade, J., Ojha, T.P., Kapp, P.A., and Upreti, B.N., 1998a, Neogene foreland basin deposits, erosional unroofing, and the kinematic history of the Himalayan fold-thrust belt, western Nepal: *Bulletin of the Geological Society of America Bulletin*, v. 110, p. 2–21, doi:10.1130/0016-7606(1998)110<0002:NFBDEU>2.3.CO;2.

DeCelles, P.G., Gehrels, G.E., Quade, J., and Ojha, T.P., 1998b, Eocene early Miocene foreland basin development and the history of Himalayan thrusting, western and central Nepal: *Tectonics*, v. 17, p. 741–765.

DeCelles, P.G., Gehrels, G.E., Quade, J., LaReau, B., and Spurlin, M., 2000, Tectonic Implications of U-Pb Zircon Ages of the Himalayan Orogenic Belt in Nepal: *Science*, v. 288, p. 497–499, doi: 10.1126/science.288.5465.497.

DeCelles, P.G., Robinson, D.M., Quade, J., Ojha, T.P., Garzione, C.N., Copeland, P., and Upreti, B.N., 2001, Stratigraphy, structure, and tectonic evolution of the Himalayan fold-thrust belt in western Nepal: *Tectonics*, v. 20, p. 487–509, doi: 10.1029/2000TC001226.

DeCelles, P.G., Robinson, D.M., and Zandt, G., 2002, Implications of shortening in the Himalayan fold-thrust belt for uplift of the Tibetan Plateau: *Tectonics*, v. 21, p. 1062–1087, doi: 10.1029/2001TC001322.

DeCelles, P.G., Kapp, P., Ding, L., and Gehrels, G.E., 2007, Late Cretaceous to middle Tertiary basin evolution in the central Tibetan Plateau: Changing environments in response to tectonic partitioning, aridification, and regional elevation gain: *Bulletin of the Geological Society of America*, v. 119, p. 654–680, doi: 10.1130/B26074.1.

Decelles, P., Kapp, P., Gehrels, G., and Ding, L., 2014, Paleocene-Eocene foreland basin evolution in the Himalaya of southern Tibet and Nepal: Implications for the age of initial India-Asia collision: *Tectonics*, v. 33, doi: 10.1002/2014TC003522.

- Ehlers, T., and Farley, K.A., 2003, Apatite (U-Th)/He thermochronology: methods and applications to problems in tectonic and surface processes: *Earth Planet Science Letters*, v. 206, p. 1–14.
- Ehlers, T. A., 2005, Crustal thermal processes and thermochronometer interpretation, in: Low-Temperature Thermochronology: Techniques, Interpretations, and Applications, Review Mineral Geochemistry, v. 58, p. 315–350, doi:10.2138/rmg.2005.58.12.
- Fuchs, G.R., and Frank, W., 1970, The geology of west Nepal between the rivers Kali Gandaki and Thulo Bheri: *Jahrbuch der Geologischen Bundesanstalt*, v. 18, p. 103.
- Gansser, A., 1964, *Geology of the Himalayas*, Wiley-Interscience, New York, p. 289.
- Garzanti, E., 1999, Stratigraphy and sedimentary history of the Nepal Tethys Himalaya passive margin: *Journal of Asian Earth Sciences*, doi: 10.1016/S1367-9120(99)00017-6.
- Guatam, P., and Fujiwara, Y., 2000, Magnetic polarity stratigraphy of Siwalik Groupd seds of Karnali River section in western Nepal: *Geophysical Journal International*, v. 142, p. 812–824.
- Gehrels, G.E., DeCelles, P.G., Martin, A., Ojha, T.P., Pinhassi, G., and Upreti, B.N., 2003, Initiation of the Himalayan orogen as an early Paleozoic thin-skinned thrust belt: *GSA Today*, v. 13, p. 4–9, doi: 10.1130/1052-5173(2003)13<4:IOTHOA>2.0.CO;2.
- Gehrels, G.E., DeCelles, P.G., Ojha, T.P., and Upreti, B.N., 2006, Geologic and U-Pb geochronologic evidence for early Paleozoic tectonism in the Dadeldhura thrust sheet, far-west Nepal Himalaya: *Journal of Asian Earth Sciences*, v. 28, p. 385–408, doi: 10.1016/j.jseaes.2005.09.012.
- Gehrels, G.E., Valencia, V.A., and Ruiz, J., 2008, Enhanced precision, accuracy, efficiency, and spatial resolution of U-Pb ages by laser ablation-multicollector-inductively coupled plasmamass spectrometry: *Geochemistry, Geophysics, Geosystems*, v. 9, doi: 10.1029/2007GC001805.
- Gilmore, M.E., McQuarrie, N., Eizenhöfer, P.R., and Ehlers, T.A., 2018, Testing the effects of topography, geometry, and kinematics on modeled thermochronometer cooling ages in the eastern Bhutan Himalaya: *Solid Earth*, v. 9, p. 599–627, doi: 10.5194/se-9-599-2018.
- Godin, L., Parrish, R.R., Brown, R.L., and Hodges, K. V., 2001, Crustal thickening leading to exhumation of the Himalayan metamorphic core of Central Nepal: Insight from U-Pb geochronology and 40Ar/39Ar thermochronology: *Tectonics*, doi: 10.1029/2000TC001204.
- Godin, L., 2003, Structural evolution of the Tethyan sedimentary sequence in the Annapurna area, central Nepal Himalaya: *Journal of Asian Earth Sciences*, doi: 10.1016/S1367-9120(03)00066-X.

Harvey, J. E., 2015, University of California, Santa Barbara, ProQuest Dissertations Publishing, 2015. 3733555 (Unpublished).

Harvey, J.E., Burbank, D.W., and Bookhagen, B., 2015, Along-strike changes in Himalayan thrust geometry: Topographic and tectonic discontinuities in western Nepal: Lithosphere, v. 7, p. 511–518, doi: 10.1130/L444.1.

He, D., Webb, A.A.G., Larson, K.P., and Schmitt, A.K., 2016, Extrusion vs. duplexing models of Himalayan mountain building 2: The South Tibet detachment at the Dadeldhura klippe: Tectonophysics, v. 667, p. 87–107, doi: 10.1016/j.tecto.2015.11.014.

Herman, F., Copeland, P., Avouac, J.P., Bollinger, L., Maheo, G., Le Fort, P., Rai, S., Foster, D., Pecher, A., Stuwe, K., and Henry, P., 2010, Exhumation, crustal deformation, and thermal structure of the Nepal Himalaya derived from the inversion of thermochronological and thermobarometric data and modeling of the topography: Journal of Geophysical Research: Solid Earth, v. 115, p. 1–38, doi: 10.1029/2008JB006126.

Hetzel, R., Dunkl, I., Haider, V., Strobl, M., von Eynatten, H., Ding, L., and Frei, D., 2011, Peneplain formation in southern Tibet predates the India-Asia collision and plateau uplift: Geology, v. 39, p. 983–986, doi: 10.1130/G32069.1

Hodges, K., 2003, Geochronology and thermochronology in orogenic systems, in: Turekian, K.K., Holland, H.D. eds., Treatise on Geochemistry, Elsevier, p 263-292.

Hoste-Colomer, R., Bollinger, L., Lyon-Caen, H., Adhikari, L.B., Baillard, C., Benoit, A., Bhattacharai, M., Gupta, R.M., Jacques, E., Kandel, T., Koirala, B.P., Letort, J., Maharjan, K., Matrau, R., et al., 2018, Lateral variations of the midcrustal seismicity in western Nepal: Seismotectonic implications: Earth and Planetary Science Letters, v. 504, p. 115–125, doi: 10.1016/j.epsl.2018.09.041.

Hu, X., Garzanti, E., Wang, J., Huang, W., An, W., and Webb, A., 2016, The timing of India-Asia collision onset—Facts, theories, controversies: Earth-Science Reviews, v. 160, p. 264–299, doi:10.1016 /j.earscirev.2016.07.014.

Huerta, A.D., and Rodgers, D.W., 2006, Constraining rates of thrusting and erosion: Insights from kinematic thermal modeling: Geology, v. 34, p. 541–544, doi: 10.1130/G22421.1.

Husson, L., and I. Moretti, 2002. Thermal regime of fold and thrust belts – an application to the Bolivian sub Andean zone: Tectonophysics, v. 345, p. 253-280.

Huyghe, P., Galy, A., Mugnier, J.-L., and France-Lanord, C., 2001, Propagation of the thrust system and erosion in the Lesser Himalaya: Geochemical and sedimentological evidence: Geology, v. 29, p. 1007–1010, doi:10.1130/0091-7613(2001)029<1007:POTTSA>2.0.CO;2.

Hayashi, D., Fujii, Y., Yoneshiro, T., and Kizaki, K., 1984, Observations on the geology of the Karnali region, west Nepal. Journal of Nepal Geological Society. 4. 29-40.

- Imayama, T., Takeshita, T., Yi, K., Cho, D.L., Kitajima, K., Tsutsumi, Y., Kayama, M., Nishido, H., Okumura, T., Yagi, K., Itaya, T., and Sano, Y., 2012, Two-stage partial melting and contrasting cooling history within the Higher Himalayan Crystalline Sequence in the far-eastern Nepal Himalaya: *Lithos*, v. 134–135, p. 1–22, doi: 10.1016/j.lithos.2011.12.004.
- Jain, S. K., Goswami, A., and Saraf , A. K., 2008, Determination of land surface temperature and its lapse rate in the Satluj River basin using NOAA data, *International Journal of Remote Sensing*, v. 29, p. 3091–3103, doi: 10.1080/01431160701468992.
- Jiménez-Munt, I., and Platt, J. P., 2006, Influence of mantle dynamics on the topographic evolution of the Tibetan Plateau: Results from numerical modeling, *Tectonics*, 25, TC6002, doi:10.1029/2006TC001963.
- Karner, G. D., & Watts, A. B., 1983, Gravity anomalies and flexure of the lithosphere at mountain ranges. *Journal of Geophysical Research: Solid Earth*, 88(B12), 10449–10477. doi:10.1029/jb088ib12p10449.
- Klootwijk, C. T., Gee, J. S., Peirce, J. W., Smith, G. M., and McFadden, P. L., 1992, An early India-Asia contact: Paleomagnetic constraints from Ninetyeast Ridge, ODP Leg 121, *Geology*, 20, 395–398, [https://doi.org/10.1130/0091-7613\(1992\)020<0395:AEIACP>2.3.CO;2](https://doi.org/10.1130/0091-7613(1992)020<0395:AEIACP>2.3.CO;2).
- La Roche, R.S., Godin, L., Cottle, J.M., and Kellett, D.A., 2016, Direct shear fabric dating constrains early Oligocene onset of the South Tibetan detachment in the western Nepal Himalaya: *Geology*, v. 44, p. 403–406, doi: 10.1130/G37754.1.
- Larson, K. M., Burgmann, R., Bilham, R., and Freymueller, J., 1999, Kinematics of the India-Eurasia collision zone from GPS measurements, *J. Geophys. Res.-Sol. Ea.*, v. 104, p. 1077–1093, doi:10.1029/1998JB900043.
- Larson, K.P., Godin, L, Price, R.A., 2010. Relationships between displacement and distortion in orogens: linking the Himalayan foreland and hinterland in central Nepal. *Geological Society of America Bulletin* 122, 1116-1134.
- Lave, J., and Avouac, J., 2000, Active folding of fluvial terraces across the Siwaliks Hills, Himalayas of central Nepal: *Journal of Geophysical Research*, v. 105, p. 5735–5770.
- Lillie, R.J., Johnson, G.D., Yousuf, M., Zamin, A.S.H., and Yeats, R.S., 1987, Structural development within the Himalayan foreland fold-and-thrust belt of Pakistan, in Beaumont, C., and Tankard, A.J., eds., *Sedimentary basins and basin forming mechanisms: Memoirs of the Canadian Society of Petroleum Geology*, v. 12, p. 379–392.
- Lock, J., and Willett, S., 2008, Low-temperature thermochronometric ages in fold-and-thrust belts: *Tectonophysics*, v. 456, p. 147–162, doi: 10.1016/j.tecto.2008.03.007.

- Lyon-Caen, H., and Molnar, P., 1985, Gravity anomalies, flexure of the Indian plate, and the structure, support, and evolution of the Himalaya and Ganga basin: *Tectonics*, v. 4, p. 513– 538.
- Mandal, S., Robinson, D.M., Khanal, S., and Das, O., 2015, Redefining the tectonostratigraphic and structural architecture of the Almora klippe and the Ramgarh–Munsiari thrust sheet in NW India: Geological Society, London, Special Publications, v. 412, p. 247–269, doi: 10.1515/JOC.1982.3.3.86.
- Martin, A.J., DeCelles, P.G., Gehrels, G.E., Patchett, P.J., and Isachsen, C., 2005, Isotopic and structural constraints on the location of the Main Central thrust in the Annapurna Range, central Nepal Himalaya: *GSA Bulletin*, v. 117, p. 926–944.
- Martin, A. J., 2017, A review of Himalayan stratigraphy, magmatism, and structure: *Gondwana Research*, v. 49, p. 42–80. doi:10.1016/j.gr.2017.04.031
- McCallister, A.T., Taylor, M.H., Murphy, M.A., Styron, R.H., and Stockli, D.F., 2014, Thermochronologic constraints on the late Cenozoic exhumation history of the Gurla Mandhata metamorphic core complex, Southwestern Tibet: *Tectonics*, v. 33, p. 27–52, doi: 10.1002/2013TC003302.
- McQuarrie, N., and Ehlers, T.A., 2015, Influence of thrust belt geometry and shortening rate on thermochronometer cooling ages: Insights from thermokinematic and erosion modeling of the Bhutan Himalaya: *Tectonics*, v. 34, p. 1055–1079, doi: 10.1002/2014TC003783.
- McQuarrie, N. and Ehlers, T. A., 2017, Techniques for understanding fold-thrust belt kinematics and thermal evolution, in: *Linkages and Feedbacks in Orogenic Systems*, GSA Memoirs, edited by: Law, R. D., Thigpen, J. R., Merschat, A. J., and Stowell, H. H., 213, 25–54, [https://doi.org/10.1130/2017.1213\(02\)](https://doi.org/10.1130/2017.1213(02)).
- Mercier, J., 2014, Structure et dynamique des prismes orogéniques : une approche pluridisciplinaire sur le cas Himalaya. Unpublished PhD Thesis, Université de Grenoble, 329 pp.
- Montomoli, C., Iaccarino, S., Carosi, R., Langone, A., and Visonà, D., 2013, Tectonometamorphic discontinuities within the Greater Himalayan Sequence in Western Nepal (Central Himalaya): Insights on the exhumation of crystalline rocks: *Tectonophysics*, v. 608, p. 1349–1370, doi: 10.1016/j.tecto.2013.06.006.
- Mugnier, J.-L., Leturmy, P., Mascle, G., Huyghe, P., Chalaron, E., Vidal, G., Husson, L., and Delcaillau, B., 1999, The Siwaliks of western Nepal I. Geometry and kinematics: *Journal of Asian Earth Sciences*, v. 17, p. 629–642, doi: 10.1016/S1367-9120(99)00038-3.
- Murphy, M.A., and Yin, A., 2003, Structural evolution and sequence of thrusting in the Tethyan fold-thrust belt and Indus-Yalu suture zone, southwest Tibet: *GSA Bulletin*, v. 115, p. 21–34, doi: 10.1130/0016-7606(2003)115<0021:SEASOT>2.0.CO;2.

- Murphy, M.A., Yin, A., Kapp, P., Harrison, T.M., Manning, C.E., Ryerson, F.J., Ding, L., and Guo, J., 2002, Structural evolution of the Gurla Mandhata detachment system, southwest Tibet: Implications for the eastward extent of the Karakoram fault system: Geological Society of America Bulletin, v. 114, p. 428–447, doi: 10.1130/0016-7606(2002)114<0428: SEOTGM>2.0.CO;2.
- Murphy, M.A., and Copeland, P., 2005, Transtensional deformation in the central Himalaya and its role in accommodating growth of the Himalayan orogen: Tectonics, v. 24, TC4012, doi:10.1029/2004TC001659.
- Najman, Y., Carter, A., Oliver, G., and Garzanti, E., 2005, Provenance of Eocene foreland basin sediments, Nepal: Constraints to the timing and diachroneity of early Himalayan orogenesis: Geology, v. 33, p. 309–312, doi: 10.1130/G21161.1.
- Najman, Y., Jenks, D., Godin, L., Boudagher-Fadel, M., Millar, I., Garzanti, E., Horstwood, M., and Bracciali, L., 2017, The Tethyan Himalayan detrital record shows that India-Asia terminal collision occurred by 54 Ma in the Western Himalaya: Earth and Planetary Science Letters, v. 459, p. 301–310, doi:10.1016 /j.epsl.2016.11.036.
- Nakayama, K., and Ulak, P., 1999, Evolution of fluvial style in the Siwalik Group in the foothills of the Nepal Himalaya: Sedimentary Geology, v. 125, p. 205–224, doi:10.1016/S0037-0738(99)00012-3.
- Ojha, T.P., Butler, R.F., Quade, J., DeCelles, P.G., Richards, D., and Upreti, B.N., 2000, Magnetic polarity stratigraphy of the Neogene Siwalik Group at Kutia Khola, far western Nepal: GSA Bulletin, v. 112, p. 424–434.
- Ojha, T.P., Butler, R.F., DeCelles, P.G., and Quade, J., 2009, Magnetic polarity stratigraphy of the Neogene foreland basin deposits of Nepal: Basin Research, doi: 10.1111/j.1365-2117.2008.00374.x.
- Olsen, J. E. S., 2018, Determining relative age of out-of-sequence faults: integration of foreland basin deposits to a flexural thrust belt evolution and a case study in Western Nepal. Master's Thesis, University of Pittsburgh. (Unpublished).
- Patriat, P., and Achache, J., 1984, Indian-Asia collision chronology has implications for crustal shortening and driving mechanisms of plates: Nature, v. 311, p. 615–621, doi: 10.1038/311615a0.
- Powers, P.M., Lillie, R.J., and Yeates, R.S., 1998, Structure and shortening of the Kangra and Dehra Dun reentrants, Sub-Himalaya, India: Geological Society of America Bulletin, v. 110, p. 1010–1027, doi: 10.1130/0016-7606(1998)110<1010:SASOTK>2.3.CO;2.
- Quade, J., Cater, J.M.L., Ojha, T.P., Adam, J., and Harrison, T.M., 1995, Late Miocene environmental change in Nepal and the northern Indian subcontinent: Stable isotopic evidence from paleosols: Geological Society of America Bulletin, v. 107, p. 1381–1397, doi:10.1130/0016-7606(1995)107<1381:LMECIN>2.3.CO;2.

- Rahn, M.K., and Grasemann, B., 1999, Fission track and numerical thermal modeling of differential exhumation of the Glarus thrust plane (Switzerland): *Earth and Planetary Science Letters*, v. 169, p. 245–259, doi: 10.1016/S0012-821X(99)00078-3.
- Ratschbacher, L., Frisch, W., Liu, G., and Chen, C., 1994, Distributed deformation in southern and western Tibet during and after the India-Asia collision: *Journal of Geophysical Research: Solid Earth*, v. 99, p. 19917–19945, doi: 10.1029/94JB00932.
- Robert, X., Van Der Beek, P., Braun, J., Perry, C., and Mugnier, J.L., 2011, Control of detachment geometry on lateral variations in exhumation rates in the Himalaya: Insights from low-temperature thermochronology and numerical modeling: *Journal of Geophysical Research: Solid Earth*, v. 116, p. 1–22, doi: 10.1029/2010JB007893.
- Robinson, D.M., 2008, Forward modeling the kinematic sequence of the central Himalayan thrust belt, western Nepal: p. 785–801, doi: 10.1130/GES00163.1.
- Robinson, D.M., DeCelles, P., and Copeland, P., 2006, Tectonic evolution of the Himalayan thrust belt in western Nepal: Implications for channel flow models: *GSA Bulletin*, v. 118, p. 865–885.
- Robinson, D.M., DeCelles, P.G., Garzione, C.N., Pearson, O.N., Harrison, T.M., and Catlos, E.J., 2003, Kinematic model for the Main Central thrust in Nepal: *Geology*, v. 31, p. 359–362, doi:10.1130/0091-7613(2003)031<0359:KMFTMC>2.0.CO;2.
- Robinson, D.M., DeCelles, P.G., Patchett, P.J., and Garzione, C.N., 2001, The kinematic evolution of the Nepalese Himalaya interpreted from Nd isotopes: *Earth and Planetary Science Letters*, doi: 10.1016/S0012-821X(01)00451-4.
- Robinson, D.M., and McQuarrie, N., 2012, Robinson and McQuarrie, Pulsed deformation and variable slip rates within the CN thrust belt: *Lithosphere*, v. 4, p. 449–464.
- Robinson, D.M., and Pearson, O.N., 2013, Was Himalayan normal faulting triggered by initiation of the Ramgarh-Munsiari thrust and development of the Lesser Himalayan duplex? *International Journal of Earth Sciences*, doi: 10.1007/s00531-013-0895-3.
- Rohrmann, A., Kapp, P., Carrapa, B., Reiners, P.W., Guynn, J., Ding, L., and Heizler, M., 2012, Thermochronologic evidence for plateau formation in central Tibet: By 45 Ma: *Geology*, v. 40, p. 187–190, doi: 10.1130/G32530.1.
- Sakai, H., Iwano, H., Danhara, T., Hirata, T., and Takigami, Y., 2013, Emplacement of hot lesser himalayan nappes from 15 to 10 Ma in the Jumla-Surkhet region, western Nepal, and their thermal imprint on the underlying Early Miocene fluvial Dumri Formation: *Island Arc*, v. 22, p. 361–381, doi: 10.1111/iar.12030.
- Sakai, H., 1983, Geology of the Tansen Group of the Lesser Himalaya in Nepal: *Memoirs of the Faculty of Science: Kyushu University [D]*, v. 25, p. 27–74.

Searle, M.P., Law, R.D., Godin, L., Larson, K.P., Streule, M.M., Cottle, J.M., and Jessup, M.J., 2008, Defining the Himalayan Main Central thrust in Nepal: *Journal of the Geological Society of London*, v. 165, p. 523–534, doi:10.1144/0016-76492007-081.

Shi, Y., and Wang, C.Y., 1987, Two-dimensional modeling of the P-T-t paths of regional metamorphism in simple overthrust terrains: *Geology*, v. 15, p. 1048–1051, doi: 10.1130/0091-7613(1987)15<1048:TMOTPP>2.0.CO;2.

Srivastava, P., and Mitra, G., 1994, Thrust geometries and deep structure of the outer and lesser Himalaya, Kumaon and Garhwal (India): Implications for evolution of the Himalayan fold and thrust belt: *Tectonics*, v. 13, p. 89–109, doi: 10.1029/93TC01130.

Stüwe, K., White, L., and Brown, R., 1994, The influence of eroding topography on steady-state isotherms. Application to fission track analysis: *Earth and Planetary Science Letters*, v. 124, p. 63–74, doi: 10.1016/0012-821X(94)00068-9.

Szulc, A.G., Najman, Y., Sinclair, H.D., Pringle, M.S., Bickle, M., Chapman, H., Garzanti, E., Andó, S., Huyghe, P., Mugnier, J.-L., Ojha, T.P., and DeCelles, P.G., 2006, Tectonic evolution of the Himalaya constrained by detrital 40Ar-39Ar, Sm-Nd and petrographic data from the Siwalik foreland basin succession, SW Nepal: *Basin Research*, v. 18, p. 375–391, doi: 10.1111/j.1365-2117.2006.00307.x.

Turcotte, D.L., and Schubert, G., 1982, *Geodynamics: Applications of continuum physics to geological problems*: Wiley, 450 p.

Upreti, B.N., 1996, Stratigraphy of the western Nepal Lesser Himalaya: A synthesis: *Journal of Nepal Geological Society*, v. 13, p. 11–28.

van der Beek, P., Litty, C., Baudin, M., Mercier, J., Robert, X., and Hardwick, E., 2016, Contrasting tectonically driven exhumation and incision patterns, western versus central Nepal Himalaya: *Geology*, v. 44, p. 327–330, doi:10.1130/G37579.1.

van Hinsbergen, D.J.J., Kapp, P., Dupont-Nivet, G., Lippert, P.C., DeCelles, P.G., and Torsvik, T.H., 2011, Restoration of Cenozoic deformation in Asia and the size of Greater India: *Tectonics*, v. 30, p. 1–31, doi: 10.1029/2011TC002908.

Wang, J., Hu, X., Jansa, L.F., and Huang, Z., 2011, Provenance of the Upper Cretaceous–Eocene deep-water sandstones in Sangdanlin, southern Tibet: Constraints on the timing of initial India-Asia collision: *The Journal of Geology*, v. 119, p. 293–309, doi:10.1086/659145.

Webb, A.A.G., Schmitt, A.K., He, D., and Weigand, E.L., 2011, Structural and geochronological evidence for the leading edge of the Greater Himalayan Crystalline complex in the central Nepal Himalaya: *Earth and Planetary Science Letters*, v. 304, p. 483–495, doi: 10.1016/j.epsl.2011.02.024.

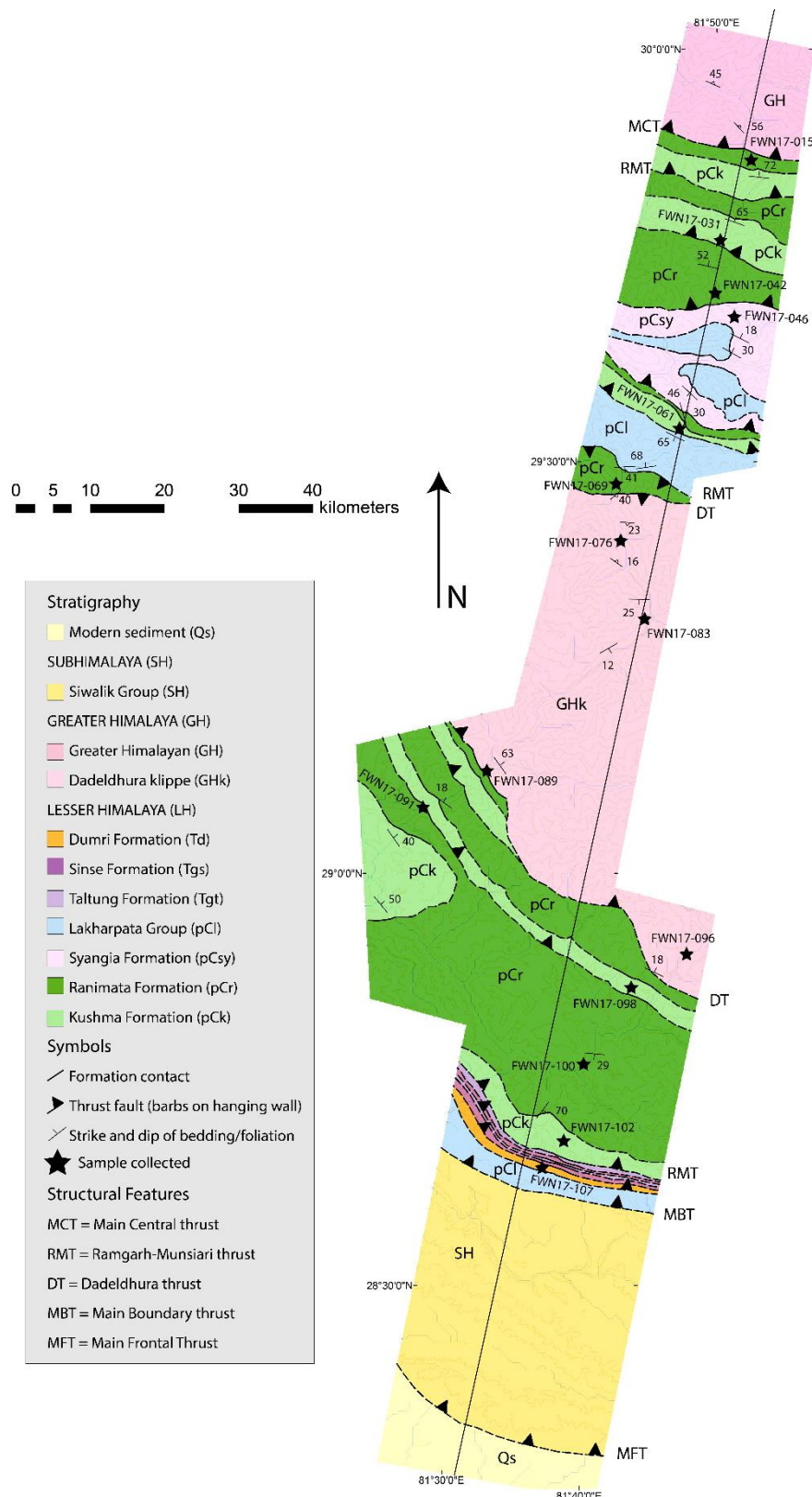
Whipp, D.M., Ehlers, T.A., Blythe, A.E., Huntington, K.W., Hodges, K. V., and Burbank, D.W., 2007, Plio-Quaternary exhumation history of the central Nepalese Himalaya: 2.

Thermokinematic and thermochronometer age prediction model: Tectonics, v. 26, p. 1–23, doi: 10.1029/2006TC001991.

Whipp, D.M., Ehlers, T.A., Braun, J., and Spath, C.D., 2009, Effects of exhumation kinematics and topographic evolution on detrital thermochronometer data: Journal of Geophysical Research: Earth Surface, doi: 10.1029/2008JF001195.

Yakymchuk, C., and Godin, L., 2012, Coupled role of deformation and metamorphism in the construction of inverted metamorphic sequences: An example from far-northwest Nepal: Journal of Metamorphic Geology, v. 30, p. 513–535, doi: 10.1111/j.1525-1314.2012.00979.x.

APPENDIX A: NEW MAPPING OF FAR-WESTERN NEPAL



APPENDIX B: NEW THERMOCHRONOLOGY SAMPLES COLLECTED ALONG
SIMIKOT CROSS SECTION

Sample ID	Latitude (°N)	Longitude (°E)	Rock unit
ZHe Samples			
FWN17-015	29.86481	81.87433	LH Ranimata
FWN17-031	29.76806	81.83283	LH Kushma
FWN17-042	29.70733	81.83181	LH Ranimata
FWN17-046	29.67467	81.85525	LH Syangia
FWN17-061	29.54381	81.78969	LH Kushma
FWN17-069	29.47178	81.71067	LH Ranimata
FWN17-076	29.40461	81.71561	Klippe
FWN17-083	29.31128	81.74856	Klippe
FWN17-089	29.12022	81.55456	Klippe
FWN17-091	29.08028	81.47753	LH Ranimata
FWN17-098	28.85772	81.72558	LH Kushma
FWN17-100	28.76467	81.66450	LH Kushma
FWN17-102	28.68400	81.63558	LH Kushma
FWN17-107	28.64656	81.62178	LH Dumuri
AFT Samples			
FWN17-042	29.70733	81.83181	LH Ranimata
FWN17-069	29.47178	81.71067	LH Ranimata
FWN17-083	29.31128	81.74856	GH Klippe
FWN17-089	29.12022	81.55456	GH Klippe
FWN17-096	28.90111	81.79336	GH Klippe
FWN17-100	28.76467	81.66450	LH Kushma

APPENDIX C: VELOCITY MODELS WITH TIMING OF MOVEMENT ON INDIVIDUAL FAULTS

Robinson et al. (2006) model																			
Fault	Displ- acement (km)	Constant velocity			Velocity A			Velocity B			Velocity C			Velocity D			Velocity E		
		Start (Ma)	End (Ma)	Veloci- ty (mm yr ⁻¹)	Start (Ma)	End (Ma)	Veloci- ty (mm yr ⁻¹)	Start (Ma)	End (Ma)	Veloci- ty (mm yr ⁻¹)	Start (Ma)	End (Ma)	Veloci- ty (mm yr ⁻¹)	Start (Ma)	End (Ma)	Veloci- ty (mm yr ⁻¹)	Start (Ma)	End (Ma)	Veloci- ty (mm yr ⁻¹)
MCT	252	25.00	17.40	33.15	25.00	13.00	21.00	25.00	20.00	50.40	25.00	20.00	50.40	25.00	22.00	84.00	28.00	24.00	63.00
RMT	185.9	17.40	11.79	33.15	13.00	9.00	46.48	20.00	16.00	46.48	20.00	16.10	47.63	22.00	17.32	39.69	24.00	19.71	43.30
LHD 1	66.9	11.79	9.77	33.15	9.00	8.08	72.59	16.00	14.06	34.52	16.10	14.69	47.63	17.32	15.63	39.69	19.71	18.16	43.30
LHD 2	36.65	9.77	8.67	33.15	8.08	7.57	72.59	14.06	13.00	34.52	14.69	13.92	47.63	15.63	14.71	39.69	18.16	17.31	43.30
LHD 3	36.35	8.67	7.57	33.15	7.57	7.07	72.59	13.00	12.00	36.35	13.92	13.16	47.63	14.71	13.79	39.69	17.31	16.47	43.30
LHD 4	36.35	7.57	6.47	33.15	7.07	6.57	72.59	12.00	11.00	36.35	13.16	12.40	47.63	13.79	12.87	39.69	16.47	15.64	43.30
LHD 5	48.5	6.47	5.01	33.15	6.57	5.90	72.59	11.00	10.00	48.50	12.40	11.38	47.63	12.87	11.65	39.69	15.64	14.52	43.30
LHD 6	31.7	5.01	4.06	33.15	5.90	5.47	72.59	10.00	7.96	15.55	11.38	10.71	47.63	11.65	10.85	39.69	14.52	13.78	43.30
LHD 7	19.7	4.06	3.46	33.15	5.47	5.20	72.59	7.96	6.69	15.55	10.71	10.30	47.63	10.85	10.36	39.69	13.78	13.33	43.30
LHD 8	14.2	3.46	3.03	33.15	5.20	5.00	72.59	6.69	5.78	15.55	10.30	10.00	47.63	10.36	10.00	39.69	13.33	13.00	43.30
MBT	12.14	3.03	2.67	33.15	5.00	4.40	72.59	5.78	5.00	15.55	10.00	8.79	10.05	10.00	8.79	10.05	13.00	11.43	7.73
SHTS 1	21.7	2.67	2.01	33.15	4.40	3.32	20.11	5.00	3.77	17.68	8.79	6.63	10.05	8.79	6.63	10.05	11.43	8.62	7.73
SHTS 2	15.8	2.01	1.54	33.15	3.32	2.53	20.11	3.77	2.88	17.68	6.63	5.06	10.05	6.63	5.06	10.05	8.62	6.58	7.73
SHTS 3	17.6	1.54	1.00	33.15	2.53	1.66	20.11	2.88	1.89	17.68	5.06	3.31	10.05	5.06	3.31	10.05	6.58	4.31	7.73
MFT	13.9	1.00	0.59	33.15	1.66	0.96	20.11	1.89	1.10	17.68	3.31	1.93	10.05	3.31	1.93	10.05	4.31	2.51	7.73
OOST 1	2.9	0.59	0.50	33.15	0.96	0.82	20.11	1.10	0.93	17.68	1.93	1.64	10.05	1.93	1.64	10.05	2.51	2.13	7.73
OOST 2	11	0.50	0.17	33.15	0.82	0.27	20.11	0.93	0.31	17.68	1.64	0.55	10.05	1.64	0.55	10.05	2.13	0.71	7.73
OOST 3	5.5	0.17	0.00	33.15	0.27	0.00	20.11	0.31	0.00	17.68	0.55	0.00	10.05	0.55	0.00	10.05	0.71	0.00	7.73

Olsen et al. (2018) model

Fault	Displ- acement (km)	Constant velocity			Velocity F			Velocity G			Velocity H			Velocity I		
		Start age (Ma)	End age (Ma)	Veloci- ty (mm yr^{-1})												
MCT	220.5	25.00	18.70	35.00	25.00	13.00	18.36	25.00	20.00	44.10	25.00	20.00	44.10	25.00	18.00	31.50
RMT	205.65	18.70	12.82	35.00	13.00	9.00	51.41	20.00	16.00	51.41	20.00	16.40	57.11	18.00	15.12	71.39
LHD 1	56.95	12.82	11.20	35.00	9.00	8.38	91.36	16.00	14.43	36.18	16.40	15.40	57.11	15.12	14.32	71.39
LHD 2	51.6	11.20	9.72	35.00	8.38	7.81	91.36	14.43	13.00	36.18	15.40	14.50	57.11	14.32	13.60	71.39
LHD 3	48.48	9.72	8.34	35.00	7.81	7.28	91.36	13.00	11.32	28.86	14.50	13.65	57.11	13.60	12.92	71.39
LHD 4	9.24	8.34	8.07	35.00	7.28	7.18	91.36	11.32	11.00	28.86	13.65	13.49	57.11	12.92	12.79	71.39
LHD 5	52.2	8.07	6.58	35.00	7.18	6.61	91.36	11.00	10.00	52.20	13.49	12.57	57.11	12.79	12.06	71.39
LHD 6	39.82	6.58	5.44	35.00	6.61	6.17	91.36	10.00	8.65	29.39	12.57	11.88	57.11	12.06	11.50	71.39
LHD 7A	10	5.44	5.16	35.00	6.17	6.06	91.36	8.65	8.31	29.39	11.88	11.70	57.11	11.50	11.36	71.39
LHD 7B	27.7	5.16	4.36	35.00	6.06	5.76	91.36	8.31	7.36	29.39	11.70	11.22	57.11	11.36	10.97	71.39
LHD 8	37.65	4.36	2.29	35.00	5.76	5.35	91.36	7.36	6.08	29.39	11.22	10.56	57.11	10.97	10.45	71.39
LHD 9	31.8	2.29	2.38	35.00	5.35	5.00	91.36	6.08	5.00	29.39	10.56	10.00	57.11	10.45	10.00	71.39
MBT	13.95	2.38	1.98	35.00	5.00	4.16	16.66	5.00	4.16	16.66	10.00	8.33	8.33	10.00	8.33	8.33
SHTS 1	5	1.98	1.84	35.00	4.16	3.86	16.66	4.16	3.86	16.66	8.33	7.73	8.33	8.33	7.73	8.33
SHTS 2	19.55	1.84	1.28	35.00	3.86	2.69	16.66	3.86	2.69	16.66	7.73	5.38	8.33	7.73	5.38	8.33
SHTS 3A	8	1.28	1.05	35.00	2.69	2.21	16.66	2.69	2.21	16.66	5.38	4.42	8.33	5.38	4.42	8.33
OOST 1	12.1	1.05			2.21			2.21			4.42			4.42		
OOST 2	2.8		0.63	35.00		1.31	16.66		1.31	16.66		2.63	8.33		2.63	8.33
SHTS 3E	7.7	0.63	0.41	35.00	1.31	0.85	16.66	1.31	0.85	16.66	2.63	1.70	8.33	2.63	1.70	8.33
MFT	14.2	0.41	0.00	35.00	0.85	0.00	16.66	0.85	0.00	16.66	1.70	0.00	8.33	1.70	0.00	8.33